Electron Beam Damage of Biological Specimens in Liquid-Phase Electron Microscopy

Dissertation

zur Erlangung des Grades

Doktorin der Naturwissenschaften

der Naturwissenschaftlich-Technischen Fakultäten der Universität des Saarlandes

vorgelegt von

Patricia Simone Blach

Saarbrücken

2022

Tag des Kolloquiums: 14. November 2022

Dekan:	Prof. Dr. Ludger Santen
Berichterstatter:	Prof. Dr. Dr. h.c. Niels de Jonge Prof. Dr. Karin Jacobs
Akad. Mitglied:	Dr. Thomas John
Vorsitz:	Prof. Dr.-Ing. Michael Vielhaber

Abstract

Electron microscopy of native biological materials is usually hampered by sample preparation procedures such as dehydration and freezing, and by electron beam damage. Liquid phase electron microscopy (LP-EM) allows the observation of biological samples in liquid environments without conventional preparation procedures. However, electron beam damage also occurs in LP-EM, and thresholds for biological samples are not yet fully explored.

In this work, the electron dose tolerance of green fluorescent protein (GFP) was analyzed in LP-EM. Protein damage was studied with increasing electron dose, using fluorescence degradation as an indication. $D_c < 0.01\,\mathrm{e}^-/\mathrm{Å}^2$ and $D_c < 0.1\,\mathrm{e}^-/\mathrm{Å}^2$ were observed for GFP on silicon nitrite in transmission electron microscopy (TEM) and environmental scanning electron microscopy (ESEM), respectively. In TEM, the dose tolerance was increased by three orders of magnitude when GFP was encapsulated in graphene liquid cells. The dose tolerance of more complex systems was investigated by binding GFP to actin filaments in fixed SKBR3 cells, which showed $D_c < 0.1\,\mathrm{e}^-/\mathrm{Å}^2$ in TEM and ESEM. In fixed SKBR3 cells, radiation damage was also studied based on the displacement of labeled membrane proteins. At electron doses of $D = (7.8 \pm 0.4) \cdot 10^3\,\mathrm{e}^-/\mathrm{Å}^2$ these labels showed a displacement of $0.8\,\%$.

Procedures for studying biological materials such as proteins an fixed cells in LP-EM are presented in this thesis. Strategies to study and mitigate beam damage are demonstrated.

Kurzzusammenfassung

Elektronenmikroskopie nativer biologischer Materialien wird in der Regel durch Probenpräparationsverfahren wie Dehydrierung und Einfrieren sowie durch Strahlenschäden behindert. Flüssigphasen-Elektronenmikroskopie (LP-EM) ermöglicht die Beobachtung biologischer Proben in flüssiger Umgebung ohne herkömmliche Präparationsverfahren. Strahlenschäden treten allerdings auch in LP-EM auf, jedoch sind die Grenzwerte biologischer Proben noch nicht vollständig erforscht.
In dieser Arbeit wurde die Dosistoleranz des grün fluoreszierenden Proteins (GFP) in LP-EM analysiert. Proteinschädigung wurde anhand abnehmender Fluoreszenz mit zunehmender Elektronendosis untersucht. $D_c < 0.01\,\mathrm{e}^-/\mathrm{Å}^2$ und $D_c < 0.1\,\mathrm{e}^-/\mathrm{Å}^2$ wurden für GFP auf Siliziumnitrit in Transmissionselektronenmikroskopie (TEM) bzw *environmental scanning electron microscopy* (ESEM) gezeigt. In TEM konnte die Dosistoleranz mit dem Einschluss von GFP in Graphenflüssigzellen um drei Größenordnungen erhöht werden. Zur Untersuchung komplexerer Systemen wurde GFP an Aktinfilamente in SKBR3 Zellen gebunden, die $D_c < 0.1\,\mathrm{e}^-/\mathrm{Å}^2$ in TEM und ESEM zeigten. In fixierten SKBR3-Zellen wurden Strahlenschäden auch anhand der Verschiebung markierter Membranproteine untersucht. Bei $D = (7.8 \pm 0.4) \cdot 10^3\,\mathrm{e}^-/\mathrm{Å}^2$ zeigten diese eine Verschiebung von 0.8 %.
In dieser Arbeit werden Verfahren zur Untersuchung biologischer Materialien wie Proteinen und fixierten Zellen in LP-EM vorgestellt. Strategien zur Untersuchung und Abschwächung von Strahlenschäden werden aufgezeigt.

Acknowledgements

First of all, I would very much like to thank my supervisor Prof. Niels de Jonge for giving me the opportunity to work on this very interesting topic, for his good feedback and advice, and for his confidence and support in all challenges.
A big thank you also goes to all my colleagues at INM and especially the IEM group for being the best colleagues I could have wished for. Thank you for very enjoyable past years both at work and outside, and your support, without which it would not have been possible to finish this thesis. I especially want to mention Dr. Florian Weinberg for always being there for me, for proof reading and for his biological knowledge. Dr. Navina Dahmke for many helpful discussions and all the smart suggestions, her biological knowledge, her interest in my well-being and lots of empathy. Dr. Arixin Bo for proof reading, lots of helpful discussions, his great interest and empathy and for spending a whole INM contract with me at the climbing gym. I also want to mention Dr. Eduardo Ortega, Dr. Sercan Keskin and Dr. Peter Kunnas for their advice and knowledge in electron microscopy, for graphene preparation and for introducing me to the fascinating world of an ARM200. Caroline Lang and Tabea Trampert for their great assistance in the lab and Dr. Zahra Mostajeran for proof reading and her biological support. Many thanks also to our HiWis John and Susann for the cell analysis. A big thank you goes to Jörg Schmauch and Marcus Koch for their support with the ARM200 and the ESEM at any time. I also want to thank the present and former INM colleagues who made it enjoyable for me to come to work every day, here especially to mention Jana, Henrik, Verena, Amir and Hanna. Thank you all for the amazing time we spent, for so many fun activities and for being wonderful people!
Nicht zuletzt möchte ich allen danken, die in jeglicher Hinsicht zur Entstehung dieser Arbeit beigetragen haben und die stets ein offenes Ohr für meine Bedenken und inneren Auseinandersetzungen hatten. Hier gilt mein Dank insbesondere meiner Mama, meinem Papa, meinem Bruder und René, für viele Diskussionen, viel Geduld, aufbauende Worte, bedingungslose Unterstützung und für die Möglichkeit, diese Dissertation umzusetzen.
A big thank you also goes to my friends for listening, for discussions, for always being supportive and understanding and for being such amazing people.

List of Abbreviations

Å Ångström

ADF annular dark field

BB borate buffer

BS^3 bis(sulfosuccinimidyl)suberate

BSA Bovine serum albumin

BSE backscattered electrons

CB cacodylate buffer

CNT carbon nanotube

cryo-EM cryogenic electron microscopy

DIC differential interference contrast

DMEM Dulbecco's modified eagle medium

DNA deoxyribonucleic acid

DPBS Dulbecco's phosphate buffered saline

e$^-$ electrons

EELS electron energy-loss spectroscopy

EM electron microscopy

ESEM environmental scanning electron microscopy

FCS fetal calf serum

FLP fibronectin-like Protein

FRET Förster resonance electron transfer

GA Glutaraldehyde

GIF gatan imaging filter

GLC graphene liquid cell

Gly glycine

GFP green fluorescent protein

GO graphene oxide

GS goat serum

GSED gaseous secondary electron detector

HER human epidermal growth factor receptor

HPLC high performance liquid chromatography

LM light microscopy

LP-EM liquid-phase electron microscopy

MW molecular weight

NHS *N*-Hydroxysuccinimide

NA numerical aperture

NaN_3 sodium azide

NEAA non-essential aminoacids

NMR nuclear magnetic resonance

PBS phosphate buffered saline

PFA paraformaldehyde

PLL poly-l-lysine

QD quantum dot

RESOLFT reversible saturable optical linear fluorescence transitions

RFI relative fluorescence intensity

RNA ribonucleic acid

ROI region of interest

RT room temperature

SE secondary electrons

SEM scanning electron microscopy

SF serum-free

SFN superfibronectin

SiN silicon nitrite

SNR signal-to-noise ratio

STED stimulated emission depletion

STEM scanning transmission electron microscopy

STORM stochastic optical reconstruction microscopy

TEM transmission electron microscopy

TX texas red

$\boldsymbol{Z}$ atomic number

Contents

Abstract **II**

Kurzzusammenfassung **IV**

Acknowledgements **VI**

1 Introduction **1**

2 State of the Art **5**

2.1 Electron Microscopy 5

2.1.1 Liquid-Phase Electron Microscopy (LP-EM) 7

2.1.2 Environmental Scanning Electron Microscopy (ESEM) . . . 10

2.2 Benchmarking with Super-Resolution Microscopy and Cryogenic Electron Microscopy 12

2.2.1 Super Resolution Microscopy 12

2.2.2 Cryogenic Electron Microscopy (Cryo-EM) 13

2.3 Electron Scattering and Radiation Damage 13

2.3.1 Elastic Scattering 15

2.3.2 Inelastic Scattering 16

2.4 Graphene 19

2.4.1 Graphene in Biological Applications 20

2.4.2 Graphene as Sample Support Material for Electron Microscopy 21

2.5 Green Fluorescent Protein 22

2.5.1 Biological Applications 24

3 Material and Methods **27**

3.1 Material 27

3.2 Preparation of Working Solutions 31

3.3 Methods 33

3.3.1 Cleaning of Microchips 33

3.3.2 Labeling of Microchips with Green Fluorescent Protein . . . 33

3.3.3 Labeling of SKBR3 Cells with Green Fluorescent Protein . . 34

3.3.4 Assembly of Silicon Nitrite Liquid Cells 35

3.3.5 Preparation of Graphene Liquid Cells 36
3.3.6 Calculation of the Accumulated Dose and Electron Flux . . 37
3.3.7 Transmission and Environmental Scanning Electron Microscopy 38
3.3.8 Liquid Thickness Measurements via Electron Energy Loss Spectro-scopy 39
3.3.9 Fluorescence Microscopy and Data Analysis 41
3.3.10 Control Experiments 42
3.3.11 Labeling of Human Epidermal Growth Factor Receptor 2 . . 43
3.3.12 Graphene Coating 45
3.3.13 Scanning Transmission Electron Microscopy and Analysis . . 47

4 Electron Beam Damage of Green Fluorescent Protein in Liquid-Phase Electron Microscopy 48
4.1 Results 49
4.1.1 Control Experiments 49
4.1.2 Electron Beam Exposure of Green Fluorescent Protein in Liquid-Phase Transmission Electron Microscopy 53
4.1.3 Liquid Thickness of Graphene Liquid Cells 55
4.1.4 Electron Beam Exposure of Green Fluorescent Protein in Graphene Liquid Cells in Transmission Electron Microscopy 56
4.1.5 Comparison of the Electron Dose Tolerance of Green Fluorescent Protein in Graphene Liquid Cells and Silicon Nitrite Liquid Cells 60
4.1.6 Electron Beam Exposure of Green Fluorescent Protein in Environmental Scanning Electron Microscopy 63
4.2 Discussion 67
4.2.1 Electron Beam Damage of Green Fluorescent Protein in Liquid-Phase Electron Microscopy 68
4.2.1.1 Liquid-Phase Transmission Electron Microscopy . . 69
4.2.1.2 Environmental Scanning Electron Microscopy . . . 72
4.3 Conclusion 73

5 Electron Beam Damage of SKBR3 Cells Labeled with Green Fluorescent Protein in Liquid-Phase Electron Microscopy 75
5.1 Results . . . 76
5.1.1 Controls . . . 76
5.1.2 Labeled SKBR3 Cells in Liquid-Phase Transmission Electron Microscopy . . . 82
5.1.3 Labeled SKBR3 Cells in Environmental Scanning Electron Microscopy . . . 86
5.2 Discussion . . . 89
5.2.1 Liquid-Phase Transmission Electron Microscopy . . . 90
5.2.2 Environmental Scanning Electron Microscopy . . . 93
5.3 Conclusion . . . 94

6 Graphene Enclosure of Chemically Fixed Mammalian Cells for Liquid-Phase Electron Microscopy 96
6.1 Results . . . 98
6.2 Discussion . . . 101

7 Conclusion and Outlook 104

References 108

A Appendices 129
A.1 List of Figures . . . 129
A.2 List of Tables . . . 131
A.3 pH Measurements for PBS and HPLC-grade H_2O . . . 131
A.4 Calculation of the Ionic Strength . . . 132
A.5 Stage Shift . . . 132
A.6 Publications . . . 133

1 Introduction

The ability to image specimens beyond the resolution of visible light has been one of the greatest technological achievements of the last century, benefiting biological, medical and materials research. A transmission electron microscope, which used electrons instead of light, was first designed by Ernst Ruska and Max Knoll in 1931.[1] The higher resolution compared to conventional optical microscopy enabled imaging of nanometer-sized samples. Biological and medical research in particular benefited from the invention, as it became possible to resolve pathogens and proteins, many of which were previously invisible under optical microscopy.[2–5] **Figure 1.1** shows images of bacteria (**a**) and pox viruses (**b**), which were acquired by F. Krause and E. Ruska in the 1930s.[1,5,6]

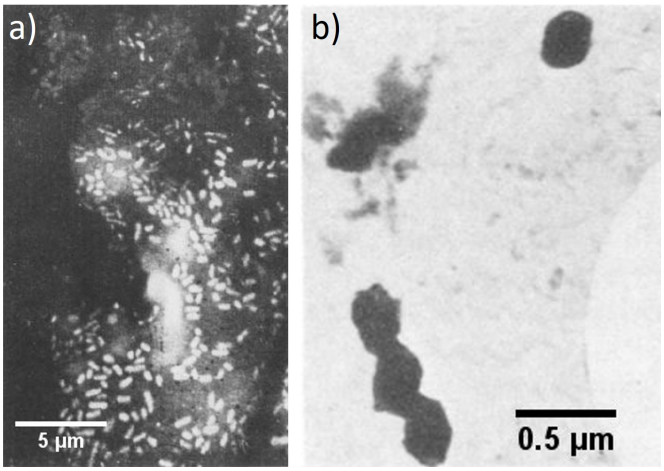

Figure 1.1: Electron microscopic images of biological specimens. a) Bacteria extracted from culture infusion and fixed with formalin. b) Pox viruses. Adapted by permission from Springer Nature: a)[6] © (1937) and b)[5] © (1939).

A few years after imaging the first biological specimens, applications of electron microscopy (EM) had proliferated to materials science, contributing to the understanding of various phenomena in thin metal foils or crystal defects.[7,8] Nowadays, electron microscopes have developed into important tools in broad areas of research as they add insights in biological samples and intrinsic material properties.[2,9] In addition, EM allows probing dynamic sample behaviors in-situ under mechanical deformations, in gaseous and liquid environments.[10,11] For the invention of this

powerful microscope and his research contributions in the field of electron optics, Ernst Ruska was awarded the Nobel Prize in Physics in 1986.[1]

The great interest and benefit of EM resulted from its much higher resolution compared to all previously known microscopic methods at that time.[3] Using electrons instead of light increased the resolution due to the smaller wavelength of electrons compared to visible light (five orders of magnitude). The resolution of EM is not only limited by the wavelength, but also by electron optics. The theoretical resolution of 2.2 Å of an electron microscope operated at 75 kV was already estimated by Ruska and Knoll in 1932.[3] However, inevitable spherical and chromatic aberrations in electromagnetic lenses caused a resolution of about 10 nm for the first electron microscopes.[6,12,13] Since then, improving lens optics and correcting aberrations have been important aspects of EM development. In the 1990s and early 2000s, major breakthroughs were accomplished with spherical aberration correctors, achieving sub-angstrom resolution.[14–16] Further improvement in lens optics and aberration correctors increased the resolution to 0.5 Å.[17,18]

The use of electron microscopes in biological research has contributed significantly to the understanding of organelle morphology, cell organization and interaction.[2,19] Future steps to advance research include the observation of processes in the native environment of biological samples at nanometer resolution.[2,20] However, various requirements of EM complicate the observation of intact biological specimens. Electron microscopes operate under high vacuum conditions to avoid scattering of beam electrons with air molecules. The vacuum is typically in the range of 10^{-3} Pa for scanning electron microscopes and 10^{-5} Pa for transmission electron microscopes.[8,21] Under these conditions, rapid water evaporation causes biological specimens to dry out and lose their composition and natural structure. Another aspect is the lack of imaging contrast of biological specimens as organic matter consists of light elements.[8] To overcome these problems, several techniques to stabilize biological specimens have been established. Specimens can either be frozen rapidly before imaging in cryogenic electron microscopy (cryo-EM) or dehydrated, stained, fixed, and embedded in resin. Both methods are used, but do not maintain a native environment for biological specimens and may cause artifacts from the preparation process.[22,23] To maintain a liquid environment, liquid-phase electron microscopy (LP-EM) techniques such as environmental scanning electron mi-

croscopy (ESEM) and liquid-phase transmission electron microscopy (TEM) have been developed.[11,24] For electron transmitting imaging techniques such as TEM and scanning transmission electron microscopy (STEM), samples must be thin to allow sufficient electron transmission for signal collection.[8,23] Whole cells and tissues exceed this thickness and, therefore, have to be sliced into thin sections using ultramicrotomes.[23,25]

Another challenge in EM of biological samples is the occurrence of electron beam damage. Negatively charged electrons interact with specimens, which can cause structural damage such as atomic displacement and radiolysis, generally referred to as radiation damage.[8] Radiation damage can hinder the examination of specimens, as damaged samples do not provide information. To image intact specimens in their native state, radiation damage needs to be limited to preserve the function and structure of the specimens. To ensure this, the electron dose at which radiation damage occurs has to be determined. Strategies to increase the electron dose tolerance of specimens include mitigation of radiation damage, for example, by using scavenging materials such as graphene. Damage mitigation is of general interest as it allows the resolution of nanometer-sized biological features without loss of information. Research on evaluating electron beam damage is a key step to understand underlying mechanisms and to further propose damage mitigation strategies.[26] Radiation damage also occurs in liquids, but damage mechanisms and electron dose tolerances for biological samples in liquid environments have not yet been fully explored.

The present work addresses the subject of electron beam damage in biological specimens in liquid. Green fluorescent protein (GFP) is used as a model protein and irradiated with different electron doses and fluxes in liquid environment. Damage mitigation is investigated using graphene as scavenging material. Radiation damage of chemically fixed SKBR3 cells is evaluated using GFP bound to actin-filaments and membrane proteins labeled with quantum dots (QDs). This thesis addresses the following questions:

- What is the impact of electron dose and electron flux on electron beam damage of GFP?

- What is the difference between the electron beam damage in TEM and ESEM?
- Does graphene as sample support mitigate electron beam damage?
- Can electron dose thresholds for single proteins be applied to more complex systems such as cells?

Chapter 2 of this thesis presents the theoretical background and state-of-the-art. The basic principle of EM is described, focusing on LP-EM, electron scattering and radiation damage. Benchmarking with cryo-EM and super-resolution microscopy is presented. Additionally, properties and applications of GFP and graphene are described. Experimental materials and methods are presented in **Chapter 3**. Sample preparation techniques, EM operation and data analyses are explained in detail. **Chapters 4 - 6** present the experimental work of this thesis. The electron beam irradiation of GFP in liquid-phase TEM and ESEM is described in **Chapter 4**. Electron dose, electron flux and acceleration voltage were varied. Damage mitigation was observed by changing the sample support from silicon nitrite (SiN) to graphene. **Chapter 5** presents the investigation of radiation damage of GFP bound to actin-filaments in fixed SKBR3 cells in liquid. The last experimental **Chapter 6** presents investigations of membrane proteins of fixed SKBR3 cells labeled with QDs. Here, radiation damage was examined based on the change of QD positions in graphene-coated and non-coated cells. Each chapter includes a discussion of the results presented in that chapter. Summary and outlook for further investigation of electron beam damage and damage mitigation on biological specimens are given in **Chapter 7**.

This thesis provides information about the electron dose thresholds of EM of biological specimens in their native, liquid environment. A guideline for the measurement of the electron dose in LP-EM is provided. In addition, damage mitigation for proteins in liquid is shown by encapsulating proteins in graphene. The results presented here provide a procedure for the investigation of biological materials such as proteins and fixed cells in LP-EM.

2 State of the Art

2.1 Electron Microscopy

Electron microscopy is mainly divided into two types: TEM and scanning electron microscopy (SEM). In TEM, a parallel electron beam is used to expose the sample, while in SEM, a focused electron beam (electron probe) scans the sample. A combination of both is STEM, in which the setup is similar to TEM, but the sample is scanned with a focused electron probe as in SEM. Some TEMs can be operated in probe mode (STEM), but dedicated STEM also exists. **Figure 2.1** illustrates the schematic setup of SEM (**a**), TEM (**b**) and STEM (**c**). The microscopes are equipped with an electron source where electrons are extracted from the cathode by an applied extraction voltage in the anode.[8] The electrons are accelerated, with accelerating voltages typically ranging from 500 eV to 30 kV in SEM and from 30 kV to 300 kV in TEM and STEM.[11] Electrons leaving the electron source in the primary electron beam are focused on the sample by a lens system. The condenser lens (CL) system is located after the electron source and controls the beam size. In TEM, which can be operated in STEM, the condenser lenses are necessary to form either a parallel electron beam for TEM or a fine probe for STEM.[27] In TEM, the specimen is located after the condenser lens and before objective (OL) and projector lenses (**Figure 2.1b**), whereas in SEM the specimen is located at the bottom of the whole lens system (**Figure 2.1a**). Additionally, scan coils are inserted in SEM to scan the sample with a focused electron probe. The setup in STEM is similar to TEM, but scan coils are also inserted here to scan the sample with the focused electron probe (**Figure 2.1c**).

Different signals are typically used for image formation in TEM and SEM. In TEM, electrons transmitted through the samples are detected, whereas backscattered electrons (BSE) and secondary electrons (SE) are usually detected in SEM (see **Section 2.3** for more detailed information). Transmitted electrons can be detected in SEM as well if the specimen is thin enough, however, better resolution can be obtained in higher-voltage TEM or STEM.[29] In STEM, SE and BSE can also be used for data acquisition, but higher resolution is achieved with the detection of transmitted electrons.[30] Annular dark field (ADF) detectors (see **Figure 2.1c**) are

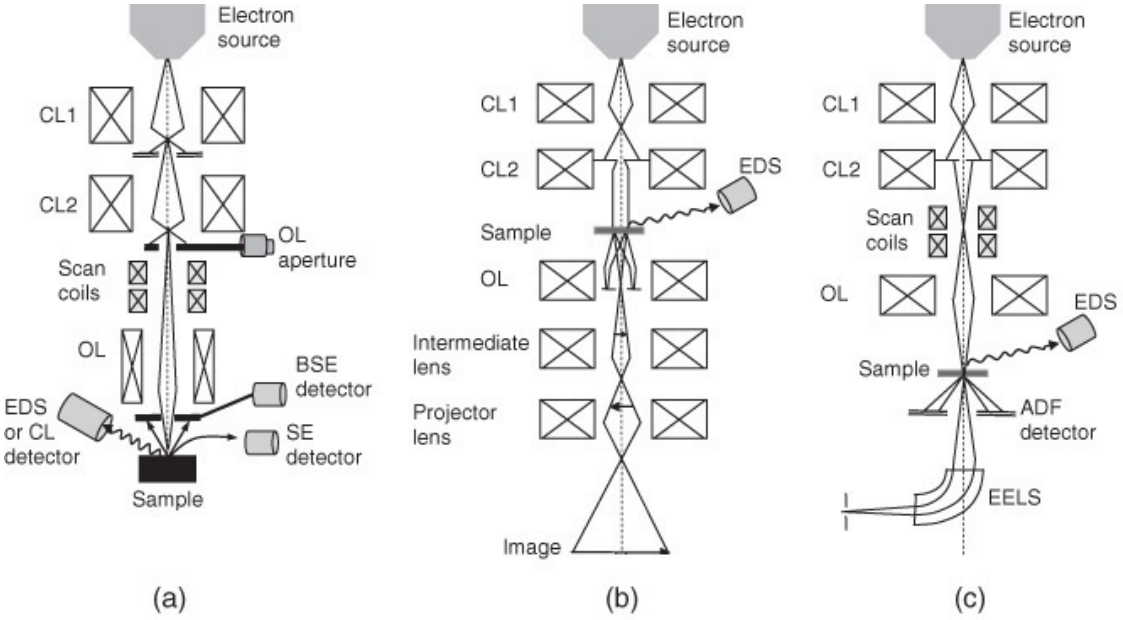

Figure 2.1: Schematic setup of electron microscopes. a) In scanning electron microscopy (SEM), the specimen is located at the end of the lens system. Scan coils are located after the condenser lenses (CL) to focus a fine electron beam that scans the sample. b) In transmission electron microscopy (TEM), the specimen is located after CL. The objective (OL) and projector lenses (PL) are located after the specimen. c) In scanning transmission electron microscopy (STEM), scan coils are inserted to scan the specimen with a focused electron beam. An annular dark field (ADF) detector is used for the detection of high-angle scattered electrons. Republished with permission of John Wiley & Sons - Books, from ;[28] permission conveyed through Copyright Clearance Center, Inc.

used in STEM to detect high-angle scattered transmitted electrons, which provide atomic number (Z) contrast.

As mentioned above, the resolution in optical light microscopy is limited by the wavelength of light. Resolution is defined as the minimum distance d that two particles must be apart to be distinguishable and is given by Rayleigh's criterion:[8]

$$d = 0.61\frac{\lambda}{n\sin\alpha} \tag{1}$$

where n is the refractive index, α is half the opening angle and λ is the wavelength. The resolution improves with decreasing wavelength and increasing numerical aper-

ture (NA) = $n\sin\alpha$. The wavelength of electrons is given by the De-Broglie-wavelength

$$\lambda_{deBroglie} = \frac{h}{\sqrt{2m_e \cdot e \cdot V}} \tag{2}$$

where $h = 6.6 \cdot 10^{-34}$ J·s is Planck's constant, $m_e = 9.1 \cdot 10^{-31}$ kg is the mass of an electron, $e = 1.6 \cdot 10^{-19}$ C is the elementary charge and V is the acceleration voltage.[8] If V increases, $\lambda_{deBroglie}$ (**Equation 2**) and d (**Equation 1**) decrease. For 200 kV, the wavelength of electrons is about 2.7 pm. Assuming NA = 0.4 and λ = 400 nm for visible light, d = 610 nm. Assuming the same NA, but with λ = 2.7 pm for 200 kV electrons, d = 4.1 pm, i.e. five orders of magnitude higher than for visible light. The theoretical resolution of 4.1 pm cannot be achieved until now which is due to low quality electromagnetic lenses in TEM with NA $\approx 10^{-2}$.[31] However, atomic resolution (1 Å) can be achieved in TEM.
In SEM, the probe size, which is limited e.g. by lens aberrations, sets the resolution. For modern instruments, the resolution is $<$ 1 nm.[29,32] This is valid for SE and BSE in thin specimens ($<$ 100 nm).[29] For bulk specimens, however, the resolution depends on the detected electrons. SE still provide similar high resolution, since SE emerge from near the surface. For BSE, the resolution is mostly limited by the interaction volume.[29] Due to the higher energy of BSE, they emerge from about half the penetration depth of the primary electron beam.[33] This leads to a larger interaction volume and a wider region from which BSE emerge than for SE, which reduces resolution.[34] As illustrated in **Figure 2.2**, the interaction volume increases with increasing E_0 and decreasing Z.

2.1.1 Liquid-Phase Electron Microscopy (LP-EM)

The observation of biological specimens in EM is particularly challenging as the samples need to withstand the high vacuum that is essential in electron microscopes to avoid scattering of electrons with air molecules. In addition, samples will dry out when exposed to the vacuum of an electron microscope. Therefore, biological sample preparation in EM traditionally includes dehydration, fixation, embedding, or freezing of the specimens.[23,27,35] For conventional TEM, samples are sliced in thin sections to allow sufficient electron transmission.[23] This approach has been

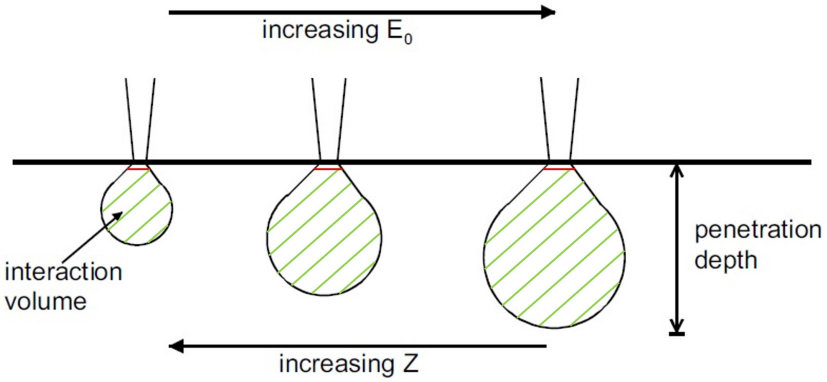

Figure 2.2: Dependence of the interaction volume in scanning electron microscopy (SEM) in bulk specimens. The interaction volume and the penetration depth of electrons in a bulk specimen in SEM increases with decreasing atomic number (Z) and with increasing electron energy E_0. The red line indicates the approximate origin depth of secondary electrons (SE) and the volume marked in green indicates the origin of backscattered electrons (BSE). Adapted by permission from Springer Nature: ,[33] © (2005).

successfully used in studies of the ultrastructure of biological cells and tissues. Through EM, many new insights in cell organization, cellular components and structures were gained and contributed to the understand of cellular functions.[23] However, this technique does not reflect biological samples under natural, liquid conditions and prevents the observation of dynamic processes which are of major interest in EM research.[24] LP-EM is a technique that allows visualization of samples in liquid using electron microscopes. The most challenging aspects are separating the liquid samples from the vacuum of the microscope and achieving nanometer resolution.[36,37] The resolution decreases as the sample thickness increases, so the liquid thickness must be sufficiently thin.[36,37]

LP-EM has advanced to an important method in many fields of research including electrochemistry, biomineralization and nanoparticle self-assembly.[26] Multiple preparation techniques for LP-EM have been developed so far. **Figure 2.3** illustrates the cross section of a so-called liquid cell containing nanoparticles in liquid. Liquid cells are prepared to separate the sample from the vacuum in a sealed liquid system at atmospheric pressure.[38,39] In most cases, liquid cells consist of amorphous SiN deposited on a silicon support as electron transparent membrane material.[36,37]

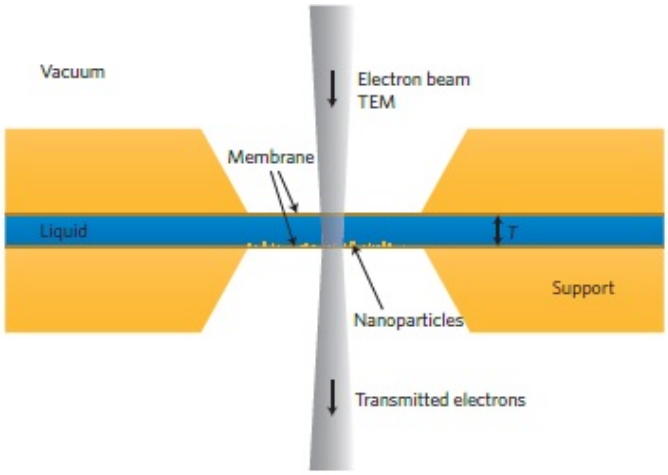

Figure 2.3: Silicon nitrite (SiN) liquid cell in transmission electron microscopy (TEM). The liquid sample is enclosed in a sandwiched structure consisting of two SiN microchips. Liquid and nanoparticles are introduced either by flowing through a tubing system or by dispensing a droplet on the microchip before closing the liquid cell. Reprinted by permission from Springer Nature: Nature Nanotechnology [11] © (2011).

For the preparation of liquid cells, physical spacers can be included to regulate the liquid thickness. However, the liquid thickness can vary due to bulging of the SiN membrane when exposed to vacuum as a result of the pressure difference.[37,40,41] One of the microchips is inserted in the sample holder and a second microchip is placed upside down on the first microchip so that the two SiN membranes overlap. The liquid can be introduced either by dispensing a drop on the first microchip before closing the liquid cell, or by a microfluidic system connected to the sample holder. A lid with sealing o-rings is used to close the liquid cell. Various designs of liquid cells are available in which microchips and holders can be fabricated, for example, to integrate temperature control elements.[11,36,37]

An alternative approach for LP-EM is the enclosure of liquid samples in graphene liquid cells (GLCs). **Figure 2.4** illustrates preparation methods for GLCs. The sample is dispensed on a graphene-coated TEM grid and either coated with a graphene sheet via loop-assisted transfer (**Figure 2.4a**) or by picking up a graphene sheet via touch-down (**Figure 2.4b**). A sandwich can be prepared by encapsulating the sample between two graphene-coated TEM grids (**Figure 2.4c**). Several benefits of using graphene rather than SiN have been demonstrated in LP-EM

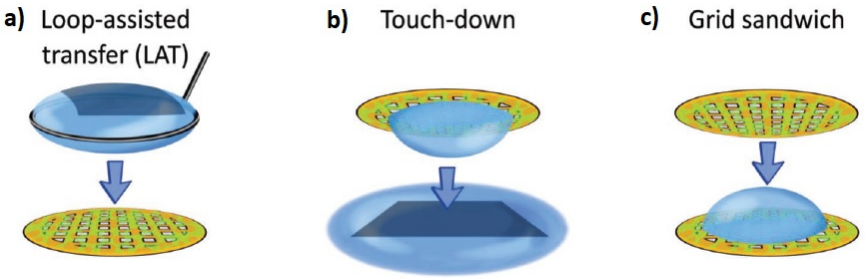

Figure 2.4: Preparation methods for graphene liquid cells (GLCs). a) Loop-assisted transfer of graphene on a graphene-coated transmission electron microscopy (TEM) grid. The bottom grid is coated with a graphene sheet by a loop enclosing liquid between the grid and the graphene. b) The graphene-coated grid with the sample is placed upside down on a graphene sheet floating on liquid. c) The graphene-coated TEM grid with the sample is closed with another graphene-coated TEM grid to form a sandwich. Republished with permission of John Wiley & Sons - Books, from ;[46] permission conveyed through Copyright Clearance Center, Inc.

applications. Biological samples coated with graphene show reduced motion as a result of reduced charging.[42,43] Graphene acts like a scavenger for radicals created in EM and hence reduces radiation damage.[26,42–44] In addition, graphene also provides a thinner layer than SiN membranes which results in better signal-to-noise ratio (SNR) and enhanced resolution (see also **Section 2.4**).[45]

2.1.2 Environmental Scanning Electron Microscopy (ESEM)

Another LP-EM method is a variation of SEM called environmental scanning electron microscopy (ESEM). The setup is similar to conventional SEM, but the specimen chamber is operated at low vacuum, typically between 100 - 1300 Pa. The specimen chamber is filled with vapor which provides a saturated atmosphere. In most cases, water is used.[47,48] The chamber and the electron gun need to be separated to maintain a high vacuum in the electron gun and a low vacuum in the chamber. To achieve this, several pressure-limiting apertures and different pumping systems for chamber and gun are installed in ESEM compared to conventional SEM.[37,49,50]

Figure 2.5a illustrates the signal generation in ESEM. As with SEM, the sample is irradiated with the primary electron beam, generating SE and BSE (grey and

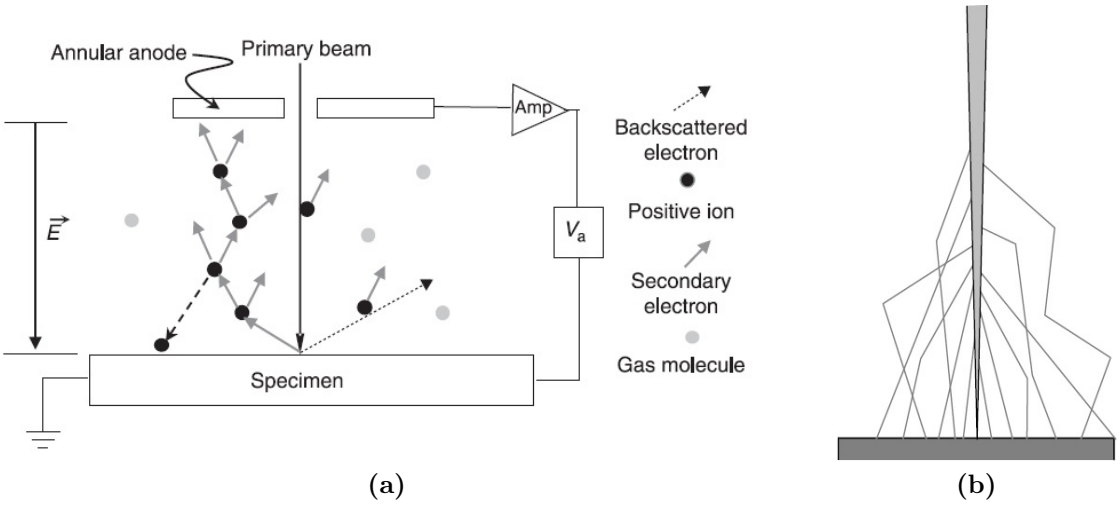

Figure 2.5: Signal generation in environmental scanning electron microscopy (ESEM). a) The primary electron beam creates secondary electrons (SE) in the specimen upon radiation. SE interact with gas molecules and create more SE which amplify the signal and ionize the gas molecules. These positively charged gas molecules can neutralize the charge created in the specimen due to the interaction with the primary electron beam. b) Beam spreading of the primary electron beam with gas molecules. Reprinted from [48] © (2013), with permission from Elsevier.

black arrows, respectively). However, unlike conventional SEM, these electrons collide with gas molecules in the atmosphere and generate more SE, leading to a cascade of SE, which amplifies the signal. For the operation in gaseous conditions special gaseous secondary electron detectors (GSEDs) have been developed with low positive potentials of typically 300 - 500 V.[51]

SE not only amplify the signal, but also ionize gas molecules (grey dots). Positively charged ions (black dots) can compensate the negative charge generated in the sample to mitigate charging effects.[29,47] The charge neutralization enables observation of non-conductive materials and is an advantage of ESEM over SEM.[48,52] This also facilitates sample preparation and avoids artifacts caused by drying or freezing.[48]

However, not only SE, but also the primary electron beam can interact with gas molecules before encountering the sample as depicted in **Figure 2.5b**. Therefore, the beam intensity in a gaseous environment may be reduced compared to the measured intensity.

2.2 Benchmarking with Super-Resolution Microscopy and Cryogenic Electron Microscopy

2.2.1 Super Resolution Microscopy

In contrast to conventional TEM, dynamic and live processes can be observed using optical microscopy. Optical microscopy methods have improved over the years, aiming to image samples with a resolution close to the atomic resolution achievable in EM. In general, such super resolution microscopy methods can be classified by the image acquisition. Reversible saturable optical linear fluorescence transitions (RESOLFT) techniques include deterministic functional techniques such as stimulated emission depletion (STED), ground state depletion, and saturated structured-illumination microscopy. In RESOLFT, two states of the fluorophores are used: the dark state where the fluorophores do not emit photons and the bright state where photons are emitted. In STED, this is achieved by using two laser beams, one to excite the fluorophores and another doughnut-shaped laser beam that reduces the probe size and mutes fluorophores.[53] In this way, a smaller amount of fluorophores are excited which increases the resolution. The first experiments using STED showed a resolution of 35 nm, which was further improved to 1 - 3 nm using a recently developed variant of STED called minimal STED (MINSTED).[53,54]
Besides deterministic techniques, there are some stochastic functional techniques available. For example, in stochastic optical reconstruction microscopy (STORM), multiple cycles are imaged, in which fluorescent dyes are switched from fluorescent and dark state using red and green lasers.[55] In each cycle only a fraction of fluorophores is excited and one image is taken.[55] The final image is reconstructed from all imaging cycles with a resolution of about 20 nm.[55] Compared to conventional optical microscopy, the resolution is not limited by the wavelength of light but by the number of photons that are excited in each cycle.[55]
Although super resolution microscopy techniques have improved, some drawbacks remain. The resolution is still at least one order of magnitude lower than with EM ($\sim$ 1 nm for MINSTED vs 1 Å in EM). Specific fluorophores are required for super-resolution techniques such as STORM and photoactivated localization microscopy.[56] Phototoxicity and photobleaching of the fluorophores are likely to occur after intense beams and multiple imaging cycles. Some methods require imaging

close to the coverslip due to low z-axis resolution, therefore imaging is limited by the setup. For RESOLFT methods, high-intensity pulsed lasers are required that can cause irreversible sample damage.[55]

2.2.2 Cryogenic Electron Microscopy (Cryo-EM)

Cryo-EM provides imaging of biological samples under near native conditions. In cryo-EM, amorphous ice preserves the structure of biological specimens. Samples are plunge frozen in liquid ethane or propane and observed in EM at temperatures around 80 K using liquid nitrogen.[57,58] Cryo-EM has become a very important characterization technique in structural biology, since it reduces radiation damage and offers much higher resolution compared to traditional characterization techniques such as nuclear magnetic resonance (NMR) spectroscopy and X-ray crystallography.[59,60] Recently, atomic resolution was achieved in single-particle cryo-EM.[61,62] Early events can be studied with time-resolved cryo-EM. Two components are mixed on a microfluidic chip to initiate reactions. The reaction can be stopped at any time by spraying the product onto a grid and freezing it. This way, time-resolved investigations of fast processes at different time points are possible.[63,64] While sample preparation for conventional TEM can change the structure, shape and morphology during the staining and dehydration process, sample preparation for cryo-EM preserves the structural integrity of the sample.[65] The radiation sensitivity of the sample decreases due to the much lower temperatures in cryo-EM.[19,66] The major limitation of cryo-EM is that the samples are frozen, which precludes the observation of dynamics and live processes.[36] In addition, the samples must be examined at low temperatures around 80 K.[58] The freezing process can create artifacts such as ice contamination and crystalline ice formation.[67,68] Therefore, cryo-EM is mainly used as a high-resolution technique for structural elucidation in biology.[69]

2.3 Electron Scattering and Radiation Damage

Electrons can be scattered either elastically (electron-nucleus interaction) or inelastically (electron-electron interaction) in a material.[33,70] In inelastic scattering processes, the energy is transferred and most of the energy is converted to heat

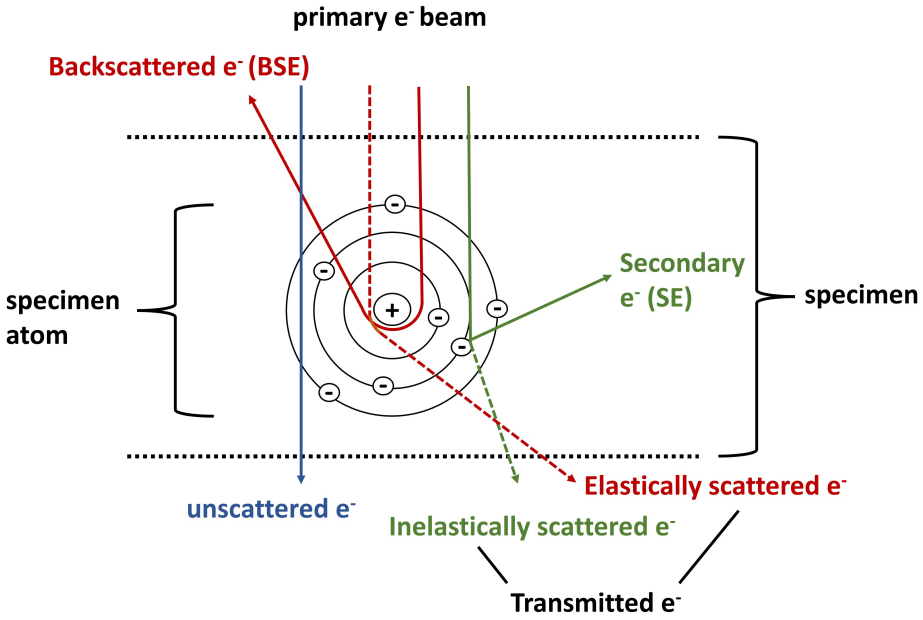

Figure 2.6: Scattering of incident beam electrons in an atom of a specimen. Electrons can be attracted by the positively charged nucleus of the atom and scattered elastically at high angles >90° (red arrow, backscattered electrons (BSE)) or at angles <90° (red dashed arrow, forward scattered electrons). Beam electrons can also interact with electrons of the atom and be scattered inelastically at low angles generating secondary electrons (SE) (green arrow). Elastically and inelastically forward scattered electrons that exit the specimen are called transmitted electrons (red and green dashed arrows). Some beam electrons exit the specimen unscattered (blue arrow).

and the emission of X-rays and electrons.[29,70,71] In elastic scattering processes, the kinetic energy of the system, i.e. of the incident electron plus the nucleus, is conserved. Energy transfer still occurs, but for electrons scattered at lower angles and with low electron energy, the energy transfer is negligible because the mass of the nuclei is much greater than the mass of the electrons.[27,29,72]

Figure 2.6 shows different scattering mechanisms that occur in EM when electrons interact with an atom of a specimen. Electrons can be attracted by the positively charged nucleus and reflected at high angles (>90°).[2,33] Those electrons are called BSE (**Figure 2.6 red arrow**). Electrons attracted by the nucleus, but scattered at angles <90°, transmit the atom and are called forward scattered

electrons (**Figure 2.6 red dashed arrow**).[2,33] Both, BSE and forward scattered electrons occur after elastic scattering events.
Electrons encountering the specimen can also interact with the electrons in the atomic shells and are then scattered at angles $<1°$. As they transfer some energy during the scattering process, these electrons are inelastically scattered. Those electrons are also scattered in the forward direction and exit the specimen as transmitted electrons (**Figure 2.6 green dashed arrow**). Transmitted electrons, both elastically and inelastically scattered, are used for signal generation in the TEM.[8,73]
The energy transferred in the interaction between incident electrons and electrons in atomic shells can also excite atomic electrons. Those excited electrons are ejected from their position and exit the specimen as SE with low energies $\leq 50\,\mathrm{eV}$ (**Figure 2.6 green arrow**).[8,29]
Some electrons do not encounter any scattering events when traveling through the sample and exit the specimen unscattered (**Figure 2.6 blue arrow**). The thinner the sample, the more unscattered electrons transmit.
Although EM is extremely useful because it provides nanometer-scale information, electron scattering can damage the sample. This damage can limit imaging and analyses such as spectroscopy. Understanding radiation mechanisms is the key to reduce the damage on the specimen and to ensure imaging and analysis without artifacts. Radiation damage can generally be divided into two categories based on the scattering mechanisms: damage caused by elastic or inelastic scattering. In the following chapter, mechanisms of elastic and inelastic scattering will be examined in more detail.

2.3.1 Elastic Scattering

Elastic scattering is the most important scattering interaction to generate diffraction pattern and phase contrast in STEM and TEM and BSE contrast in SEM.[27,70,74] For high Z elements, more BSE reach the detector leading to higher signals that appear brighter than lower Z elements.[2] This characteristic makes BSE a useful tool for mapping materials according to their composition.[2] The scattering probability of an electron is given by the differential elastic scattering cross section in units of area per solid angle and is given by [27,75]

$$\frac{\mathrm{d}\sigma_{el}}{\mathrm{d}\Omega} = \frac{4Z^2R^4(1+\frac{E}{E_0})^2}{a_0^2}\frac{1}{\left[1+(\frac{\theta}{\theta_0})^2\right]^2} \tag{3}$$

where Ω is the solid angle, Z the atomic number, E the total energy, E_0 the beam energy in kV, $\mathrm{a}_0 = 0.5\,\text{Å}$ the Bohr radius, θ the scattering angle im mrad, $\theta_0 = \frac{\lambda}{2\pi R}$ the characteristic angle in mrad, and $R = a_0 Z^{-1/3}$. $\mathrm{d}\sigma_{el}/\mathrm{d}\Omega$ scales with Z^2 so it increases for increasing Z.[27,75]

The interaction of electrons with atomic nuclei can cause atom reposition. During the scattering process, high-angle elastically scattered electrons can transfer some energy to the atomic nucleus.[76] Every material has a critical energy E_c at which atoms are displaced from their original position.[77] If the transferred energy exceeds E_c, the atom is ejected from the lattice and creates point defects.[27,75–77] The damage is called atomic displacement or knock-on damage. The ejection of the atom can occur at the surface of the specimen, which is called sputtering.[8] As the electron energy decreases, the knock-on cross section becomes smaller, so knock-on damage can be reduced by lowering the radiation energy below E_c.[8,76,77] In practice, acceleration voltages above 100 kV are expected to cause knock-on damage in specimens.[70] Therefore, knock-on is mainly present in TEM and less present in SEM as the acceleration voltages are typically too low (up to 30 kV).[70]

2.3.2 Inelastic Scattering

In contrast to elastic scattering, a fraction of the kinetic energy are converted in inelastic scattering processes.[27] Outer-shell electrons are weakly bound and can be easily ejected as SE when beam electrons interact with an atom. Due to their low energy ($\leq 50\,\text{eV}$), SE can undergo more scattering events on their way through the specimen. This way, SE emerging from deeper in the sample usually get absorbed and do not reach the detector.[33] Therefore, SE that generate signal usually originate from near the surface of the specimen (<20 nm for insulators and ≈5 nm for metals).[33,78] SE provide important information about surface characteristics of the specimen but do not contain any elemental information.[8,33] Signals based on SE are the standard imaging signals used in SEM.[33]

Characteristic inelastic scattering signals can be detected with analytic methods.

Characteristic X-rays and electron energy-loss spectroscopy (EELS) give important information about the composition of materials.[8] The primary beam electrons lose energy during the interaction. In STEM, the energy loss can be detected via EELS. Characteristic X-rays arise from the excitation of an atom caused by the ejection of an electron that leaves a hole in the inner shell of the atom. This hole needs to be filled with an electron from a higher energy level which releases characteristic X-rays with a certain energy. In both, EELS and X-rays, the detected signals are unique for each atom and therefore those methods are used for the elemental characterization of materials.[8,33] Another mechanism is the ejection of Auger electrons. In this case, the excited atom does not fill the hole in the inner shell, but returns to its ground state by ejecting another electron, called the Auger electron.[8,33] Auger electrons are used to determine the chemical composition of specimen surfaces.[33]
As mentioned above, parts of the kinetic energy are converted to atom-electron excitations, heat or vibrations in inelastic scattering processes.[27,70] The scattering itself is concentrated into much smaller angles (<1°) than elastic scattering.[27,33] The inelastic scattering cross section is given by [27]

$$\frac{\mathrm{d}\sigma_{inel}}{\mathrm{d}\Omega} = \frac{(1+\frac{E}{E_0})^2}{4\pi^4 a_0^2 q'^4} Z \left[1 - \frac{1}{(1+4\pi^2 q'^2 R^2)^2}\right] \tag{4}$$

with q' the scattering vector. Because σ_{inel} scales linearly with Z and σ_{el} scales quadratically with Z (see **Equation 3**), inelastic scattering is more dominant in low Z elements, while elastic scattering dominates in high Z elements.[8,27,75] **Figure 2.7** illustrates the dependence of the scattering cross sections on Z. The ratio for inelastic and elastic scattering cross section $\sigma_{inel}/\sigma_{el}$ over the beam energy is shown for different elements. If $\sigma_{inel}/\sigma_{el} > 1$, σ_{inel} is more dominant and σ_{el} is more dominant if $\sigma_{inel}/\sigma_{el} < 1$. σ_{el} is more dominant for higher Z elements for all beam energies.
Similar to elastic scattering, inelastic scattering events can also cause radiation damage. Most of the transferred energy is converted to heat, which potentially leads to electron ejection in solid materials.[27,75] Options to reduce radiation damage in solids include cooling the specimen and effective dissipation of thermal energy.[75] The energy transfer, typically in the range of 20 eV, results in excitation and ionization of the specimen.[37,75] This leads to the breaking of bonds and, in

liquids, to the formation of reactive radicals such as OH· or H·, which alter the chemical environment of the sample.[27,37,75,79] These radicals can react with other molecules in the specimen and create structural damage while bond ruptures cause mass loss.[70]

The radiolytic cross section is given by

$$\sigma_R = 7 \cdot 10^6 \xi \frac{Z}{E_d} \tag{5}$$

where E_d is the threshold energy for displacement and ξ the radiolytic efficiency.[75] ξ is defined as the number of scattering events that are needed to create damage and is given by the ratio of the damage cross section σ_D (reciprocal of the characteristic dose D_c) and the average cross section per atom $\langle\sigma_i\rangle$: $\xi = \frac{\sigma_D}{\langle\sigma_i\rangle}$.[80] If $\xi < 1$ more than one collision is needed to damage the specimen. For aromatic molecules, usually $\xi < 1$ because the molecules are stabilized by the delocalized π-electrons of the benzene rings.[27,71,80] Aliphatic amino acids show higher numbers for ξ and are therefore more sensitive to beam damage. In those molecules, a single scattering event can destroy the whole structure.[80] Glycine for example, has a radiolytic efficiency of $\xi \approx 40$.[80]

Conductive materials contain a high number of delocalized electrons that can

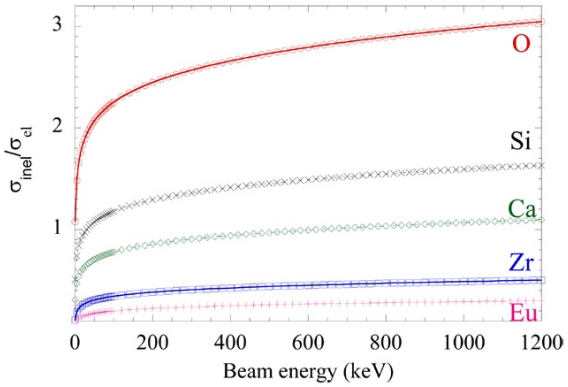

Figure 2.7: Ratio for inelastic and elastic scattering cross section. The ratio of the inelastic (σ_{inel}) and the elastic (σ_{el}) scattering cross section is shown over the beam energy for different elements. For $\sigma_{inel}/\sigma_{el} > 1$, σ_{inel} is more pronounced and for $\sigma_{inel}/\sigma_{el} < 1$, σ_{el} is more dominant.[75] © IOP Publishing. Reproduced with permission. All rights reserved.

rapidly fill holes caused by inelastic scattering. This stabilizes the system and reduces radiolysis so that knock-on damage remains as the main damage mechanism.[75,76,81] In contrast, for insulators and organic specimens, an atom could remain in the localized excitation state for long enough to eventually cause bond rupture.[75,76] In organic specimens, the damage cross section for radiolysis is much larger than that for atomic displacement. Knock-on damage is still present in organic specimens, but the majority of beam damage is caused by inelastic scattering events.[76]

Mitigating radiation damage in EM is of general interest to increase the dose tolerance of specimens and image specimens without loss of information. Cooling the specimens can help to reduce thermal vibrations and heat induced damage as well as radiolysis.[27,75] Inelastic scattering can be reduced by increasing the acceleration voltage.[27,82] Materials such as graphene can scavenge radicals and mitigate electron beam damage.[26,44] Substitution of elements in organic samples or coating with conductive layers can also reduce radiolysis.[27] In addition, some low-dose microscopy methods, such as dose fractionation and sparse imaging, can be used to reduce the electron dose deposited on the sample.[82,83]
Notably, all scattering events including scattering cascades occur simultaneously at multiple atoms and electrons. This complicates the entire scattering process and the understanding of radiation damage.

2.4 Graphene

In 2004, Novoselov *et al.* isolated the first single-layer two-dimensional carbon crystal from graphite by exfoliation.[84] The single-layer crystal called graphene is the thinnest nanomaterial known ($\sim 3\,\text{Å}$) and consists of a single layer of carbon atoms arranged in a honeycomb structure.[85–87] Each carbon atom is surrounded by three other carbon atoms at an angle of 120°.[88] The sp^2-hybridized orbitals of the carbon atoms form three strong, covalent, in-plane σ-bonds with three localized electrons and one weaker, out-of-plane π-bond with one delocalized electron.[89–91] Graphene is mechanically robust and electrically conductive and can be produced by top-down or bottom-up synthesis such as exfoliation and chemical vapor depo-

sition.[43,89,92]

Unlike other semiconductors, there is no band gap between the conduction and valence bands in graphene.[87,93] However, when an electric field is applied perpendicular to the graphene layers, a band gap develops.[94] This allows tuning of the electronic properties of graphene.[91,93,94] The band gap can also be tuned by controlling the size of graphene. In addition, limiting the width of graphene to e.g. 100 nm such as in graphene nanoribbons, the electronic properties are highly dependent on the edge configuration.[95]

Compared to carbon nanotubes (CNTs) and fullerenes, the surface of graphene sheets is larger and both sides of the sp^2 hybridized carbon atoms are exposed to the surrounding.[96,97] Graphene is naturally hydrophobic, but can be functionalized to increase dispersibility in solution.[86,87,98] Contradictory studies on the toxicity of graphene-based nanomaterials were reported.[96] Toxicity appears to be dependent on the graphene material used, the concentration, the model (*in vivo* or *in vitro*) and surface functionalization.[99] However, cytotoxic effects are possible due to chemical and metal residues from the preparation process.[89] Nevertheless, functionalization of graphene materials can reduce toxic effects and increase dispersibility.[89,96]

The implementation of graphene into many research fields has developed fast as the methods to produce high-quality graphene are relatively cheap and simple.[100] With its high mechanical strength, high electronic and thermal conductivity, flexibility and impermeability to liquids and gases, graphene is a unique material than can substitute many materials and offers new applications.[100,101]

2.4.1 Graphene in Biological Applications

The extraordinary properties of graphene and graphene-based materials also opened up the possibility of biological and biomedical applications. Among others, areas of interest include biosensing, drug delivery and photothermal therapy.[92,102–104] CNTs have already been investigated on their biomedical application, but the higher surface area of graphene compared to CNTs and fullerenes proposes more efficient surface functionalization to modify its biological properties and reduce toxicity.[92,96] Graphene oxide (GO) shows reduced toxicity and increased dispersibility and is often used for biological applications although it shows an increased num-

ber of structural defects.[89] However, surface functionalization is crucial to reduce the hydrophobicity of graphene and GO and therefore increase the stability in physiological media by loading hydrophilic agents.[89,92] Functionalizing GO, for example, with polyethylene glycol has shown reduced toxicity and increased biocompatibility.[92,96,98] It is possible to functionalize peptides, aptamers and nucleic acids followed by materials such as nanoparticles as well as biomolecules such as deoxyribonucleic acid (DNA) to create biosensors.[89,104,105] Graphene has strong interactions with DNA and ribonucleic acid (RNA) which makes it a possible protective carrier against DNAse and RNAse in gene delivery.[89] Graphene has been used as biosensor for the detection of DNA sequences with high sensitivity, high selectivity, and low costs, hence providing a simple and accurate method for the detection of diseases.[104,106]

Through surface functionalization, graphene provides the potential of a highly efficient drug carrier for nanomedicine.[89] Functionalization is required to load graphene flakes and nano-GO with drugs, such as water-insoluble and hydrophobic chemotherapeutics and anticancer drugs.[89,103] Graphene can efficiently convert light into thermal energy so it has been used for photothermal therapy, for example, for *in vitro* killing of cancer cells using near-infrared light.[89,92] Many other applications of graphene and graphene-based nanomaterials such as tissue engineering or drug delivery are of great interest and are currently under investigation.[102,107]

2.4.2 Graphene as Sample Support Material for Electron Microscopy

In EM, graphene was investigated as an alternative sample support to substitute SiN membranes and carbon-coated TEM grids. Microchips can be fabricated with SiN membranes of about 5 nm thickness. These microchips are robust, biocompatible and of homogeneous thickness.[38] For the preparation of biological samples, microchips are easier to handle compared to mechanically unstable TEM grids.[38] However, these microchips are at least one order of magnitude thicker and less thermally and electrically conductive compared to graphene. TEM grids made of various metals are commercially available with different support material such as amorphous carbon. Amorphous carbon is very thin, however, its surface is electrically insulated and does not show significant conductivity for thin layers.[108] The

background signal of amorphous carbon increases with increasing magnification and is therefore not suitable for high-resolution imaging of low-contrast materials.[108] Graphene-based materials provide ultra-thin sample supports for EM. Spatial resolution and SNR can be increased about 100 % compared to carbon-based and SiN sample supports.[20,44,45,108] Graphene itself exhibits a weak contrast that allows imaging of light elements that is usually affected by the background signal of amorphous carbon.[99,109] Since graphene has a periodic lattice and is only one carbon atom thick, it can be easily distinguished from the sample of interest.[108,110] Compared to amorphous carbon, its electrical conductivity is about six orders of magnitude higher.[86,108] The sp^2 domains of graphene can scavenge radicals that are formed upon electron beam irradiation and transfer electrons to the outside.[44,111] The use of graphene as support material showed reduced radiation damage in EM.[20,26,44] Due to the high thermal and electrical conductivity of graphene, heat and charge accumulation during electron beam irradiation can be reduced.[86,110,112] Since graphene is impermeable to gases and liquids and can mitigate electron beam damage, studies of liquid samples enclosed in graphene have drawn great interest.[20,26,101,113] Owing to its enhanced SNR, damage mitigation, low background signal, and impermeability, graphene remains to date the most promising sampling candidate for observing biological and low Z-materials in their native environment.[20] Research on biological materials encapsulated in GLCs continuously delivers promising results, but is still ongoing and needs further improvement.

2.5 Green Fluorescent Protein

Osamu Shimomura was the first who isolated the bioluminescent protein Aequorin from the green fluorescent jellyfish *Aequorea victoria* in the early 1960s.[114] In the presence of calcium, aequorin emits blue light, however, the jellyfish fluoresces green.[114] After further investigation, another protein involved in fluorescence called GFP was identified. The excitation spectrum of GFP overlaps with the emission spectrum of aequorin, which excites GFP and causes the green fluorescence of the jellyfish.[115–117]

The first results on the molecular structure of GFP were reported in 1996 by Yang *et al.* for wild-type GFP and Ormö *et al.* for mutated GFP.[118,119] The protein

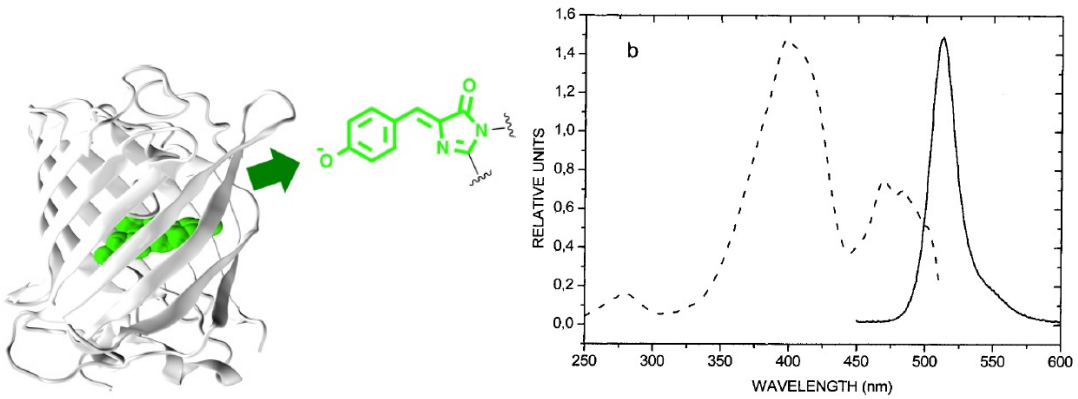

(a) (b)

Figure 2.8: Molecular structure, excitation and emission spectra of green fluorescent protein (GFP). a) Molecular structure of enhanced GFP with the alpha-helices arranged in a cylindrical β-barrel structure surrounding the chromophore marked in green in the center. The chemical structure in green presents the structure of the chromophore. Adapted from.[122] b) GFP excitation and emission spectra. The dashed line shows the excitation spectrum of purified GFP with maxima at 395 nm and 470 nm. The solid line depicts the emission spectrum of GFP with a peak at 509 nm. Reprinted from [123] © (1998), with permission from Elsevier.

consists of 238 amino acids and a cylindrical β-barrel structure which encloses the covalently bound chromophore as shown in **Figure 2.8a**.[119–121]

In wild-type GFP, the fluorophore is formed by the cyclization of Tyr66 with the neighboring Gly67 and Ser65 in an autocatalytic process.[117,119] The location of the chromophore in the barrel provides increased photostability compared to other dyes.[122,124,125] Wild-type GFP absorbs blue light with a maximum at 395 nm and a smaller peak at 470 nm and emits green light with a peak at 509 nm as shown in **Figure 2.8b**.[117,126]

No co-factors are required for the fluorescence of GFP, which attracted great interest in the protein.[123,127,128] It is non-toxic and can penetrate organisms without permeabilization, allowing imaging of living tissues.[127,129] GFP can fuse with structures in organisms to track their movement without altering their original location and function.[127,128] The discovery that GFP is genetically encoded and can be functionally expressed in, for example, *E.coli* enabled the development of mutants.[117,127,130] The protein was mutated to improve fluorescence and change the

excitation and emission of the chromophore to different wavelengths so that nowadays the GFP family includes many fluorescent proteins, emitting at various wavelengths.[131,132] GFP retains its fluorescence after fixation with paraformaldehyde (PFA), which, however, vanishes after denaturation of the protein.[117,128,133] For some time, denaturation of GFP was considered irreversible, but it has been reported that fluorescence can be retrieved if the β-barrel structure can be restored.[133]

2.5.1 Biological Applications

Since it was found that GFP only requires ambient oxygen but no co-factors to fluoresce and is non-toxic to most organisms, it has been widely used in biology and related fields.[117,123,134–136] GFP has become such an invaluable resource that it is not possible to mention all applications here. Among others, it can be used as a reporter gene, for visualization of whole organisms, and as a biosensor.[137] Some examples of previous research with GFP include the detection of the presence of calcium. Genetically encoded calcium indicators such as GFP-based GCaMP are used to detect neuronal activity via the presence or absence of calcium and to monitor the activation of signaling pathways.[138–142] Protein-protein interactions were studied using GFP-based Förster resonance electron transfer (FRET) analysis to gain insights into signaling cascades, proteolysis, cell cycle control, and distance measurements in living cells.[128,143]

However, detection of biological activity with GFP is still limited. High concentrations of GFP are required to detect beyond the autofluorescent background signal. In addition, oxygen is required for GFP fluorescence, which hampers the study of anaerobic organisms. Transcription into a fluorescent protein takes several hours, making early events elusive.[119,137] Fluorophore formation is quite thermosensitive and inactive aggregates with lower fluorescence intensity are formed above 20 °C.[119,144]

Fortunately, the location of the fluorophore within the cylindrical structure suggests that some side chains of the amino acids could be mutated to increase fluorescence intensity and accelerate fluorophore formation.[119,145,146] For example, about fourfold faster fluorophore formation and increased fluorescence amplitude at an excitation wavelength of 488 nm and an emission wavelength of 510 nm was reported with

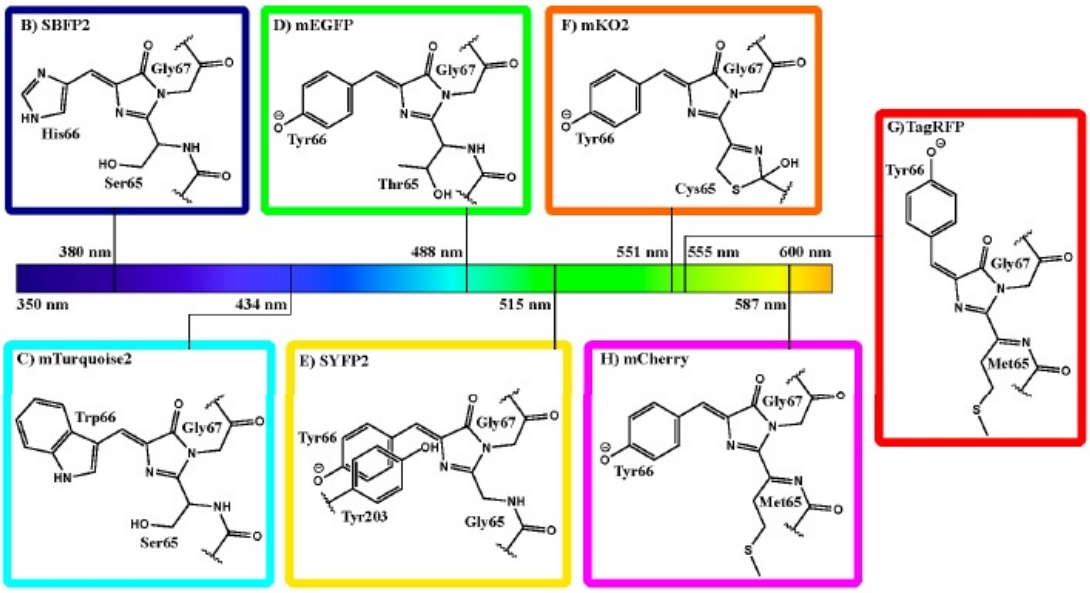

Figure 2.9: Chromophores and emission wavelengths of various fluorescent proteins. Chromophores of different fluorescent proteins are shown according to their emission wavelength. Each chromophore consists of a variable amino acid, an aromatic amino acid and glycine. Reprinted from.[131]

the mutation of Ser65 to threonine which is widely used as enhanced-GFP.[125,145,147] The discovery that Tyr66 in the fluorophore of GFP can be replaced by any aromatic amino acid and still emit fluorescence made it possible to tune the emission wavelength of the protein. Therefore, a number of fluorescent proteins such as cyan fluorescent proteins (CFP) and blue fluorescent proteins (BFP) now belong to the GFP family.[124,148] Some examples including the structure and wavelength of their chromophores are shown in **Figure 2.9**. The variety of fluorescent proteins allows labeling of multiple structures and simultaneous visualization under fluorescence microscopy.[131]

As described in **Section 2.3.2**, amino acids can only withstand a limited amount of electron irradiation before bond breakage occurs. Amino acids are estimated to withstand electron doses ranging from $1.6\,e^-/Å^2$ for aliphatic and $160\,e^-/Å^2$ for aromatic amino acids.[27] Several studies have been performed on mutations of GFP, which demonstrated that a variable position, an aromatic amino acid, and glycine

are required for successful chromophore formation (see **Figure 2.9**).[124,149,150] Mutation of Gly67 results in disruption of chromophore formation.[151] Since glycine seems to be crucial for the fluorescence of GFP, the electron dose is limited by the electron dose threshold of glycine.

3 Material and Methods

3.1 Material

Table 1: Table of Chemicals

Chemical	**Manufacturer**
Acetone for HPLC (min. 99.8 %)	Chemsolute®, Th. Geyer GmbH + Co. KG, Renningen, Germany
Albumin Fraction V, biotin-free, $\geq$ 98 %, for molecular biology	Carl Roth GmbH + Co KG, Karlsruhe, Germany
Anti-human epidermal growth factor receptor (HER)2 Affibody® Molecule biotin conjugated 20 µM	Affibody, Solna, Sweden
Boric Acid	Sigma-Aldrich, Merck, Darmstadt, Germany
BS^3 (bis(sulfosuccinimidyl)suberate), No-Weigh™ Format	ThermoFisher scientific, Waltham, MA, USA
Cacodylic acid sodium salt trihydrate $\geq$ 98 %	Carl Roth GmbH + Co KG, Karlsruhe, Germany
CellLight™ Actin-GFP, BacMam 2.0	ThermoFisher Scientific, Waltham, MA, USA
Corning® CellStripper™non-enzymatic cell dissociation solution	Corning®, NY, USA
D(+)-Saccharose min. 99.7 %, powdered	Carl Roth GmbH + Co KG, Karlsruhe, Germany
Dulbecco's phosphate buffered saline (DPBS)	Carl Roth GmbH + Co KG, Karlsruhe, Germany
Ethanol absolute for HPLC (min. 99.9 %)	Chemsolute®,Th. Geyer GmbH + Co. KG, Renningen, Germany

EZ-Link™Sulfo-*N*-Hydroxysuccinimide (NHS)-LC-LC-Biotin, No-Weigh™Format	ThermoFisher Scientific, Waltham, MA, USA
Green Fluorescent Protein (GFP) (AA 2-238) protein (His tag)	Antikörper-online GmbH, Aachen, Germany
Glutaraldehyde (GA)	Carl Roth GmbH + Co KG, Karlsruhe, Germany
Gibco® Dulbecco's modified eagle medium (DMEM), high glucose, GlutaMAX™ Supplement, pyruvate	Gibco®, FisherScientific, Hampton, NH, USA
Gibco® fetal calf serum (FCS)	Gibco®, FisherScientific, Hampton, NH, USA
Gibco® Goat Serum, New Zealand origin	Gibco®, FisherScientific, Hampton, NH, USA
Gibco® phosphate buffered saline (PBS), pH 7.4	Gibco®, FisherScientific, Hampton, NH, USA
glycine (Gly) $\geq$ 98.5 % Ph.Eur., USP, BP	Carl Roth GmbH + Co KG, Karlsruhe, Germany
4 Pack Suspended Monolayer Graphene on QF R2/4	Graphenea, San Sebastián, Spain; purchased from Plano GmbH, Wetzlar, Germany
H_2O ROTISOLV® HPLC gradient grade	Carl Roth GmbH + Co KG, Karlsruhe, Germany
MEM non-essential aminoacids (NEAA)s 100x W/O L-Glutamine	Biowest, Nuaillé, France
Paraformaldehyde (PFA)	Electron Microscopy Sciences, Hatfield, PA, USA
Poly-L-Lysine (poly-l-lysine (PLL)) 0.01 % solution	Sigma-Aldrich, Merck, Darmstadt, Germany
Qdot™655 Streptavidin Conjugate 1 µM	Invitrogen™, ThermoFisher Scientific, Waltham, MA, USA

sodium azide (NaN_3) ReagentPlus®, $\geq$ 99.5 %	Sigma-Aldrich, Merck, Darmstadt, Germany
Sodium tetraborate decahydrate, ACS reagent, $\geq$ 99.5 %	Sigma-Aldrich, Merck, Darmstadt, Germany
Sodium cacodylate trihydrate $\geq$ 98 %	Sigma-Aldrich, Merck, Darmstadt, Germany
Superfibronectin from human plasma solution, sterile-filtered, BioReagent, suitable for cell culture	Sigma-Aldrich, Merck, Darmstadt, Germany
Trivial Transfer Graphene™ 3-5 layers, 1 cm x 1 cm	ACS material®, Pasadena, CA, USA

Table 2: Table of Expendable Materials

Component	**Manufacturer**
Cell Culture Flasks, PS, treated, sterile, Filter screw cap 50 mL, 250 mL	Labsolute®, Th. Geyer GmbH + Co. KG, Renningen, Germany
Cell Culture Multiwell plates, treated, 24-well, 96-well	Labsolute®, Th. Geyer GmbH + Co. KG, Renningen, Germany
CELLSTAR® Cell Culture Flasks TC-treated, 250 mL	Greiner Bio-One, Kremsmünster, Austria
CELLSTAR® Cell Culture Multiwell Plates 12-, 48-, 96-well	Greiner Bio-One, Kremsmünster, Austria
CELLSTAR® Centrifuge Tubes 15 mL sterile	Greiner Bio-One, Kremsmünster, Austria
CELLview™ , PS, 35/10 mm, glass bottom, 1 and 4 compartments	Greiner Bio-One, Kremsmünster, Austria
Centrifuge Tubes 50 mL sterile	Labsolute®, Th. Geyer GmbH + Co. KG, Renningen, Germany
micro-Insert 4 Well in µ-Dish 35 mm, high	ibidi GmbH, Gräfelfing, Germany

Ocean Microchips SiN window 400x150 µm, 200 nm spacer	DENSsolutions, Delft, The Netherlands
Omnifix® Single-use syringe Luer Lock Solo (1 mL, 2 mL, 10 mL, 20 mL, 50 mL)	B. Braun Melsungen AG, Melsungen, Germany
Pipette tips with aerosol barrier in racks, sterile and non-sterile	Labsolute®, Th. Geyer GmbH + Co. KG, Renningen, Germany
reaction tubes (0.2 mL, 0.5 mL, 1.5 mL, 2 mL	Labsolute®, Th. Geyer GmbH + Co. KG, Renningen, Germany
Serological ROTILABO® pipettes, sterile (1 mL, 2 mL, 10 mL)	Th. Geyer GmbH + Co. KG, Renningen, Germany
Serological pipettes, sterile, (1 mL, 2 mL, 10 mL)	Carl Roth GmbH + Co KG, Karlsruhe, Germany
Serological pipettes, sterile, (5 mL, 25 mL, 50 mL)	Labsolute®, Th. Geyer GmbH + Co. KG, Renningen, Germany
syringe filters Rotilabo® PES, sterile 0.22 µm	Carl Roth GmbH + Co KG, Karlsruhe, Germany

Table 3: Table of Hardware

Component	**Manufacturer**
AL54 analytical balance	Mettler-Toledo GmbH, Giessen, Germany
atomic resolution analytical microscope JEM-ARM200F	JEOL (Germany) GmbH, Freising, Germany
Centrifuge 5418	Eppendorf, Wesseling-Berzdorf, Germany
DENS solution ocean liquid holder	DENS solutions, Delft, The Netherlands
Easypet®	Eppendorf, Wesseling-Berzdorf, Germany

FEI Quanta FEG250 ESEM	FEI Germany GmbH, Dreieich, Germany
Fluorescence Microscope Leica DMI6000 with Leica DFC365 FX CCD camera, 12-bit	Leica Microsystems GmbH, Wetzlar, Germany
Galaxy® 48R CO_2 Incubator	New Brunswick, Eppendorf, Hamburg, Germany
Gatan Model 950 Solarus™ Plasma Cleaner	Gatan GmbH, München, Germany
Inverted Laboratory Microscope Leica DM IL LED	Leica Microsystems GmbH, Wetzlar, Germany
MSc-Advantage™ Class II Biological Safety Cabinet	ThermoFisher Scientific, Waltham, MA, USA
Perfekt-Kescher® with handle	Plano GmbH, Wetzlar, Germany
Pipettes	Eppendorf, Wesseling-Berzdorf, Germany
Routine stereo Microscope Leica M60	Leica Microsystems GmbH, Wetzlar, Germany
Shaking water bath SW22	Julabo GmbH, Seelbach, Germany

3.2 Preparation of Working Solutions

Table 4: Preparation of Working Solutions

Solution	**Concentration**	**Components**
growth medium		DMEM supplemented with 10 % FCS + 1 % NEAAs
borate buffer (BB) stock solution	0.2 M	Dilute sodium tetraborate (MW = 381.37) in HPLC-grade H_2O to 0.2 M
BB working solution	40 mM	dilute 0.2 M stock solution 1:5 in HPLC-grade H_2O

cacodylate buffer (CB)	1 M	For 1 L stock solution (1 M) dissolve 214 g sodium cacodylate trihydrate (MW = 214) in HPLC-grade H_2O. Adjust pH to 7.4 with concentrated HCl. Fill up to 1 L and store at 4 °C.
CB working solution	0.1 M	Dilute to a 0.1 M working solution and add sucrose stock solution (2 M) to 0.1 M
PBS/Bovine serum albumin (BSA)	1 %	dissolve 1 % BSA in PBS
Gly-PBS	1 M	Dilute glycine (MW = 75.07) in PBS to a 1 M solution
Gly-PBS/BSA	1 %	dissolve 1 % BSA in PBS/Gly to a 1 M solution
Gly-PBS/BSA/goat serum (GS)	1 %	1 % GS in Gly-PBS/BSA
anti-HER2 Affibody	200 nM	dilute stock solution (20 µM) 1:100 in Gly-PBS/BSA/GS
superfibronectin (SFN)	5 µg/mL	dilute SFN stock solution (2 mg/mL of protein) in PBS
QD655	20 nM	centrifuge Qdot™655 Streptavidin Conjugate stock solution 1 µM for 4 min at 8000g, take supernatant and dilute 1:3 in 40 mM BB and fill up with PBS/BSA to the desired volume
PFA	3%	dilute PFA stock solution (16%) to a 3% working solution in CB
PFA/GA	3 % + 0.2 %	dilute PFA stock solution (16 %) to a 3 % working solution in CB and add 0.2 % GA (stock solution: 25 %)
GA	2 %	dilute GA stock solution (25 %) to a 2 % working solution in CB

3.3 Methods

3.3.1 Cleaning of Microchips

Si microchips with an electron-transparent SiN membrane were washed in 100 % acetone for 2 min and transferred to a beaker containing 100 % ethanol for another 2 min. The microchips were then washed in high performance liquid chromatography (HPLC)-grade H_2O for 10 min and dipped in 100 % ethanol afterwards. For drying, microchips were placed on a clean room tissue. The dried microchips were placed on a clean microscope slide and plasma cleaned with 11.5 sccm O_2 and 35 sccm Ar at 9.3 Pa and radio frequency-target of 50 W for 5 min.

3.3.2 Labeling of Microchips with Green Fluorescent Protein

To ensure that for each exposure the same GFP proteins were exposed in EM, the proteins were immobilized on the SiN surface. Two methods were used:

1. Biotin-Streptavidin binding
2. BS^3 crosslinker binding

Microchips were cleaned as mentioned in **Section 3.3.1**, coated with 0.01 % PLL for 5 min at room temperature (RT) and rinsed in HPLC-grade H_2O twice. For TEM experiments, microchips with 200 nm spacers were used and microchips without spacers were used for ESEM experiments.
In the first method, microchips were incubated in 250 µg/mL streptavidin for at least 1 h. After washing with PBS three times, microchips were incubated with 100 µM EZ-link™ Sulfo-NHS-LC-LC-Biotin for 30 min. Microchips were washed in PBS three times and incubated in 125 µg/mL GFP for 30 min. Afterwards, microchips were washed in PBS three times and stored in PBS for fluorescence microscopy. **Figure 3.1a** shows a scheme of the GFP-binding via biotin-streptavidin. Streptavidin, which is attached to the PLL-coated surface, has four binding sites for biotin. Biotin binds to streptavidin and the Sulfo-NHS-side of the complex can bind the free NH_2-groups of the amino acids in GFP.
In the second GFP binding method, bis(sulfosuccinimidyl)suberate (BS^3) was used as NH_2 crosslinker. A scheme of the binding process is shown in **Figure 3.1b**. BS^3

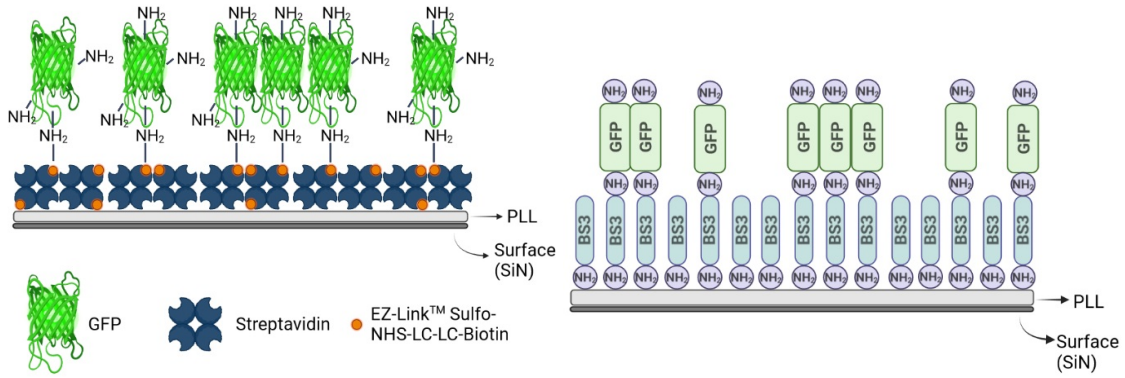

Figure 3.1: Schematics of green fluorescent protein (GFP) binding methods. a) Streptavidin is attached to a poly-l-lysine (PLL)-coated surface of a silicon nitrite (SiN) microchip. Biotin binds to streptavidin and the Sulfo-*N*-Hydroxysuccinimide (NHS)-side of the complex binds the free NH_2-groups of the amino acids in GFP. b) Bis(sulfosuccinimidyl)suberate (BS^3) covalently binds NH_2 groups of PLL immobilized on the SiN surface. The free end of BS^3 binds the NH_2 groups of GFP. Schemes created with BioRender.com.

binds the NH_2 groups of PLL and GFP. PLL-coated microchips were incubated with 2 mM BS^3 for 30 min. After washing once in PBS, the microchips were incubated with 125 µg/mL GFP for 30 min. Microchips were then quenched in 25 mM Gly-PBS solution for 5 min. Microchips were washed in PBS three times and stored in PBS for fluorescence microscopy.

3.3.3 Labeling of SKBR3 Cells with Green Fluorescent Protein

Microchips with 5 µm spacers were cleaned as mentioned in **Section 3.3.1**. Microchips were incubated with 0.01 % PLL solution for 5 min at RT and washed with HPLC-grade H_2O twice. The coated microchips were transferred into a well plate and covered with DMEM growth medium. SKBR3 cells grown in cell culture flask were incubated with CellStripper™ until they detached ($\sim$ 30 min). Cell were counted using a hemocytometer and the concentration was calculated:

$$\text{cell concentration} = \frac{\text{total number of cell in counted quadrants}}{\text{number of counted quadrants}} \cdot 10^4 \qquad (6)$$

$2.5{\cdot}10^5$ cells/ml were added to the PLL-coated microchips and incubated at 37 °C and 5% CO_2 for 2 h to allow cells to settle and to attach to the microchips. According to the manufacturer, 4 µL of CellLight^{TM} actin-GFP were then added per 10^4 cells. SKBR3 cells on microchips were incubated at 37 °C and 5% CO_2 for 48 h and fixed afterwards. For fixation, actin-GFP labeled SKBR3 cells were first washed in PBS three times, then washed in CB once and fixed in 4 % PFA for 15 min. Next, cells were again washed in CB once and in PBS three times. The fixed cells on microchips were stored in PBS with 0.02 % NaN_3 at 4°C until used for EM.

3.3.4 Assembly of Silicon Nitrite Liquid Cells

Samples were prepared as described in **Sections 3.3.2** and **3.3.3**. The DENS solution ocean liquid holder was used for assembly of the liquid cells. The microchips with the sample were used as bottom chips and plain microchips without spacers were used as top chips. The tubing of the specimen holder was filled with HPLC-grade H_2O to wash the tubing system. PBS was sonicated for at least 5 min to degas. The tubing was then filled with sonicated PBS. The two ends of the tubing were connected to provide a sealed environment. Air bubbles in the tip of the liquid holder were removed manually using tweezers. **Figure 3.2** shows the assembly of a liquid cell in the liquid holder. The bottom chip was removed from the well plate and placed into the tip of the liquid holder (**Figure 3.2b**). The top chip was cleaned as mentioned in **Section 3.3.1**, flipped and placed onto the bottom chip so that the SiN windows overlapped (**Figure 3.2c**). The lid of the holder was placed on top and tightened with two screws (**Figure 3.2d**). The outside of the microchips was washed with H_2O five times to remove the excess PBS and prevent formation of salt crystals. To remove excess water on the outside, the liquid holder was placed in vacuum (9.3 Pa for 30 s). The liquid cell remained assembled throughout the experiment. For each pair of microchips, two exposed region of interests (ROIs) at the edges of the SiN window and one unexposed region in the center of the SiN window were analyzed.

To insert the DENS holder into the fluorescence microscope, a custom-made adapter was mounted to maintain the correct working distance for imaging. (**Figure 3.2e-g**).

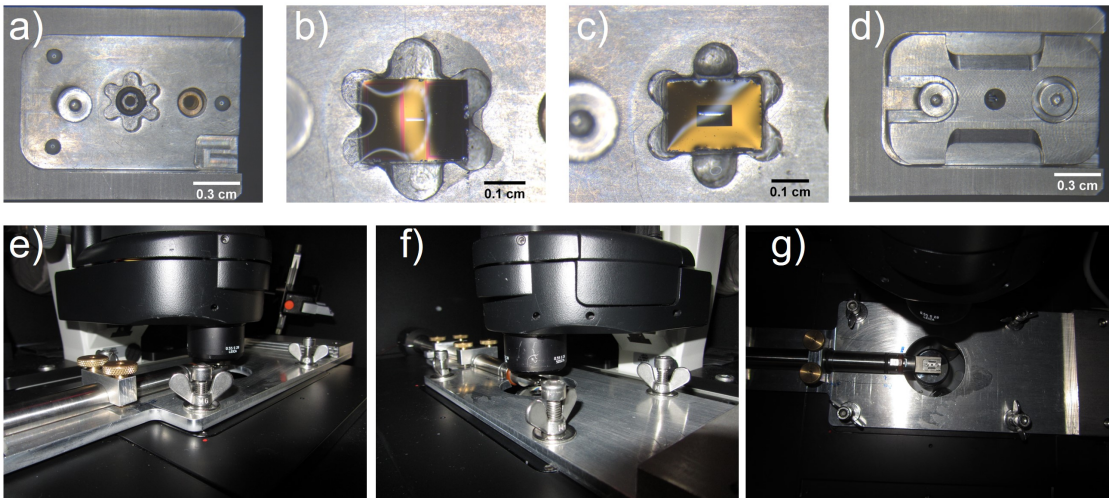

Figure 3.2: Assembly of a silicon nitrite (SiN) liquid cell. a) The tip of a DENS solutions ocean liquid holder was washed with H_2O and then filled with sonicated phosphate buffered saline (PBS). b) A microchip with 200 nm spacers and coated with green fluorescent protein (GFP) was inserted into the tip. c) The top chip without spacers was placed on the bottom chip so that the SiN windows overlap. d) The liquid cell was closed with a lid. e) - g) The liquid holder was placed in the fluorescence microscope on a custom-made adapter to maintain the correct working distance to the objective.

3.3.5 Preparation of Graphene Liquid Cells

Figure 3.3 shows the assembly of a GLC. Two graphene-coated TEM grids as shown in **Figure 3.3a** were plasma cleaned with 39 sccm O_2 at 9.3 Pa and radio frequency-target of 5 W for 15 s. The inset depicts a closer view of the graphene grid. Graphene pockets in the holes of the grid are visible. The tip of a standard TEM holder was used for sample preparation (**e**). One graphene grid was placed in the tip with the graphene side facing up (**f**). 0.5 µL of 1 mg/mL GFP stock solution were added to the graphene grid in the tip (**g**). The second graphene grid was placed on the first one with the graphene side down so that the graphene grids overlap (**b** and **h**). The GLC was closed (**i**) and the tip was placed in a standard holder and used for further investigations. Differential interference contrast (DIC) and fluorescence images were acquired (**c** and **d**). The two TEM grids were misaligned which results in lower light transmission. The inset in **d** depicts a closer view of the grid. The fluorescence was accumulated around the grid bars and in graphene pockets. The GLC remained assembled throughout the experiment. For each GLC,

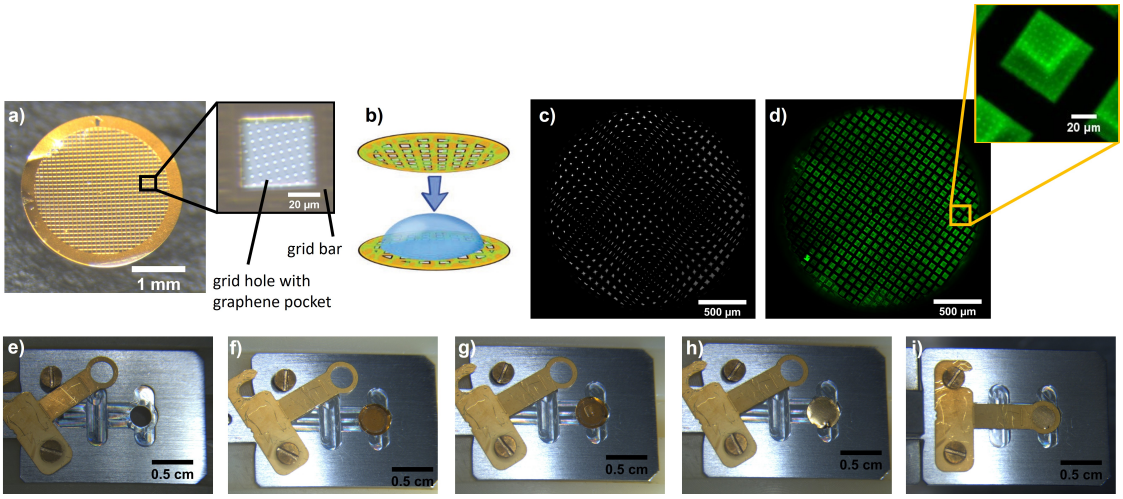

Figure 3.3: Assembly of a graphene liquid cell (GLC). a) Image of a graphene-coated 300 mesh gold grid. The inset depicts a closer view of the grid with grid bars and grid holes with graphene pockets. b) Preparation of a GLC with a grid sandwich. A drop of solution is dispensed on a graphene-coated grid and the GLC is sealed with another graphene-coated grid. Adapted from.[46] c) Differential Interference Contrast (DIC) image of an assembled GLC. Graphene grids overlap, but are misaligned. d) Fluorescence image of an assembled GLC. The inset depicts a closer view of the grid where fluorescence is shown accumulated around the grid bars of the underlying grid and in graphene pockets. e) The tip of a standard specimen holder for transmission electron microscopy (TEM). f) A graphene-coated TEM grid was placed in the tip with the graphene side facing up. g) A droplet of green fluorescent protein (GFP) solution was dispensed on the grid. h) The second graphene-coated TEM grid was placed on the first one with the graphene side facing down to enclose the liquid sample. i) The GLC was fixed in the tip.

two exposed ROIs and one unexposed region were investigated.

3.3.6 Calculation of the Accumulated Dose and Electron Flux

The electron dose in SEM and TEM is given in units of $e^-/Å^2$ and the flux is given in units of $e^-/Å^2s$.

The accumulative electron dose in SEM is given by

$$D_{SEM} = \frac{I \cdot t}{e \cdot d^2} \cdot N \tag{7}$$

where I is the beam current in A, t the pixel dwell time in s, e the elementary charge $e = 1.6 \cdot 10^{-19}$ C, d the pixel size in Å and N the number of images.[152] The

beam current was measured in high vacuum mode in a Faraday cup mounted on the stage. A picoamperemeter was connected to the stage for current readout.
The electron flux in SEM can be calculated by

$$flux_{SEM} = \frac{D}{t \cdot a} \tag{8}$$

where a is the image size of the exposed area in pixels.
In TEM the dose is calculated by

$$D_{TEM} = \frac{counts}{A \cdot f} \tag{9}$$

and the flux is calculated by

$$flux_{TEM} = \frac{D}{T} \tag{10}$$

with A is a defined area in Å^2, f is the conversion factor of the camera in counts per electron (f = 10 counts/electron for gatan imaging filter (GIF) camera at 30 kV and 200 kV) and T the exposure time. A standard sample with gold nanoparticles on carbon was used for dose calculations. The alignment was performed in TEM until atomic resolution was achieved. The counts were acquired in a hole of the carbon layer of the standard sample with defined area A using GIF camera in GIF mode. The dose was calculated according to **Equation 9**. The beam was spread to cover more than the size of the camera so that the entire camera was evenly illuminated. The condenser lens settings were adjusted to achieve the desired electron flux calculated according to **Equation 10**. The accumulated electron dose was calculated by summing the electron dose from each exposure. The critical dose D_c is the electron dose, at which the intensity decreased below $1/e = 0.4$ of its initial value with $e = 2.7$.[24] For the experiments in this thesis, D_c is the dose at which the fluorescence intensity of GFP decreased to 1/e.

3.3.7 Transmission and Environmental Scanning Electron Microscopy

For radiation damage experiments, each sample was irradiated with a constant electron flux and increasing electron dose. All samples were exposed 2 - 4 times at

the same ROIs. In TEM, the liquid holder with the sample was inserted into the electron microscope. After each exposure, the liquid holder was removed from the microscope and brought to the fluorescence microscope for imaging. In ESEM, a GSED and a cooling stage with the temperature set to 4 °C were installed. The specimen was removed from the well plate and placed on the cold stage. The chamber was pumped to a pressure of 1000 Pa. The pressure was then slowly decreased to 700 - 800 Pa until the SiN window was visible. After exposure, the chamber pressure was increased to about 1500 Pa before venting. The sample was placed back in the well plate with PBS and imaged under the fluorescence microscope.

3.3.8 Liquid Thickness Measurements via Electron Energy Loss Spectroscopy

EELS measurements for determining the liquid thickness were performed on GLCs at 200 kV. For EELS with an energy dispersion of 0.25 eV, the collection angle was set to $\beta = 20.8$ mrad and the electron probe convergence semi-angle of 30 - 35 mrad. **Figure 3.4a)** shows STEM of liquid pockets in a GLC with PBS. The circular hole represents overlapping carbon and graphene layers. The area marked in red indicates two overlapping graphene layers. Hence, in the overlapping area, both sides are covered with graphene while the other parts are covered with graphene on one side and carbon on the other. Outside the hole, two carbon layers overlap. Line scans of 2000 pixels and step sizes between 1 and 7 nm were performed, shown as a green line in the spectrum image in **Figure 3.4a**. EEL spectrum (**Figure 3.4b**) and the relative thickness τ/Λ (**Figure 3.4c**) was calculated in DigitalMicrograph software from the spectrum image. τ/Λ is given by[153]

$$\frac{\tau}{\Lambda} = \ln\left(\frac{I_t}{I_0}\right) \tag{11}$$

I_t is the total number of electrons in the spectrum and I_0 is the number of electrons without energy loss (zero-loss peak). The mean free path Λ is calculated from[153]

$$\Lambda = \frac{106 F E_0}{E_M \ln\left(\frac{2\beta E_0}{E_M}\right)} \tag{12}$$

with E_0 the acceleration voltage in eV, β the collection angle, $E_M = 7.6\,(Z_{eff})^{0.36}$ and F the relativistic factor given by[153]

$$F = \frac{1 + \frac{E_0}{1022}}{\left(1 + \frac{E_0}{511}\right)^2} \tag{13}$$

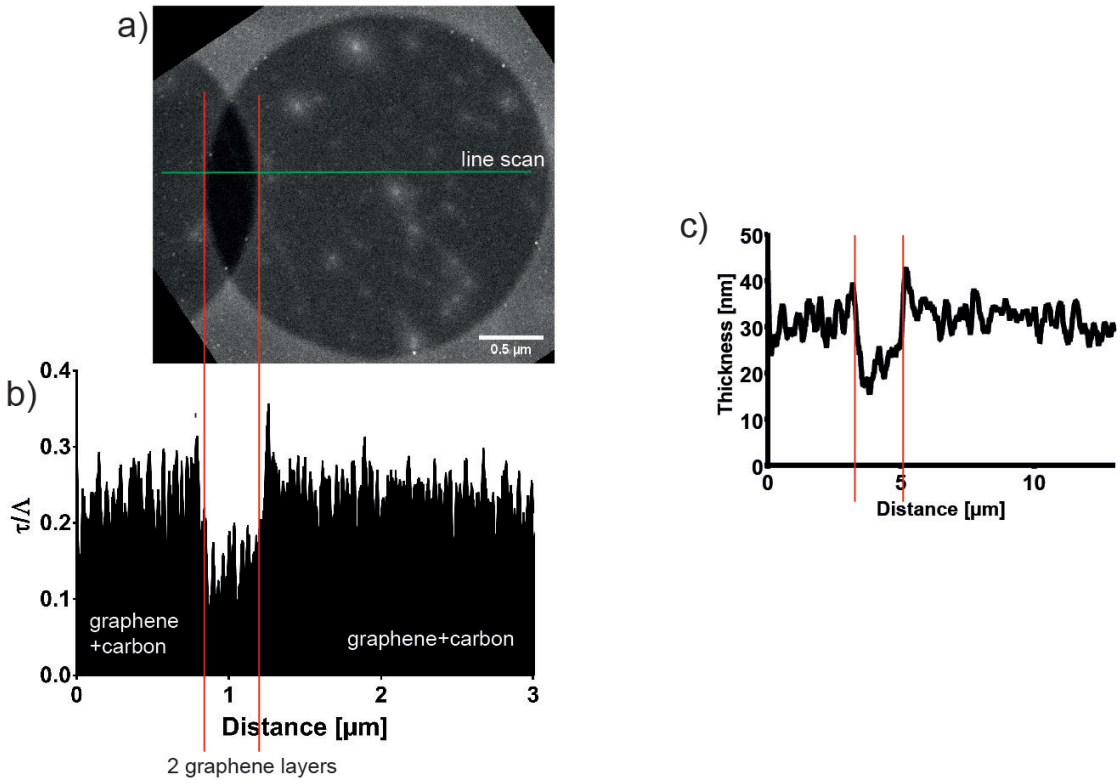

Figure 3.4: Electron energy loss spectroscopy (EELS) of graphene liquid cells (GLCs) in scanning transmission electron microscopy (STEM). a) STEM of a liquid pocket in a GLC. The circular structure represents a liquid pocket with overlapping graphene and carbon layers from the two grids. The marked, darker area represents the overlap of two graphene layers from both grids. b) τ/Λ over the distance of the line scan (2nd order smoothing, 10 neighbors). c) Calculated absolute thickness of the GLC (6th order smoothing, 20 neighbors). The area of two overlapping graphene layers is marked in red.

The effective atomic number Z_{eff} given by

$$Z_{eff} = \frac{\sum f_n Z_n^{1.3}}{\sum f_n Z_n^{0.3}} \tag{14}$$

This way, $\Lambda_{H2O} = 158\,\text{nm}$ was calculated for water for the settings mentioned above and an estimated accuracy of $\pm 20\,\%$.[153] τ can be plotted over the distance of the line scan giving the absolute thickness as exemplary shown in **Figure 3.4d**. The thickness contribution of graphene and carbon was measured via EELS and subtracted from τ.

3.3.9 Fluorescence Microscopy and Data Analysis

Samples were examined for successful binding of GFP in the fluorescence microscope. A DIC image and an image of the fluorescence channel (dichroic filter cube L5) with an excitation wavelength of 460 - 500 nm and an emission wavelength of 512 - 542 nm were acquired.
The liquid cells were introduced to vacuum at 9.3 Pa for 30 s before electron beam exposure to remove excess water from the outside of the microchips. This fluorescence image was used as reference. In ESEM, samples were not exposed to vacuum before electron beam exposure and the images before electron beam exposure were used as reference. After each electron beam exposure, DIC and fluorescence images were acquired from the sample.
According to the size of the ROIs exposed in EM, an area of about the same size was used for intensity analysis in Leica Application Suite X (LAS X) software. The mean grey values (MGVs) of GFP were analyzed relatively after each exposure. MGV_0 are the mean grey values of the reference. The relative fluorescence intensity (RFI) was calculated by:

$$\text{RFI} = \frac{MGV_{ex}}{MGV_0} \tag{15}$$

where MGV_{ex} are the mean grey values of the background on the microchip subtracted from the mean grey values of the sample.
For the fluorescence images presented in **Chapters 4** and **Chapter 5**, contrast and brightness were adjusted for better visualization. Analysis was not affected.

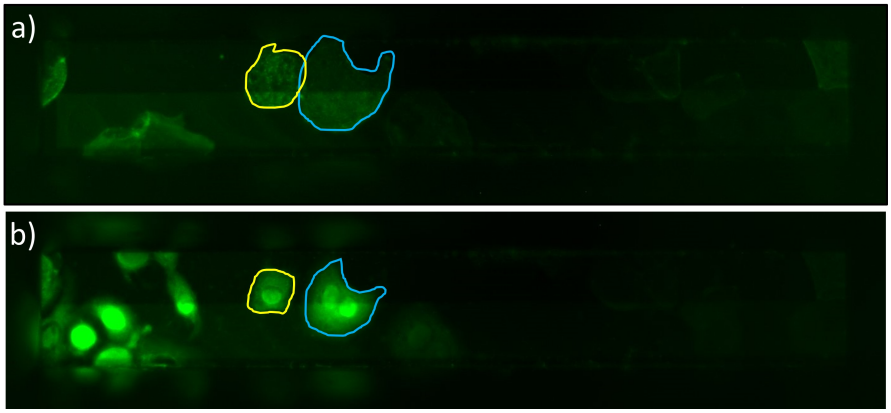

Figure 3.5: Analysis of the area of SKBR3 cells. Fluorescence channel of a silicon nitrite (SiN) liquid cell with SKBR3 cells. Two SKBR3 cells are exemplary marked. The area of the cells is surrounded. a) Prior to electron beam exposure ($0\,e^-/Å^2$) b) After exposure with an electron dose of $1\,e^-/Å^2$.

In SKBR3 cells, the changes in cell area with increasing electron dose were analyzed. For this purpose, cells were marked manually using LAS X software as exemplary illustrated in **Figure 3.5**. Fluorescence images after introduction to vacuum (9.3 Pa for 30 s, $0\,e^-/Å^2$) and after exposure with an electron dose of $1\,e^-/Å^2$ are shown in **Figure 3.5a** and **b**, respectively.
The relative area was calculated by:

$$\text{relative area} = \frac{area_{ex}}{area_0} \tag{16}$$

with $area_ex$ the area of the cells after each exposure and $area_0$ the area of the cells in the reference.

3.3.10 Control Experiments

Control experiments for photobleaching, drying and exposure to imaging conditions were performed. Samples were prepared according to **Sections 3.3.2** and **3.3.3**. To test photobleaching, samples were exposed under fluorescence microscopy. Time-lapses were performed with exposure times of 500 ms and a total time of 30 min. Autofluorescence of SKBR3 cells and the PFA fixative was investigated on SKBR3 cells without GFP labeling. Exposure times of 500 ms were chosen and samples

were imaged over 30 min.
For drying experiments, samples were washed in HPLC-grade water first to prevent formation of salt crystals that could possibly scatter. Samples were imaged during air-drying with an exposure time of 500 - 900 ms for a total of 30 min. Exposures times for all samples were chosen so that fluorescence of GFP could be detected but did not over-saturate.

3.3.11 Labeling of Human Epidermal Growth Factor Receptor 2

Parts of this section were published in Blach, P.; Keskin, S. & de Jonge, N. Graphene Enclosure of Chemically Fixed Mammalian Cells for Liquid-Phase Electron Microscopy Journal of Visualized Experiments, MyJove Corporation, 2020 DOI: 10.3791/61458[154]

Microchips were cleaned as mentioned in **Section 3.3.1**. For coating, a well plate was prepared in which the chips were incubated in 0.01 % PLL solution for 5 min at RT and washed with HPLC-H_2O twice. Subsequently, the microchips were coated with fibronectin-like Protein (FLP) for 5 min at RT and washed with PBS twice. Microchips were then transferred to a 96-well plate and covered with serum-free (SF)-DMEM growth medium. Until cells were ready for seeding, microchips were stored at 37°C and 5 % CO_2. HER2 overexpressing breast cancer cell line SKBR3 was cultured in growth medium at 37 °C and 5 % CO_2. Cells were incubated in CellStripper™ to detach. The cell concentration was determined according to **Equation 6**. Cells were diluted to a concentration of $2.5{\cdot}10^5$ cells/ml using

$$\text{amount needed} = \frac{2.5 \cdot 10^5 \text{cell/mL}}{\text{cell concentration}} \cdot \text{desired volume} \tag{17}$$

100 µL of cell suspension were added into each well of the 96-well plate containing a microchip. The microchips with cells were incubated at 37 °C and 5 % CO_2 until cells attached to the microchips (about 5 min). The density of the cells was investigated with an inverted microscope. **Figure 3.6** shows different scenarios for cell seeding. **A** shows SKBR3 cells on a microchips 5 min after seeding. **B** shows the same cells after 24 h of incubation. Cells flatten and have a good confluency. **C** and **D** show images of a microchip with too many cells seeded after 5 min and

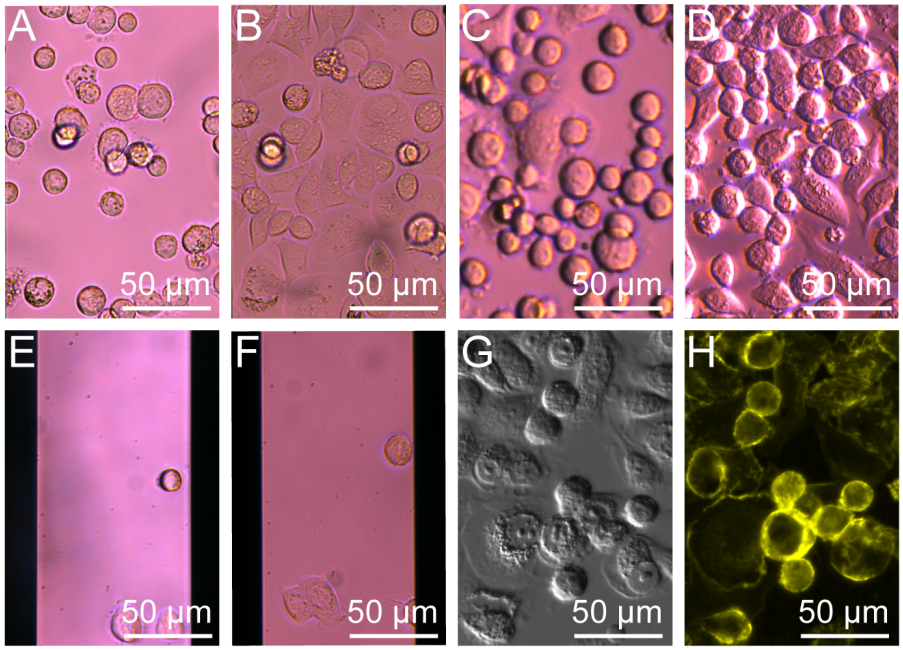

Figure 3.6: Cell seeding on a silicon nitrite (SiN) window of a silicon microchip and human epidermal growth factor receptor (HER) 2 labeled. (**A**) Exemplary image of a SiN window region with SKBR3 cells 5 min after seeding on the microchip. (**B**) The same cells spread on the same SiN window after 24 h. (**C**) SKBR3 cells on a Si microchip 5 min after seeding. (**D**) Same cells as in (C) after 24 h. Cells didn't flatten properly as there were too many cells on the chips upon seeding. (**E**) Cells on a microchip 5 min after seeding. (**F**) Only few cells were visible on the window because too few cells were seeded on the microchip. (**G**) Differential interference contrast (DIC) image of the same SKBR3 cells after quantum dot (QD) labeling of HER2. (**H**) Overlay image of DIC and corresponding fluorescence image of labeled SKBR3 cells with HER2-QD655 (false colored in yellow). This is adapted from .[154]

24 h, respectively. Here, cells didn't flatten properly. **E** and **F** show images of a microchip on which too few cells were seeded. The microchips with the attached cells were transferred to another well containing DMEM and incubated at 37 °C and 5 % CO_2. After 24 h the microchips were transferred to SF-DMEM for starvation and incubated at 37 °C and 5 % CO_2 over night.

For fixation, microchips with cells were transferred into the fume hood and washed in PBS once and in CB once for a few seconds. Cells were fixed with 3 % PFA for 5 min at RT. For quenching, cells were incubated with 1 M Gly-PBS for 10 min. The microchips were rinsed in PBS once.

For HER2 labeling, the unspecific binding sides in the cells were blocked by incubating with 1 M Gly-PBS/BSA/GS for 5 min. The cells were incubated with a specific anti-HER2 affibody biotin conjugate (200 nM) for 10 min. The microchips were washed with PBS/BSA three times. Then, they were incubated with 20 nM QD655 for 12 min. Subsequently, the chips were rinsed in PBS/BSA twice and stored in PBS/BSA for fluorescence microscopy.
For fluorescence imaging, the microchips were placed upside down in a petri dish containing 2 mL of PBS/BSA. QD655 were imaged with texas red (TX)2 channel with an excitation wavelength of 540 - 580 nm and an emitting wavelength of 607 - 683 nm. DIC and fluorescence images are shown in **Figure 3.6G** and **H**, respectively. After fluorescence microscopy, cells on microchips were post fixed in the fume hood. The microchips with the cells facing up were rinsed in CB once and fixed with 2 % GA for 10 min. After this, microchips were again washed in CB once and three times in PBS/BSA. Microchips were stored in PBS/BSA with 0.01 % NaN_3 until used for EM.

3.3.12 Graphene Coating

Parts of this section were published in Blach, P.; Keskin, S. & de Jonge, N. Graphene Enclosure of Chemically Fixed Mammalian Cells for Liquid-Phase Electron Microscopy Journal of Visualized Experiments, MyJove Corporation, 2020 DOI: 10.3791/61458[154]

Graphene coating of SKBR3 cells was performed before STEM to maintain a hydrated layer around the cells. The setup for graphene coating is shown in **Figure 3.7**. Samples were prepared as mentioned in **Section 3.3.11**. A microchip with fixed cells and labeled HER2 was washed in HPLC-grade water to remove any residues of salt from the buffer and placed on a filter paper. The cells were visible as dark spots under a stereomicroscope (**Figure 3.7B**). The multilayer graphene on NaCl crystal was cut into a piece that fits the SiN window of the microchip using a razor blade. Graphene was removed from the salt crystal by tilting the crystal about 45° and touching the water (**Figure 3.7A**). The graphene sheet floating on the water surface is marked in red in **Figure 3.7C**. The graphene sheet was

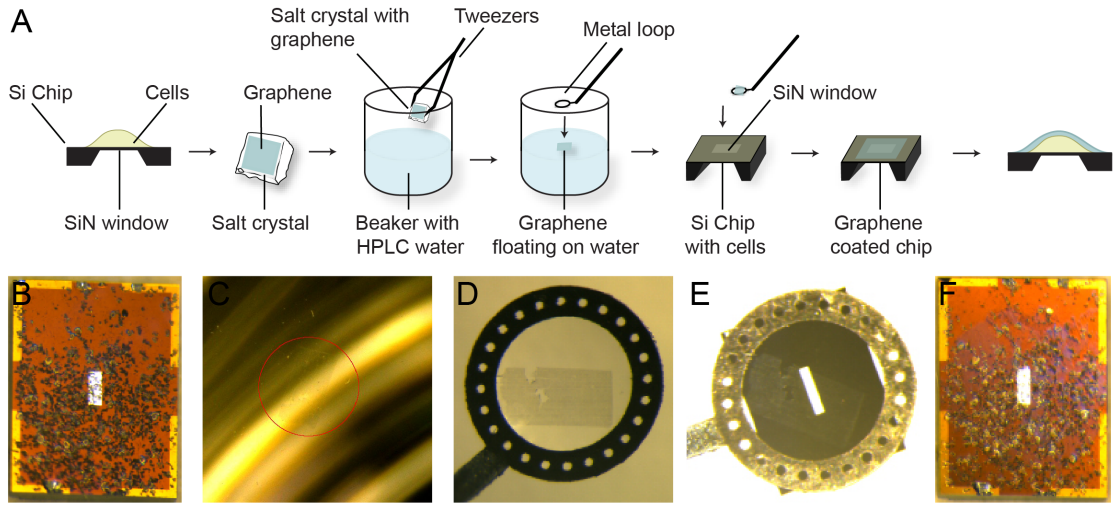

Figure 3.7: Graphene coating of cells seeded on a Si microchip. (**A**) Procedure of graphene coating. Graphene on NaCl crystal is released onto the water surface. The graphene piece is then caught with a metal loop and transferred onto the Si microchip. (**B**) Microchip (2.0 x 2.6 mm) with a silicon nitrite (SiN) window of dimensions 400 x 160 µm without graphene. SKBR3 cells were visible as dark spots. (**C**) Graphene (red circle) floating on the surface of a beaker filled with water. (**D**) Graphene caught with a metal loop. (**E**) The microchip attached to the water droplet so that the graphene was on top of the SiN window. (**F**) Microchip after graphene coating. The graphene was visible as a purple shimmer. This is adapted from .[154]

caught with a metal loop from the surface of the water. The graphene floated within a droplet (**Figure 3.7D**). The microchip was touched with the metal loop and sticked to the metal loop (**Figure 3.7E**). The graphene can be seen on top of the microchip. Under a stereomicroscope, access water was removed using filter paper so that graphene covered all cells on the SiN window. The microchip was removed from the metal loop using tweezers. The graphene was visible as a purple shimmer on the microchip (**Figure 3.7F**). For storage, the microchip was transferred to a compartment petri dish. Another compartments was filled with a HPLC-grade water to provide a water-saturated atmosphere. The petri dish was sealed with parafilm and stored at 4°C.

3.3.13 Scanning Transmission Electron Microscopy and Analysis

Parts of this section were published in Blach, P.; Keskin, S. & de Jonge, N. Graphene Enclosure of Chemically Fixed Mammalian Cells for Liquid-Phase Electron Microscopy Journal of Visualized Experiments, MyJove Corporation, 2020 DOI: 10.3791/61458[154]

STEM analyses were performed at 200 kV. A probe current of $I = 180$ pA (information provided by the manufacturer with 5% accuracy), a beam convergence semi-angle of 13.2 mrad and an ADF detector opening semi-angle range (inner and outer) of 68 - 280 mrad were used. The image size was set to 2048 x 2048 pixels with a pixel dwell time of 6 µs. Microchips with and without graphene coating were placed upside down in a standard specimen holder for TEM and loaded into the electron microscope. An overview of the SiN window with the cells was acquired at a magnification of $M = 800$x. A ROI was identified and QDs were imaged with $M = 80{,}000$x with a pixel size of $d = 1.3$ nm. To visualize the exposed area, an image with lower magnification ($M = 50{,}000$x) was acquired. The electron dose was calculated according to **Equation 7**. 20 Images per series were acquired with $t = 60$ µs each . With the settings above, this resulted in an accumulative electron dose of $D = \frac{1.75 \cdot 10^{-10} \cdot 6 \cdot 10^{-6}}{1.6 \cdot 10^{-19} \cdot (1.3 \cdot 10^{-9})^2} \cdot 20 = (7.8 \pm 0.4) \cdot 10^3\,\mathrm{e^-/Å^2}$.
Diffraction patterns were acquired in TEM to confirm the presence or absence of graphene. Diffraction patterns were acquired with $M = 1200$x, $t = 0.5$ µs, 2048 x 2048 x 3 pixels and a selected area aperture of 50 µm.
An automated software was used to detect the position of QDs in the micrographs. This included the application of a gaussian filter to reduce pixel noice followed by a fast fourier transform bandpass filter to obtain QDs. A threshold was set to binarize the image. A particle diameter of 10 nm with a tolerance of 2 was used for particle detection. Once the positions were detected, the center-to-center distance between 10 pairs of QDs were measured per series. The relative change in QD position was calculated by comparing to the first image:

$$\text{Relative change} = \frac{\text{Distance in Image}}{\text{Distance in first image}} \tag{18}$$

4 Electron Beam Damage of Green Fluorescent Protein in Liquid-Phase Electron Microscopy

In this chapter, electron beam damage of proteins in liquid was investigated using GFP as a model protein. The following research questions were addressed:

- What is the influence of electron dose and electron flux on electron beam damage of GFP?
- What is the difference between the electron beam damage in TEM and ESEM?
- Does graphene as sample support mitigate electron beam damage?

Electron beam damage of GFP was examined in ESEM and liquid-phase TEM. The fluorescence of GFP was used as an indicator for damage caused by the electron beam. When fluorescent, GFP was considered intact and fluorescence degradation indicated damage of GFP. Reference images were acquired under fluorescence microscopy prior to electron beam exposure and show the fluorescence intensities of GFP under native conditions. After each electron beam exposure, fluorescence images were acquired and compared to the reference after vacuum exposure. The fluorescence intensity relative to the fluorescence intensity after vacuum exposure was evaluated (relative fluorescence intensity, RFI). Degradation of RFI was shown with increasing electron dose. The critical dose D_c was defined as the electron dose at which RFI decreased to 1/e and GFP was considered damaged.[24] In literature, it has been described that fluorescence and aliphatic amino acids show damage at electron doses of 0.01 and $1\,e^-/Å^2$, respectively.[27] Therefore, electron doses here were chosen in the range of 0.001 - $100\,e^-/Å^2$ to cover the range reported in literature. Electron fluxes were chosen in the same range. In liquid-phase TEM, SiN sample supports were replaced by graphene because graphene has shown higher dose tolerance for proteins.[26] Before radiation experiments, however, the effects of drying, photobleaching, and exposure to ESEM and TEM conditions were studied to distinguish between these effects and electron beam effects.

4.1 Results

4.1.1 Control Experiments

When working with fluorescent proteins, photobleaching can occur and is an important aspect to consider. Photobleaching was investigated to examine the effect of light exposure on the fluorescence of GFP. In addition, GFP was air-dried to investigate the effect of drying on the fluorescence. Biological processes involving GFP usually occur in liquid and fluorescence properties of dry GFP are unknown. Fluorescence degradation upon drying would allow confirmation of the liquid state of GFP during the radiation experiments. Exposure to TEM and ESEM conditions might as well disrupt protein integrity and affect its fluorescence. Thus, GFP was exposed to TEM and ESEM imaging conditions and the fluorescence intensity was investigated. Exposure times for fluorescence microscopy were chosen to ensure that the fluorescence of GFP was detectable but did not lead to over-saturation. Image series of 30 min were acquired for photobleaching and drying controls to cover the time range required for LP-EM experiments. For photobleaching and ESEM control experiments, it is desirable to have a stable fluorescence intensity close to 100%. This would indicate that exposure to light and EM imaging conditions did not cause any damage to GFP. In order to confirm the presence of liquid, it is desirable to show decreasing fluorescence intensity of GFP upon drying.

Photobleaching of GFP on SiN microchips was conducted in PBS and HPLC-grade H_2O using fluorescence microscopy. Image series were acquired with one image per minute over 30 min. The exposure of each image was 500 ms. RFI is plotted over time in **Figure 4.1a**. The black dotted curve and green squares show bleaching of GFP in PBS and in HPLC-grade H_2O, respectively. RFI was 75 % for PBS and 60 % for HPLC-grade H_2O of the initial intensity after the last exposure. Mean grey values of the fluorescence channel are shown in **Figure 4.1b**. Mean grey values for GFP decreased in both, PBS and HPLC-grade H_2O, but the values for GFP in PBS were about three times higher than for GFP in HPLC-grade H_2O. This indicates that radiation experiments should be performed in PBS for optimal fluorescence. Graphene has shown impermeability to liquids and decreased radiation sensitivity for proteins.[26] For this reason, GFP was encapsulated in GLCs. To confirm, that

GLCs were sealed and liquid did not evaporate under vacuum, the GLC was introduced to vacuum (9.3 Pa for 30 s). Photobleaching of GFP was investigated before and after vacuum as shown in **Figure 4.2a**. One image per minute was acquired over 30 min with an exposure time of 600 ms for each image. RFI remained stable at 100 %, so no photobleaching was observed before and after vacuum. Mean grey values for the same GLCs are plotted over time in **Figure 4.2b**. Mean grey values before and after vacuum were similar with 880 ± 30 mean grey values before and 1000 ± 150 mean grey values after vacuum and were stable over time. This implies that vacuum exposure does not contribute to damage of GFP in GLCs.

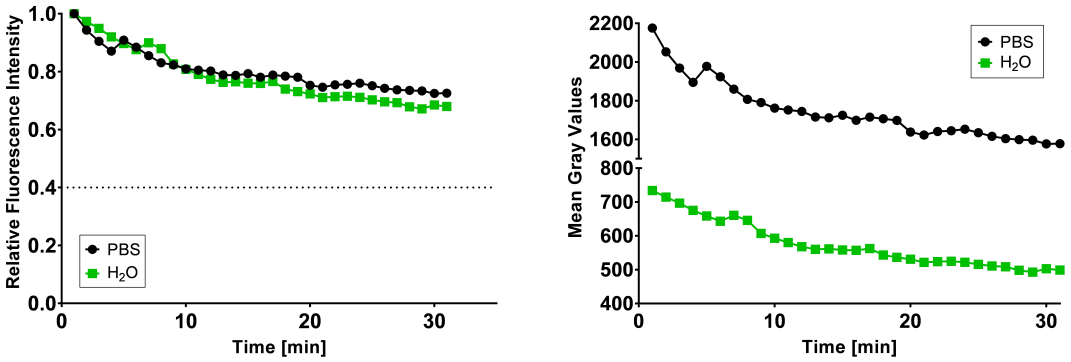

(a) (b)

Figure 4.1: Photobleaching of green fluorescent protein (GFP) on silicon nitrite (SiN) during fluorescence microscopy. a) Relative fluorescence intensity (RFI) and b) Mean grey values over time. GFP on SiN microchips was exposed in PBS (black dots) and H_2O (green squares) in fluorescence microscopy for 30 min with 1 image/min and an exposure time of 500 ms. RFI = 0 and mean grey values = 0 indicate background level. The dotted line indicates 1/e. Data points are connected for better visualization.

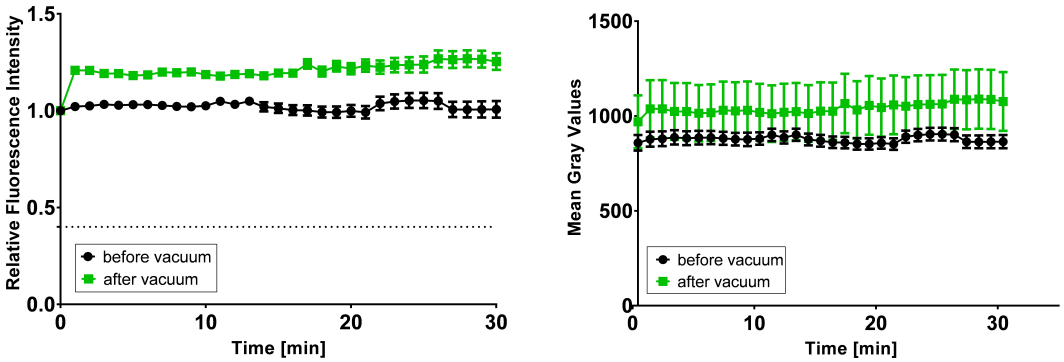

(a) (b)

Figure 4.2: Photobleaching of green fluorescent protein (GFP) in graphene liquid cells (GLCs). a) Relative fluorescence intensity (RFI) and b) Mean grey values over time. Photobleaching of GFP was investigated in a GLC right after GLC preparation (before vacuum, black dots) and after exposure to vacuum (9.3 Pa, after vacuum, green squares). 1 image/min was acquired in the fluorescence microscope with an exposure time of 600 ms. RFI = 0 and mean grey values = 0 indicate background level. The dotted line indicates 1/e. Data points are connected for better visualization.

Next, the effect of drying on the fluorescence of GFP was investigated. **Figure 4.3** shows GFP bound to SiN microchips in PBS (black bar), in dry state (green bar) and after placing dried GFP back into PBS (grey bar). The fluorescence of GFP in PBS was used as reference. After drying, GFP fluorescence decreased to background level (RFI = 0). After rehydration in PBS, the fluorescence did not recover. It can be concluded that GFP fluoresces in liquid and irreversibly degrades in fluorescence after drying. This implies liquid environment conditions and intact proteins if GFP was fluorescent.

The resistance of GFP to the vacuum conditions of ESEM and TEM was investigated. GFP on SiN microchips was placed in ESEM at 750 Pa and 4°C for 5 min for a total of four times. In TEM, a SiN liquid cell was prepared and inserted in TEM at 1.5×10^{-5} Pa for 5 min for a total of five times. **Figure 4.4** shows the RFI over accumulated time in ESEM and TEM. RFI decreased with increasing time in ESEM, but RFI remained above 1/e for 20 min. In TEM, RFI decreased to 85 % after 25 min of exposure to TEM vacuum conditions. This indicates, that for radiation experiments in ESEM, the exposure to ESEM conditions also needs to

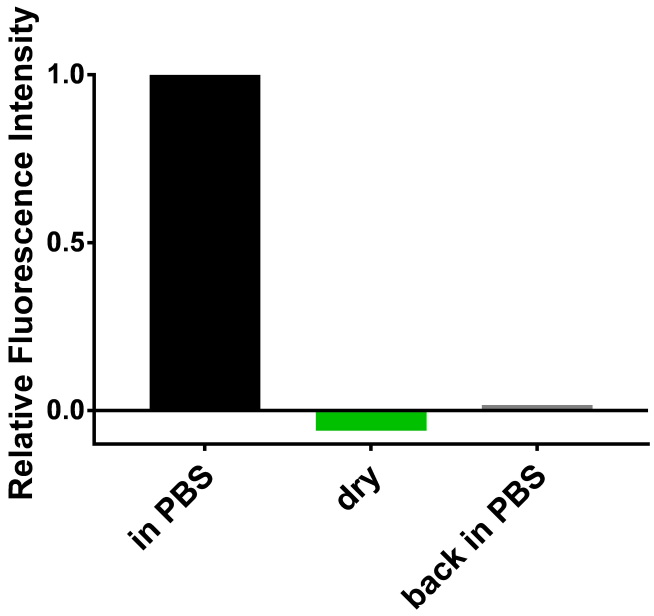

Figure 4.3: Relative fluorescence intensity (RFI) of dry green fluorescent protein (GFP). RFI of GFP on microchips in phosphate buffered saline (PBS) (black bar), air-dried (green bar) and after returning dried GFP into PBS (back in PBS, grey bar) is shown. RFI = 0 indicates background level.

be considered. In TEM, the decrease in RFI caused by the microscope conditions can be neglected.

In conclusion, control experiments implied that photobleaching occurred after some time of light exposure for GFP on SiN microchips, but no photobleaching was observed for GFP in GLCs. Drying resulted in fluorescence degradation, indicating non-reversible damage of GFP upon drying. Therefore, GFP can be considered in liquid when fluorescence can be detected. Exposure to ESEM conditions showed decreasing RFI over time. This implies that exposure to ESEM conditions can cause damage to GFP and needs to be considered in radiation experiments. When exposed to TEM vacuum conditions, no decrease in RFI was observed.

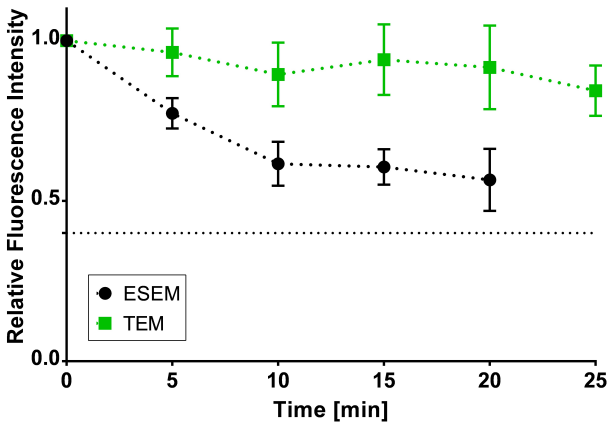

Figure 4.4: Relative fluorescence intensity (RFI) of green fluorescent protein (GFP) in electron microscopy conditions over time. RFI of GFP in environmental scanning electron microscopy (ESEM) conditions at 750 Pa and 4°C (black dots) and transmission electron microscopy (TEM) vacuum conditions at 1.5×10^{-5} Pa (green squares) over time. RFI = 0 indicates background level and the dotted line indicates 1/e. Data points are connected for better visualization.

4.1.2 Electron Beam Exposure of Green Fluorescent Protein in Liquid-Phase Transmission Electron Microscopy

The dose tolerance of GFP was investigated with varying electron dose and electron flux in liquid-phase TEM. Graphene was used as sample support to examine damage mitigation. Fluorescence images were acquired after exposure to vacuum and after each electron beam exposure to measure the decrease in fluorescence intensity. **Figure 4.5** shows exemplary DIC, fluorescence (L5) and combined overlay images of GFP in SiN liquid cells. Exposed ROIs at both ends of the SiN window are marked in red and unexposed regions are marked in yellow. The first row (**a-c**) shows the reference images after exposing the liquid cell to vacuum (9.3 Pa for 30 s). Rows 2 - 5 (**d-o**) show the images after electron beam exposure. The sample was exposed with a constant electron flux of 0.1 $e^-/Å^2s$. The electron dose increased logarithmically from 0.1 $e^-/Å^2$ for the first exposure to 100 $e^-/Å^2$ for the last exposure. After each electron beam exposure, samples were imaged under fluorescence microscopy to investigate the changes in fluorescence intensity. Exposed ROIs as well as unexposed regions showed decreasing fluorescence intensity with increasing

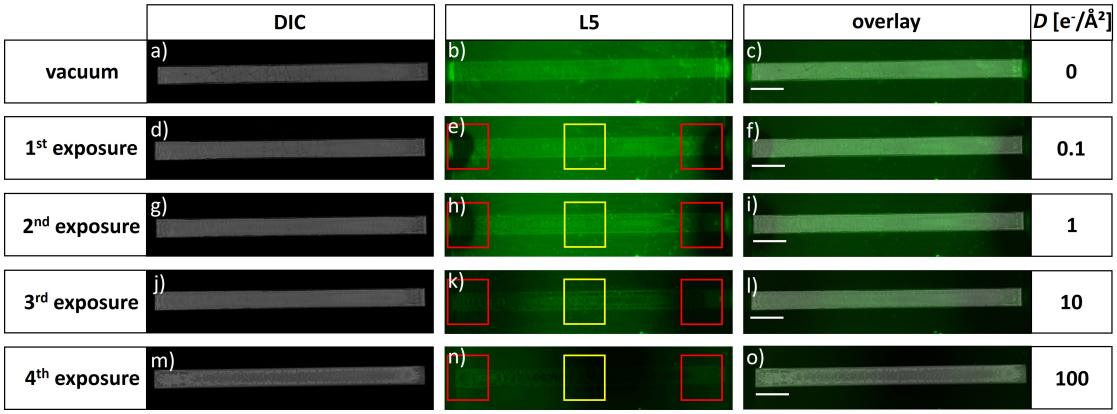

Figure 4.5: Fluorescence images of green fluorescent protein (GFP) in silicon nitrite (SiN) liquid cells after each electron beam exposure in liquid-phase transmission electron microscopy (TEM) at 200 kV. Differential interference contrast (DIC), fluorescence (L5) and combined overlay images of GFP in a SiN liquid cell are shown. GFP was exposed with an electron flux of $0.1\,e^-/Å^2s$. The first row (a-c) shows the reference images after introducing the liquid cell to vacuum (9.3 Pa for 30 s) and prior to electron beam exposure. Rows 2 - 5 show the images after electron beam exposure with an electron dose of $0.1\,e^-/Å^2$ for 1st (d-f), $1\,e^-/Å^2$ for 2nd (g-i), $10\,e^-/Å^2$ for 3rd (j-l) and $100\,e^-/Å^2$ for 4th (m-o) exposure. Red rectangles illustrate the exposed regions of interest (ROIs) at the edges of the SiN window and yellow rectangles mark unexposed regions. Scale bars are 50 µm.

electron dose.

The influence of electron dose and electron flux on the electron beam damage of GFP was examined in liquid-phase TEM. **Figure 4.6** shows the RFI of GFP in SiN liquid cells exposed in TEM at 200 kV over the electron dose. Each sample was exposed with a constant electron flux and varying electron dose. An electron dose of $0\,e^-/Å^2$ represents values after exposure to vacuum (9.3 Pa for 30 s). **Figure 4.6a** shows decreasing RFI with increasing electron dose for all electron fluxes. RFI decreased to 1/e at an electron dose of $0.01\,e^-/Å^2$ for electron fluxes of 0.001 and $0.01\,e^-/Å^2s$. At an accumulative electron dose of $0.1\,e^-/Å^2$, RFI was close to background level (RFI = 0). **Figure 4.6b** shows unexposed regions of the same samples. Although the regions were not exposed, RFI decreased with increasing electron dose ($D_c < 0.1\,e^-/Å^2$ for 0.001 and $0.01\,e^-/Å^2s$). At an electron dose of $0.1\,e^-/Å^2$, RFI decreased below background level for an electron flux of $0.001\,e^-/Å^2s$. For an electron flux of $0.1\,e^-/Å^2s$, $D_c < 100\,e^-/Å^2$. At an electron

dose of $100\,e^-/Å^2$, RFI decreased below background level for all electron fluxes. **Table 5** summarizes the findings for GFP in SiN liquid cells. For electron fluxes of 0.01, 0.1, 1 and $10\,e^-/Å^2s$, RFI was already below 1/e after the first exposure.

Table 5: Critical electron doses of green fluorescent protein in silicon nitrite liquid cells in liquid-phase transmission electron microscopy.

electron flux $[e^-/Å^2s]$	D_c exposed regions $[e^-/Å^2]$	D_c unexposed regions $[e^-/Å^2]$
0.001	< 0.01	< 0.1
0.01	< 0.01	< 0.1
0.1	< 0.1	< 100
1	< 1	< 1
10	< 10	< 10

In conclusion, a critical dose of $D_c < 0.01\,e^-/Å^2$ was observed for GFP in SiN liquid cells exposed in TEM at 200 kV. Different electron fluxes show similar RFI degradation, indicating flux independent damage of GFP. Unexposed regions showed $D_c < 0.1\,e^-/Å^2$. To ensure the investigation of intact proteins, GFP in SiN liquid cells must be exposed with electron doses below $0.01\,e^-/Å^2$.

4.1.3 Liquid Thickness of Graphene Liquid Cells

GFP was encapsulated in GLCs to mitigate electron beam damage. To confirm a liquid layer in GLCs, the liquid thickness was measured via EELS prior to exposure. **Figure 4.7** shows the liquid thickness of different regions of GLCs with GFP in PBS (black), PBS without protein (green) and GFP in HPLC-grade H_2O (grey). The liquid thickness of GFP in PBS was measured in 11 different regions of the GLC. The mean thickness of these regions was 380 ± 110 nm. The mean liquid thickness of 10 regions in a GLC with GFP-free PBS was 40 ± 8 nm. The preparation of a GLC with GFP in HPLC-grade H_2O showed a mean liquid thickness of 230 ± 140 nm measured in 7 regions.

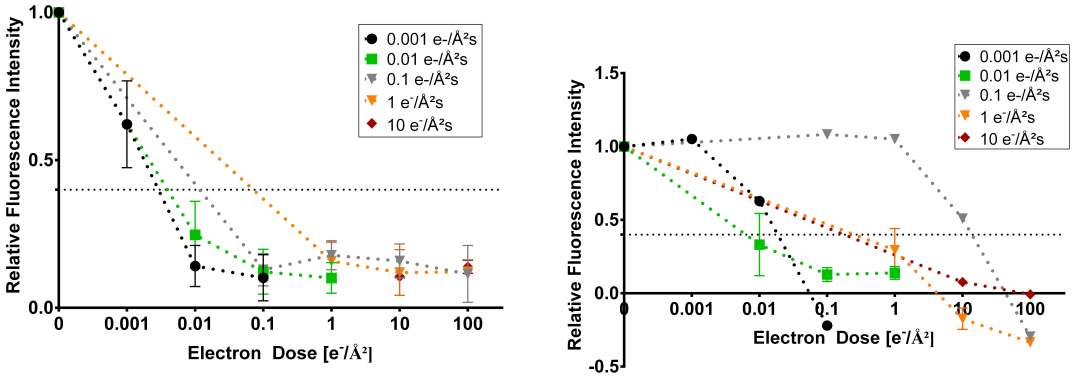

Figure 4.6: Relative fluorescence intensity (RFI) of green fluorescent protein (GFP) in liquid-phase transmission electron microscopy (TEM) at 200 kV. a) Relative fluorescence intensity (RFI) of exposed regions of interest (ROIs) and b) RFI of unexposed regions. GFP was exposed with electron fluxes from 0.001 to 10 $e^-/Å^2s$ and electron doses of 0.001 to 100 $e^-/Å^2$. An electron dose of 0 $e^-/Å^2$ represents values after vacuum. RFI = 0 indicates background level. The dotted lines indicate 1/e. Data points are connected for better visualization.

4.1.4 Electron Beam Exposure of Green Fluorescent Protein in Graphene Liquid Cells in Transmission Electron Microscopy

An overlay of DIC and fluorescence channel of an assembled GLC with encapsulated GFP is shown in **Figure 4.8**. Red rectangles represent exposed ROIs and the yellow rectangle represents the unexposed region. The inset depicts a closer view of the fluorescence channel of an exposed area. Accumulation of fluorescence around grid bars and in graphene liquid pockets is visible.

Figure 4.9 shows DIC, fluorescence (L5) and combined overlay images of a ROI before, after vacuum and after each electron beam exposure. Exposed regions are marked in red in the fluorescence and the overlay images. Before and after vacuum (**Figure 4.9a - f**), the fluorescence signal was accumulated around the bars of the grids and in graphene liquid pockets. After the first electron beam exposure (**Figure 4.9g - i**), dark spots appeared in the exposed regions. In the second and third exposure (**Figure 4.9j - o**), some squares of the GLC showed decreased fluorescence while other squares showed increased fluorescence.

Figure 4.10 shows the RFI of GFP in GLCs in TEM at 200 kV with electron fluxes

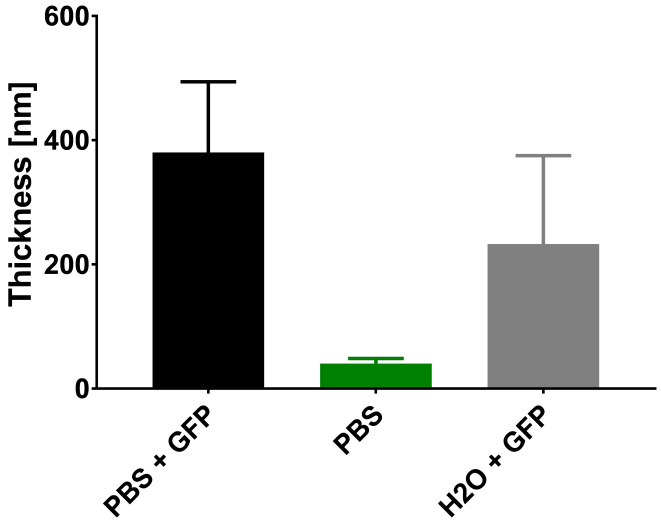

Figure 4.7: Liquid thickness of different regions in graphene liquid cells (GLCs) with phosphate buffered saline (PBS), green fluorescent protein (GFP) and H_2O. The liquid thickness of GLCs was measured using electron energy-loss spectroscopy (EELS). GFP in PBS is shown in black (N = 11), PBS without GFP is shown in green (N = 10) and GFP in H_2O is shown in grey (N = 7).

of 0.001 to 1 $e^-/Å^2s$ and electron doses of 0.001 to 100 $e^-/Å^2$. An electron dose of 0 $e^-/Å^2$ represents the reference after vacuum exposure (9.3 Pa for 30 s). RFI = 0 indicates background level. Each GLC was exposed with a constant electron flux and increasing electron dose. Two exposed ROIs and one unexposed region were analyzed for each GLC. Squares with decreasing RFI were used for analysis. **Figure 4.10a** shows the RFI of exposed ROIs. RFI decreased with increasing electron dose for all electron fluxes. At an electron dose of 1 $e^-/Å^2$, RFI was 70 % for 0.01 and 0.1 $e^-/Å^2s$. $D_c < 10\,e^-/Å^2$ for an electron flux of 1 $e^-/Å^2s$, but for electron fluxes of 0.001, 0.01 and 0.1 $e^-/Å^2s$, RFI remained above 1/e. **Figure 4.10b** shows the RFI over the electron dose for unexposed regions. RFI decreased to 70 % at an electron dose of 1 $e^-/Å^2$ for all electron fluxes. **Table 6** summarizes the critical electron doses for exposed and unexposed regions for GFP in GLCs.
As mentioned in **Section 2.6**, elastic scattering can be reduced at lower beam energy. To determine whether elastic or inelastic scattering was the main cause for radiation damage, GFP was also studied in GLCs in TEM at 30 kV. **Figure 4.11** shows the RFI for electron fluxes of 0.001 to 1 $e^-/Å^2s$ over electron doses of 0.001

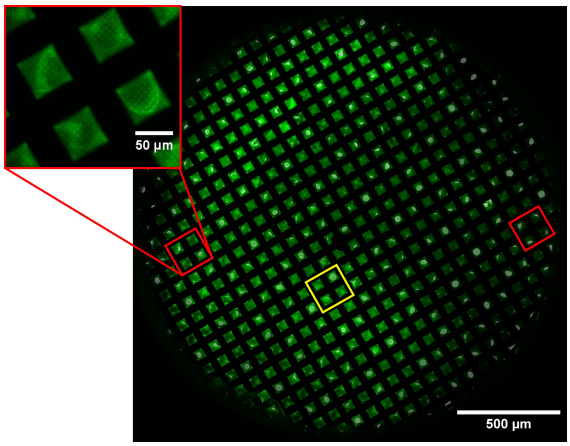

Figure 4.8: Overview of a graphene liquid cell (GLC) with encapsulated green fluorescent protein (GFP) under fluorescence microscopy. Overlay image of differential interference contrast (DIC) and fluorescence channel of an assembled GLC with encapsulated GFP. Red rectangles indicate exposed regions and the yellow rectangle indicates the unexposed region. The inset depicts a closer view of an exposed region.

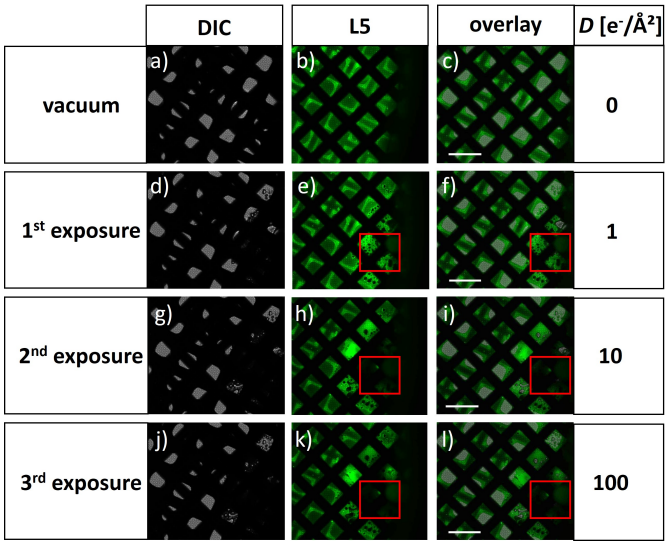

Figure 4.9: Fluorescence images of green fluorescent protein (GFP) encapsulated in a graphene liquid cell (GLC) after each electron beam exposure in liquid-phase transmission electron microscopy (TEM) at 200 kV. Differential interference contrast (DIC), fluorescence (L5) and combined overlay images of GFP in a GLC are shown. The first row (a-c) shows the reference images after introduction of GFP in GLC to vacuum (9.3 Pa for 30 s) and prior to electron beam exposure. Rows 3 - 5 (d-l) show images after electron beam exposure with a constant electron flux of 1 $e^-/Å^2s$ and an electron dose of 1 (1^{st}, d-f), 10 (2^{nd}, g-i) and 100 $e^-/Å^2$ (3^{rd}, j-l). Red rectangles indicate the exposed area. Scale bars are 100 µm.

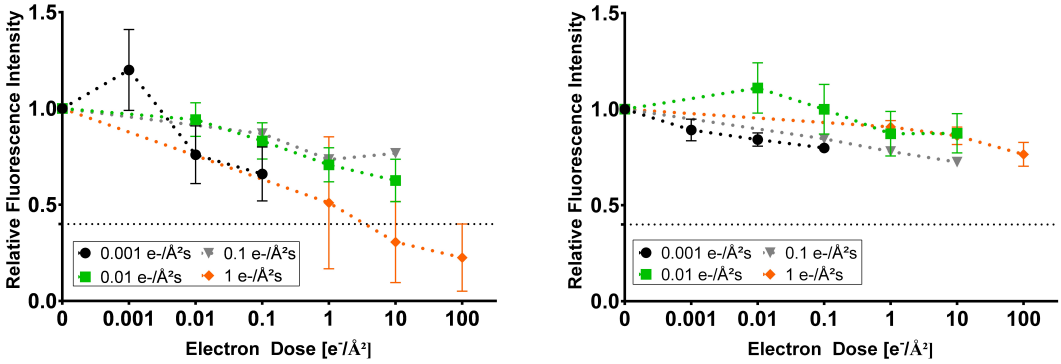

Figure 4.10: Relative fluorescence intensity (RFI) of green fluorescent protein (GFP) in graphene liquid cells (GLCs) exposed in liquid-phase transmission electron microscopy (TEM) at 200 kV. a) RFI of exposed regions of interest (ROIs) and b) RFI of unexposed regions. GFP was exposed with electron fluxes from 0.001 to $1\,e^-/Å^2s$ and accumulative electron doses of 0.001 to $100\,e^-/Å^2$. An electron dose of $0\,e^-/Å^2$ represents reference values after vacuum. RFI = 0 indicates background level. The dotted line indicates 1/e. Data points are connected for better visualization.

Table 6: Critical electron doses of green fluorescent protein in graphene liquid cells in liquid-phase transmission electron microscopy.

electron flux $[e^-/Å^2s]$	D_c exposed regions $[e^-/Å^2]$	D_c unexposed regions $[e^-/Å^2]$
0.001	-	-
0.01	-	-
0.1	-	-
1	< 10	-

to $100\,e^-/Å^2$. An electron dose of $0\,e^-/Å^2$ represents reference values after vacuum (9.3 Pa for 30 s). RFI = 0 indicates background level. **Figure 4.11a** shows decreasing RFI over increasing electron dose for all electron fluxes. $D_c < 1$ and $10\,e^-/Å^2$ was observed for electron fluxes of 0.001 and $1\,e^-/Å^2s$, respectively. For electron fluxes of 0.01 and $0.1\,e^-/Å^2s$, RFI remained above 1/e up to an accumulated electron dose of $10\,e^-/Å^2$. **Figure 4.11b** shows the RFI over the electron dose for unexposed regions. For all fluxes, RFI remained above 1/e up to an accumulated

electron dose of $100\,e^-/Å^2$.

Figure 4.12 shows the comparison of GFP in GLCs exposed in TEM at 30 kV and 200 kV. RFI for electron fluxes of 0.001 to $1\,e^-/Å^2s$ over electron doses of 0.001 to $100\,e^-/Å^2$ are shown. RFI of GFP exposed at 30 kV and 200 kV was similar for most electron doses. The beam energy did not have a major impact on the dose tolerance of GFP.

It can be concluded, that GFP encapsulated in GLCs showed a critical dose of $D_c < 10\,e^-/Å^2$. Changing the beam energy from 200 kV to 30 kV did not have an impact on the electron dose tolerance of GFP in GLCs. This indicates that elastic scattering did not have a major impact on the radiation damage of GFP.

4.1.5 Comparison of the Electron Dose Tolerance of Green Fluorescent Protein in Graphene Liquid Cells and Silicon Nitrite Liquid Cells

Electron beam damage of GFP prepared in SiN liquid cells and in GLCs was compared. **Figure 4.13** shows the RFI of GFP in GLCs and SiN liquid cells over the electron dose. For exposed regions, RFI was higher if GFP was encapsulated in GLCs instead of SiN liquid cells for all electron fluxes (**Figure 4.13a**). RFI for GFP in SiN liquid cells decreased below 1/e at an electron dose of $0.01\,e^-/Å^2$ and was close to background level at an accumulated electron dose of $0.1\,e^-/Å^2$. GFP in GLCs still showed RFI above 1/e at the same electron dose. Unexposed regions in GLCs showed RFI of 70 % up to an accumulative electron dose of $100\,e^-/Å^2$. In SiN liquid cells, RFI of unexposed regions decreased below background level at an electron dose of $0.1\,e^-/Å^2$ for some fluxes (**Figure 4.13b**). The critical electron doses for GFP in SiN liquid cells and in GLCs are summarized in **Table 7**.

In conclusion, the electron dose tolerance of GFP was increased from $0.01\,e^-/Å^2$ to $10\,e^-/Å^2$ when encapsulating GFP in GLCs instead of SiN liquid cells.

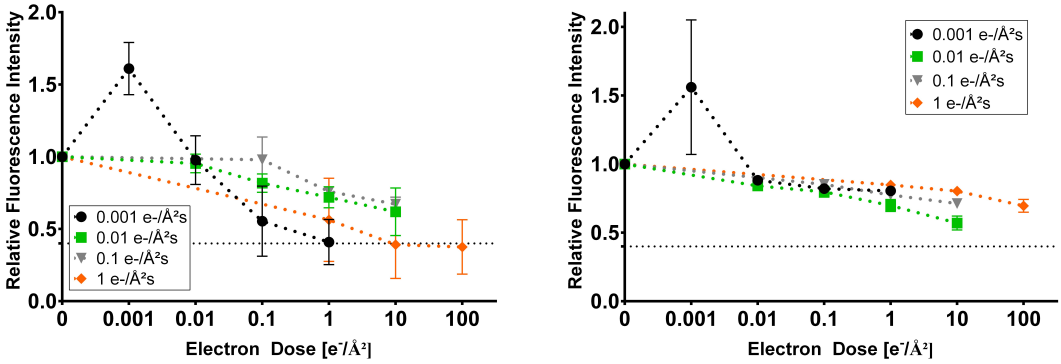

(a) (b)

Figure 4.11: Relative fluorescence intensity (RFI) of green fluorescent protein (GFP) in graphene liquid cells (GLCs) exposed in liquid-phase transmission electron microscopy (TEM) at 30 kV. a) RFI of exposed regions of interest (ROIs) and b) RFI of unexposed regions. GFP was exposed with electron fluxes from 0.001 to $1\,e^-/Å^2s$ and accumulative electron doses of 0.001 to $100\,e^-/Å^2$. An electron dose of $0\,e^-/Å^2$ represents values after vacuum. RFI = 0 indicates background level. The dotted line indicates 1/e. Data points are connected for better visualization.

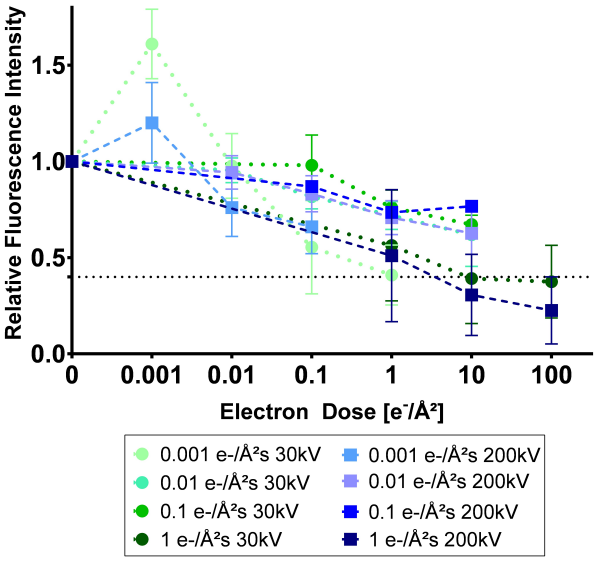

Figure 4.12: Relative fluorescence intensity (RFI) of green fluorescent protein (GFP) in graphene liquid cells (GLCs) exposed in liquid-phase transmission electron microscopy (TEM) at 30 kV and 200 kV. GFP was exposed at electron fluxes from 0.001 to $1\,e^-/Å^2s$ and accumulative electron doses of 0.001 to $100\,e^-/Å^2$ at 30 kV (squares) and 200 kV (dots). An electron dose of $0\,e^-/Å^2$ represents values after vacuum. RFI = 0 indicates background level. The dotted line indicates 1/e. Data points are connected for better visualization.

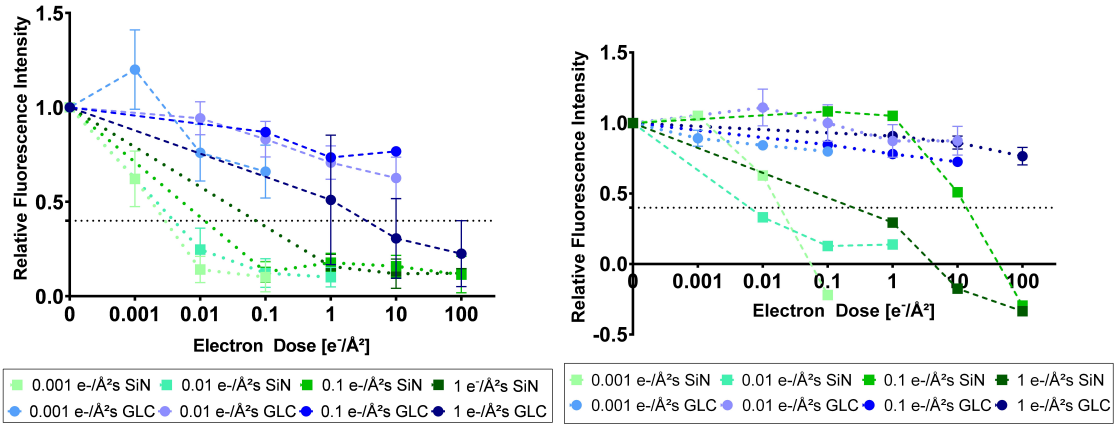

(a) (b)

Figure 4.13: Comparison of the relative fluorescence intensities (RFI) of green fluorescent protein (GFP) in graphene liquid cells (GLCs) and silicon nitrite (SiN) liquid cells exposed in liquid-phase transmission electron microscopy (TEM) at 200 kV. a) RFI of exposed regions of interest (ROIs) and b) RFI of unexposed regions. GFP was exposed at electron fluxes from 0.001 to 1 $e^-/Å^2s$ and accumulative electron doses of 0.001 to 100 $e^-/Å^2$. Dots represent GFP in SiN liquid cells and squares represent GFP in GLCs. An electron dose of 0 $e^-/Å^2$ represents reference values after vacuum. RFI = 0 indicates background level and the dotted line indicates 1/e. Data points are connected for better visualization.

Table 7: Critical electron doses of green fluorescent protein in silicon nitrite and graphene liquid cells in liquid-phase transmission electron microscopy.

electron flux $[e^-/Å^2s]$	D_c exposed regions SiN $[e^-/Å^2]$	D_c unexposed regions SiN $[e^-/Å^2]$	D_c exposed regions GLCs $[e^-/Å^2]$	D_c unexposed regions GLCs $[e^-/Å^2]$
0.001	< 0.01	< 0.1	-	-
0.01	< 0.01	< 0.1	-	-
0.1	< 0.1	< 100	-	-
1	< 1	< 1	< 10	-

4.1.6 Electron Beam Exposure of Green Fluorescent Protein in Environmental Scanning Electron Microscopy

As mentioned in **Section 2.1.2**, ionized gas molecules in ESEM can reduce charging effects by compensating for negative charge generated in the sample. To investigate if this effect can mitigate beam damage, the electron dose tolerance of GFP was studied in ESEM at 30 kV for varying electron fluxes and electron doses. In addition, the difference between a parallel electron beam as used in TEM and a focused electron beam as used in SEM was compared. GFP on SiN microchips was prepared and investigated under fluorescence microscopy before and after each electron beam exposure. **Figure 4.14** shows exemplary fluorescence images of a radiation series in ESEM at 30 kV with a constant electron flux of 0.1 $e^-/Å^2s$. DIC, fluorescence (L5) and the combined overlay channels are shown before and after each exposure. The first row (**Figure 4.14a - c**) shows the reference images before electron beam exposure. Rows 2 - 5 (**Figure 4.14d - o**) show the sample after electron beam exposure. Red rectangles in L5 show the ROIs exposed in ESEM and yellow rectangles show the unexposed region. The electron dose increased logarithmically from 0.1 $e^-/Å^2$ for the first exposure to 100 $e^-/Å^2$ for the last exposure. With increasing electron dose, exposed areas showed reduced fluorescence intensity. However, the fluorescence in unexposed regions decreased as well.

Figure 4.15a shows the RFI of exposed ROIs over the electron dose for electron fluxes ranging from 0.001 to 10 $e^-/Å^2s$. The lowest electron flux of 0.001 $e^-/Å^2s$ showed $D_c < 0.001\ e^-/Å^2$. $D_c < 0.1\ e^-/Å^2$ for electron fluxes of 0.01 and 0.1 $e^-/Å^2s$. For 1 and 10 $e^-/Å^2s$, $D_c < 1\ e^-/Å^2$, which, however, was the smallest possible dose for such high fluxes. No significant difference in the electron dose tolerance was observed for different electron fluxes. **Figure 4.15b** shows the RFI over the electron dose of unexposed regions of the same samples as in a). For electron fluxes of 0.01 to 1 $e^-/Å^2s$, unexposed regions showed higher RFI compared to exposed ROIs for electron dose up to 1 $e^-/Å^2$. From electron doses of 10 $e^-/Å^2$, RFI of unexposed areas was similar to exposed ROIs for electron fluxes of 0.1, 1 and 10 $e^-/Å^2s$. $D_c \approx 0.1\ e^-/Å^2$ for 0.1 $e^-/Å^2s$, $D_c < 1$ for 10 $e^-/Å^2s$ and $D_c < 10\ e^-/Å^2$ for 1 $e^-/Å^2s$. **Table 8** summarizes the findings for GFP on SiN microchips exposed in ESEM.

Next, the impact of the electron dose per pixel on the electron dose tolerance

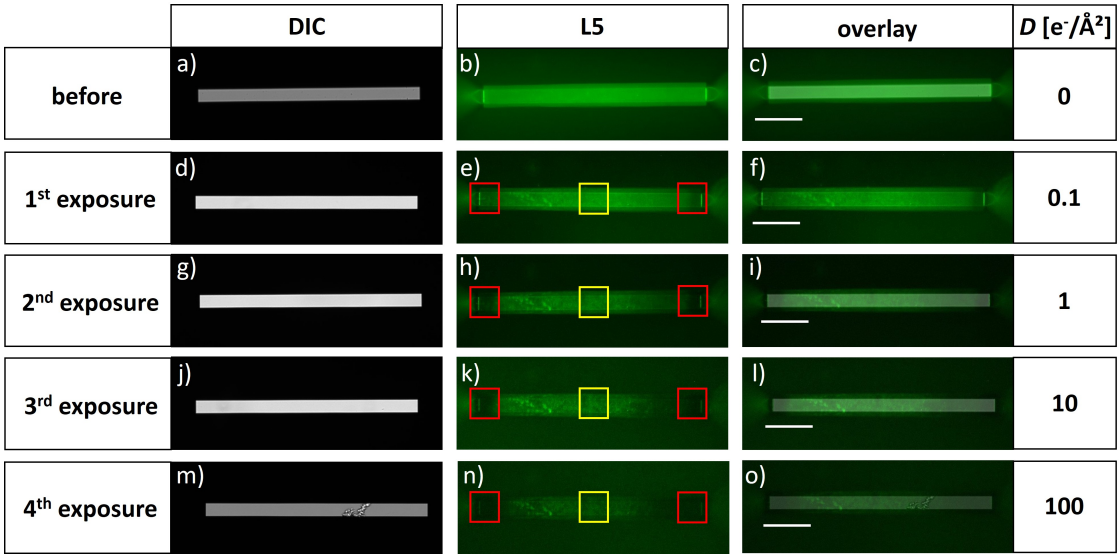

Figure 4.14: Fluorescence images of green fluorescent protein (GFP) after each electron beam exposure in environmental scanning electron microscopy (ESEM) at 30 kV. Images of differential interference contrast (DIC), fluorescence (L5) and the combined overlay for GFP exposure in ESEM are shown. The first row (a-c) shows the images prior to electron beam exposure. Rows 2 - 5 (d-o) show the images after electron beam exposure with a constant electron flux of $0.1\,e^-/Å^2s$ and electron doses of $0.1\,e^-/Å^2$ for 1st (d-f), $1\,e^-/Å^2$ for 2nd (g-i), $10\,e^-/Å^2$ for 3rd (j-l) and $100\,e^-/Å^2$ for 4th (m-o) exposure. Red rectangles show the exposed region of interests (ROIs). Yellow rectangles show the unexposed region. Scale bars are 100 µm.

of GFP was investigated. For the same total electron dose, a focused probe has higher intensity per pixel than a broader electron beam. Therefore, a broader electron beam ('defocused', change in working distance of 2 mm) was compared to the focused electron beam ('focused') that was used for the experiments in **Figure 4.15**. **Figure 4.16** shows the comparison of GFP exposed with focused and defocused electron beam for the three intermediate electron fluxes of 0.01, 0.1, and $1\,e^-/Å^2s$. $D_c < 0.1\,e^-/Å^2$ for electron fluxes of 0.1 and $1\,e^-/Å^2s$ for both, focused and defocused electron beams. For an electron flux of $0.01\,e^-/Å^2s$, $D_c < 1\,e^-/Å^2$ for the focused electron beam and $D_c < 10\,e^-/Å^2$ for the defocused electron beam. No significant effect of the electron dose per pixel on the electron dose tolerance of GFP was observed. The electron dose tolerance of GFP was investigated in LP-EM. RFI was analyzed to study the damage of GFP caused by electron beam exposure. The influence of electron flux and electron dose was investigated. The

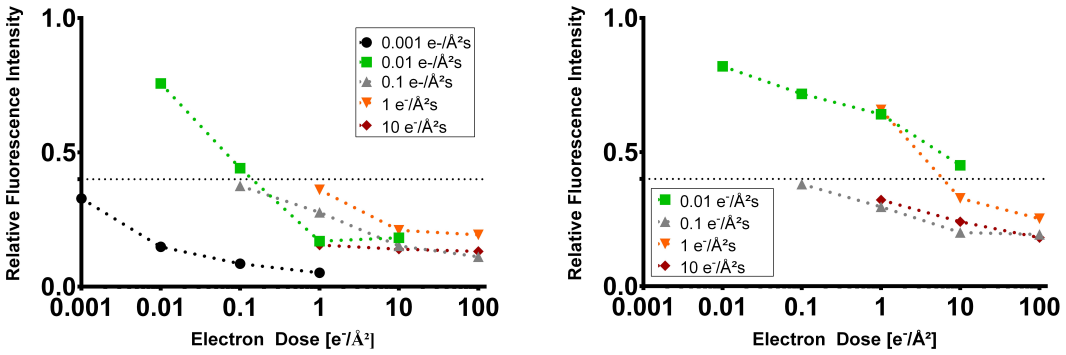

(a) (b)

Figure 4.15: Relative fluorescence intensity (RFI) of green fluorescent protein (GFP) during electron beam exposure in environmental scanning electron microscopy (ESEM) at 30 kV. a) RFI of exposed regions and b) RFI of unexposed regions without electron beam exposure. GFP on silicon nitrite (SiN) microchips was exposed in ESEM at 30 kV with electron fluxes of 0.001 to 10 $e^-/Å^2s$ and accumulative electron doses of 0.001 to 100 $e^-/Å^2$. RFI = 0 indicates background level and the dotted line indicates 1/e. Data points are connected for better visualization.

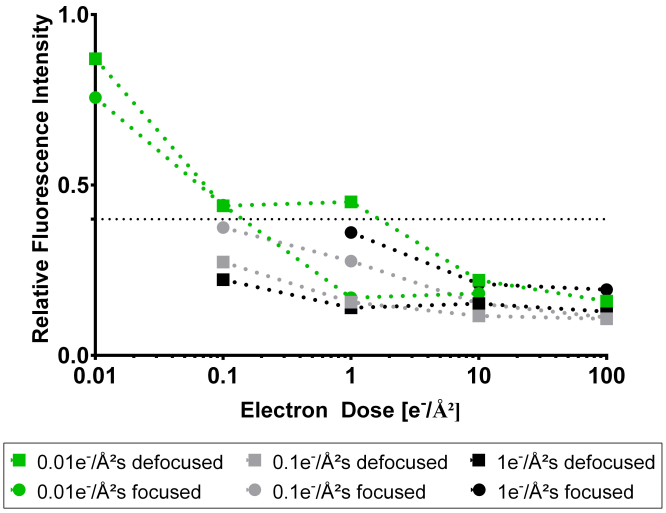

Figure 4.16: Comparison of electron beam exposure with a defocused and a focused electron beam in environmental scanning electron microscopy (ESEM) at 30 kV. The relative fluorescence intensity (RFI) of green fluorescent protein (GFP) over the electron dose is shown. Dots depict the electron beam exposure using a focused electron beam for electron fluxes of 0.01, 0.1 and 1 $e^-/Å^2$. Squares show the electron beam exposure using a defocused electron beam of about 2 mm for the same fluxes. RFI = 0 indicates background level and the dotted line indicates 1/e. Data points are connected for better visualization.

Table 8: Critical electron doses of green fluorescent protein on silicon nitrite in environmental scanning electron microscopy.

electron flux [$e^-/Å^2s$]	D_c exposed regions [$e^-/Å^2$]	D_c unexposed regions [$e^-/Å^2$]
0.001	< 0.001	-
0.01	< 0.1	-
0.1	< 0.1	< 0.1
1	< 1	< 10
10	< 1	< 1

electron dose had a major impact on the electron dose tolerance of GFP, while no significant influence of the electron flux was observed. In liquid-phase TEM, GFP was exposed in SiN liquid cells and in GLCs. Using GLCs, D_c increased to $10\,e^-/Å^2$ compared to $D_c < 0.01\,e^-/Å^2$ in SiN liquid cells. In ESEM, GFP on SiN was investigated and D_c was $< 0.1\,e^-/Å^2$ for most electron fluxes. The size of the electron probe did not have a major impact on the dose tolerance of GFP. The results of this chapter are summarized in **Table 9**.

Table 9: Results for the dose tolerance in liquid-phase electron microscopy.

Research question	**SiN liquid cells**	**GLCs**	**ESEM**
Critical electron dose D_c	$0.01\,e^-/Å^2$	$10\,e^-/Å^2$	$0.1\,e^-/Å^2$
Dependence on the electron flux	✗	✗	✗
Fluorescence degradation in unexposed regions	✓	✗	✓
Impact of beam energy	-	✗	-
Impact of beam size	-	-	✗

4.2 Discussion

Radiation damage of hydrated GFP during electron beam exposure was investigated in ESEM and liquid-phase TEM. Protein damage was analyzed by measuring fluorescence intensities upon each electron beam exposure. However, reduction of fluorescence could also result from photobleaching upon multiple exposures in fluorescence microscopy, rupture of the structure upon drying, and exposure to conditions in ESEM and TEM. Therefore, some control experiments were performed. For SiN, RFI decreased to 75 % for PBS and 60 % for HPLC-grade H_2O after 30 exposures of 500 ms. In GLCs, no photobleaching was observed before and after introduction to vacuum (**Figure 4.2**). For radiation experiments, photobleaching was neglected on SiN microchips as well as in GLCs since GFP samples were only exposed 4 - 5 times under the fluorescence microscope and RFI remained above 90 % for this period. Mean grey values were about three times higher for GFP in PBS than in HPLC-grade H_2O (**Figure 4.1b**). This is most likely caused by sensitivity of the fluorescence emission efficiency to conformational changes and protonation that can occur for example with changing pH, temperature and ionic strength.[155–159] The absence of ions in HPLC-grade H_2O changes the ionic strength and the pH of the solution. The pH of HPLC-grade H_2O (pH $\approx$ 7) is a little lower than of PBS (pH $\approx$ 7.4, see **Figure A.1**). However, the ionic strengths of the solutions are different. HPLC-grade H_2O is deionized and most of its ions have been removed (ionic strength $\approx$ 0).[160,161] PBS has higher ionic strength than HPLC-grade H_2O (169 mol/L, see appendix **Section A.4**). The difference in ionic strength can alter the fluorescence and causes increased fluorescence of GFP in PBS. For this reason, radiation experiments were performed in PBS. Another advantage of using PBS is the formation of salt crystals when PBS is dry. The absence of salt crystals during experiments indicated that GFP was still in liquid environment. In liquid phase experiments, it was essential to ensure that GFP remained hydrated. The fluorescence intensity decreased to background level upon drying (**Figure 4.3**). After placing dried GFP back in PBS, the fluorescence did not recover, indicating non-reversible damage of GFP. Since GFP is mostly used for processes in liquid, only few studies on dehydrated GFP exist. It was shown that the exposure of GFP to dehydration agents such as ethanol caused fluorescence quenching.[162] Proteins were

shown to denaturate after dehydration.[163,164] Drying most probably caused denaturation of GFP resulting in decreased fluorescence intensity. In the experiments shown here, damage of GFP seemed to be irreversible. However, a few studies reported fluorescence recovery after restoring the conformation of GFP.[165,166]

4.2.1 Electron Beam Damage of Green Fluorescent Protein in Liquid-Phase Electron Microscopy

The finding that GFP is intact when it fluoresces is important for analyzing the effects of electron beam irradiation on GFP. Fluorescence images of GFP exposed in TEM and ESEM were shown (**Figure 4.5** and **4.14**). Evaluation of both methods showed that the exposed ROIs at the edges of the SiN window were distinguishable from unexposed regions. The more pronounced decrease of RFI in exposed ROIs indicates damage of GFP due to electron beam exposure. As the electron dose increased, unexposed regions started to show decreased fluorescence intensity as well. No crystals were formed during radiation experiments, so it can be concluded that GFP was still in liquid. Hence, the decrease of RFI can only be explained with the electron beam exposure. Here, multiple processes are possible:

- **Protein detachment.** GFP was covalently bound to the surface of SiN microchips. These bonds can be disrupted by electron beam irradiation or bulging of the SiN membrane which occurs due to the pressure difference between the microscope and the liquid cell.[40,41] Bond rupture would cause GFP to detach from the surface and result in lower fluorescence intensity due to decreasing number of proteins on the surface.

- **Structural damage of GFP.** The structure of the protein itself can be disrupted by electron beam exposure. In particular, SE with low energy ($\leq 50\,\mathrm{eV}$) propagate through the specimen and cause damage. Although the protein is still attached to the surface, this results in decreased fluorescence intensity due to damaged GFP. Additionally, SE potentially also damage regions, that have not directly been exposed.

- **Changing liquid conditions.** Changing conditions in the liquid environment, such as a change in pH, can cause damage to GFP.[24] Radiolysis in

liquid cells creates ions, which in turn alter the pH.[37,167] Furthermore, radicals are created in the solvent during electron beam irradiation and cause damage to the specimen. Radical formation in solvents during EM has previously been studied in literature and scavenging properties of solvents like isopropanol were shown.[168] However, the effect of biocompatible solvents such as PBS has not been studied and requires further investigation.

4.2.1.1 Liquid-Phase Transmission Electron Microscopy

In liquid cell experiments in TEM, RFI overlapped for different electron fluxes at most electron doses (**Figure 4.6**). Even though bulging occurs when introducing the liquid cell to vacuum, the liquid thickness is more stable among different samples compared to ESEM. The exposure to TEM conditions did not lead to a decrease in RFI (**Figure 4.4**) The electron flux did not have a major impact on the radiation sensitivity of GFP. For an electron dose of $0.001\,e^-/Å^2$, RFI was still above 1/e, but was close to background level for $0.01\,e^-/Å^2$. However, in the experiments presented here, GFP was directly exposed to the electron beam. No surrounding materials covered GFP to protect it from the electron beam and the changing environment within the liquid cell.

It has been reported previously that graphene can scavenge radicals and consequently reduce radiation damage.[44,79] For this reason, graphene was introduced as support material. The liquid thickness of GLCs with GFP in PBS, PBS without GFP and GFP in HPLC-grade H_2O was examined using EELS (**Figure 4.7**). The liquid thickness of PBS was 40 ± 8 nm, which is consistent with literature.[169,170] Adding GFP to PBS increased the liquid thickness by one order of magnitude (380 ± 110 nm). For GFP in HPLC-grade H_2O, the liquid thickness increased similarly to 230 ± 140 nm. The concentration of GFP in PBS was 1 mg/mL and 0.5 mg/mL for HPLC-grade H_2O. Such high concentration of protein likely results in gel-like structures with increased viscosity and density, explaining the thicker liquid films compared to PBS.[171] However, the high liquid thickness presumably causes the protein to be distributed over the entire GLC rather than being enclosed in graphene pockets.

Despite the controlled thickness of the liquid films, radiation experiments of GFP in GLCs presented several other challenges:

- **Dark spots.** After the first electron beam exposure, dark spots were found in each exposed region of the GLCs. From EELS data, it was suggested that gel structures were formed in GLCs. Bubble formation in liquid upon electron beam exposure has been reported previously.[37,169,172,173] Bubbles result from radiolytically produced H· or gas dissolved in the liquid.[37,169] In gels, bubbles are more stable and can appear as dark spots in the fluorescence images. With increasing electron dose, these dark spots grew, resulting in decreased fluorescence intensity. The material, that is displaced by bubble formation may not evaporate due to the graphene layers and therefore, displaced GFP can move to surrounding places. This results in increased fluorescence intensity for areas surrounding exposed ROIs.

- **Determination of the exposed area.** In GLCs it was more challenging to analyze the exact area that was exposed. Due to the high liquid thickness, not a lot of electrons were transmitted and the area was very dim in TEM. Therefore, the exposed area could only be determined by the orientation of a standard grid. The position of exposed ROIs was identical, but since the orientation of the rectangles can change, this was only an indication of the area. In addition, the stage of the microscope may move when repeatedly removing and inserting the specimen, even though the position has been marked in the microscope software. **Appendix A.2** shows a stage shift of around 3.5 µm after moving to the same position 10x. This shift is negligible compared to the size of the grids ($\sim$ 50 µm). In fluorescence microscopy, exposed areas were distinguishable from unexposed areas.

RFI of GFP in GLCs in TEM at 200 kV decreased over increasing electron dose, but remained above 1/e up to an accumulative electron dose of 1 $e^-/Å^2$ (**Figure 4.10a**). Compared to SiN liquid cells, the dose tolerance of GFP was increased to 10 $e^-/Å^2$ using GLCs. SiN membranes are insulating which results in charging and enhanced electron dose at the liquid-solid interface when irradiated with an electron beam.[24,174] SiN membranes are then source of SE with energies $\leq$ 50 eV.[8,174] These electrons interact with the sample since the energy is too low to exit the specimen and create more SE leading to a cascade of SE. Creation of SE can be reduced by using less insulating membrane materials such as graphene. Graphene reduces

charge which results in less SE.[24] Furthermore, it can scavenge radicals and hence controls the chemical environment of the sample.[44,79] This reduces the electron beam damage of GFP on graphene substrate compared to SiN.
However, in addition to the previously mentioned factors, higher dose tolerance of GFP in GLCs compared to SiN liquid cells may as well be due to other aspects:

- **Liquid thickness.** The liquid layer in GLCs with GFP is quite thick compared to thicknesses reported in literature and with PBS alone (compare **Figure 4.7**). This might cause beam spreading at the surface of the GLC, so that the beam does not completely encounter the specimen. This would cause less electron dose on the sample than calculated. If the liquid layer is thinner, the beam can fully encounter the sample, which can reduce the dose tolerance compared to the dose tolerance shown here.

- **GFP binding.** GFP was not bound to the surface of graphene, so it could potentially move within the GLC. Consequently, the proteins irradiated were not necessarily the same in each exposure. Future studies should include binding of GFP to graphene to ensure exposure of the same proteins.

- **Protein detachment.** As mentioned above, SiN membranes are flexible and can bulge when exposed to vacuum, which could cause GFP to detach from the surface. This would result in lower RFI for exposed samples, but due to protein detachment rather than GFP damage. The actual dose tolerance of GFP might therefore be higher than shown in this study.

Electron dose tolerance of GFP has rarely been studied in literature before. Cathodoluminescence of GFP was used to study the electron dose tolerance.[175,176] However, GFP was air-dried on TEM grids in these studies. In the present study, GFP fluorescence degraded upon drying and could not be restored. Only a few radiation experiments in LP-EM were reported so far. The electron dose thresholds for biological samples reported in literature are mainly based on cryo-EM and vary widely. Some reports show radiation damage of biological samples at an electron dose of $1\,e^-/Å^2$.[177] Others report $D_c = 100\,e^-/Å^2$ for proteins in cryo-EM, while enzymes become inactive at $10\,e^-/Å^2$.[20] Different studies show dose tolerances for macromolecular complexes around 5-20 $e^-/Å^2$ and a dose tolerance of 50 -200 $e^-/Å^2$ for

whole cells in cryo-EM.[178] In LP-EM, the electron dose threshold of microtubules was increased to 700 $e^-/Å^2$ using GLCs, which is one order of magnitude higher than in amorphous ice.[26] In comparison to literature, the electron dose tolerance for GFP in this study was very low.
GLCs with GFP were also investigated at lower beam energy of 30 kV and compared to GFP exposed at 200 kV (**Figure 4.12**). No dependence of the dose tolerance of GFP on the beam energy was observed, indicating no significant impact of elastic scattering events on the dose tolerance of GFP.
Unexposed areas in GLCs showed a decrease in RFI of up to 30 % while unexposed areas in SiN liquid cells decreased below background level (**Figure 4.13b**). Exposed regions seemed to expand into the center of the SiN membrane (**Figure 4.5**). The expansion indicates that electrons encountering the specimens further propagated through the liquid and damaged molecules outside exposed ROIs. In SiN liquid cells, the area suitable for analysis was limited to the size of the transparent SiN window. Thus, unexposed areas were within a few hundred micrometers from exposed ROIs. In GLCs, unexposed regions were analyzed in the center of the GLCs. This results in larger distances between exposed ROIs and unexposed regions (compare **Figure 4.8**). Therefore, unexposed regions in GLCs were not as affected by electron beam irradiation compared to unexposed regions in SiN liquid cells.

4.2.1.2 Environmental Scanning Electron Microscopy

GFP in ESEM showed decreasing RFI as well. However, explanations of radiation effects in ESEM are more complex and need to consider aspects such as:

- **Liquid thickness variations.** In the ESEM setup used in this study, the liquid thickness cannot be controlled quantitatively. To be able to detect the SiN window, the pressure required in the sample chamber varied between samples and therefore, the liquid thickness for each sample was different. If the liquid layer is too thick, electrons spread more widely so that unexposed areas can also be affected (compare with **Figure 2.2**). The liquid film covering the samples absorbs electrons, which effectively reduces the calculated electron dose. In addition, the primary electron beam can scatter at gas molecules, which further reduces the effective electron dose and affects unexposed areas

(see **Figure 2.5b**). A system with controlled liquid thickness is necessary to ensure the same liquid thickness for all samples.

- **Chamber pressure variations.** As mentioned above, the chamber pressure that was required to visualize the SiN window varied between samples. The control in ESEM (**Figure 4.4**) showed that exposure to ESEM conditions can cause a decrease of RFI. Some samples required higher vacuum than others, which can potentially result in lower RFI for those samples.

For these reasons, it is difficult to compare the electron dose of different samples even if exposed with the same electron flux and electron dose. As shown in **Figure 4.15a** an electron flux of $0.001\,e^-/Å^2s$ showed higher radiation sensitivity compared to 0.01, 0.1 and $1\,e^-/Å^2s$ for higher electron dose. However, due to changing liquid thickness, it was not possible to ensure that the electron beam irradiated all samples with the same intensity. Therefore, the flux dependence might be an artifact arising from varying liquid thickness. Considering that all electron fluxes showed RFI below 1/e at an accumulative electron dose of $0.1\,e^-/Å^2$, it can still be concluded that $D_c < 0.1\,e^-/Å^2$.

4.3 Conclusion

In this chapter, electron beam damage of GFP was investigated in LP-EM. The following conclusions can be drawn:

1. GFP in ESEM ($D_c < 0.1\,e^-/Å^2$) showed higher dose tolerance than in SiN liquid cells in liquid-phase TEM ($D_c < 0.01\,e^-/Å^2$). This was mainly associated with beam spreading due to uncontrollable liquid thickness in ESEM and the uncertainty that the calculated electron dose actually encountered the specimen.

2. Encapsulation of GFP in GLCs increased the dose tolerance in TEM compared to SiN liquid cells. RFI did not decrease below 1/e up to an accumulated electron dose of $10\,e^-/Å^2$.

3. The dose tolerance of GFP was only dependent on the accumulative electron dose and independent of the electron flux. This implies that the electrons

passing the sample per unit area per unit time did not have a major impact on the electron dose tolerance.

4. The dose tolerance was independent of the beam energy. This indicates that elastic scattering events were not the main cause for radiation damage of GFP in LP-EM.

5 Electron Beam Damage of SKBR3 Cells Labeled with Green Fluorescent Protein in Liquid-Phase Electron Microscopy

In this chapter, the electron dose tolerance of GFP in fixed SKBR3 cells was investigated. GFP was bound to actin filaments of SKBR3 cells for labeling. Radiation damage was investigated using RFI of GFP and the area of SKBR3 cells. For all experiments in this chapter, SKBR3 cells were chemically fixed with PFA. The following questions will be addressed:

- Can electron dose thresholds for single proteins be applied to more complex systems such as cells?
- Do SKBR3 cells remain hydrated in liquid cells during electron beam irradiation?

Electron beam damage of SKBR3 cells labeled with GFP was examined in ESEM and liquid-phase TEM. Protein damage was studied using the fluorescence of GFP as a marker. Fluorescent SKBR3 cells indicated intact GFP and degradation of the fluorescence was correlated with protein damage. Damage of GFP can indicate damage of other cellular proteins. To study beam damage, fluorescence intensities of GFP upon electron beam irradiation were analyzed. Reference images were acquired with fluorescence microscopy prior to electron beam exposure showing the fluorescence intensities of GFP in SKBR3 cells under native conditions. SKBR3 cells were exposed with the electron beam and after each exposure, the specimen was removed from the electron microscope to record fluorescence images. The electron dose was logarithmically increased from one exposure to the next. The fluorescence intensity relative to the fluorescence intensity of the reference was evaluated (relative fluorescence intensity, RFI). Each data point represents the analysis of one fluorescence image. For analysis, SKBR3 cells were divided in different categories which were defined as follows:

- **expressing**: SKBR3 cells were fixed with PFA, incubated with CellLight™ Actin-GFP as described in **Section 3.3.3** and expressed GFP.

- **non-expressing**: SKBR3 cells were fixed with PFA and incubated with CellLight™ Actin-GFP as described in **Section 3.3.3** but did not express GFP.
- **unlabeled**: SKBR3 cells were fixed with PFA but not incubated with CellLight™ Actin-GFP.
- **exposed**: SKBR3 cells were directly exposed to the electron beam.
- **unexposed**: SKBR3 cells were located on the same SiN microchip as exposed cells but were not directly exposed to the electron beam.

Figure 5.1 shows DIC and fluorescence images of GFP labeled and fixed SKBR3 cells in a SiN liquid cell. The cell categories are marked in color. Non-expressing SKBR3 cells are shown in the DIC channel in **Figure 5.1a**. The yellow box shows exposed cells and the purple box marks unexposed cells. The fluorescence channel in **Figure 5.1b** shows GFP expressing SKBR3 cells. Expressing and exposed SKBR3 cells are marked with a blue box and expressing but unexposed cells are marked with a white box. The overlay in **Figure 5.1c** depicts all cell categories.

As in **Chapter 4**, electron doses and electron fluxes were chosen in the range of 0.001 - 100 $e^-/Å^2$ and 0.001 - 100 $e^-/Å^2s$, respectively. Degradation of RFI was shown for GFP expressing SKBR3 cells with increasing electron dose. However, after decreasing, RFI increased for all cells in TEM. In ESEM, RFI decreased over the electron dose. Control experiments including photobleaching, drying, autofluorescence and exposure to ESEM and TEM conditions were performed before electron beam irradiation experiments to distinguish between these effects and electron beam effects.

5.1 Results

5.1.1 Controls

As mentioned in **Chapter 4**, photobleaching is an important aspect to consider when working with fluorescent proteins. Photobleaching was investigated in GFP expressing SKBR3 cells. In addition, cellular components and aldehyde fixatives

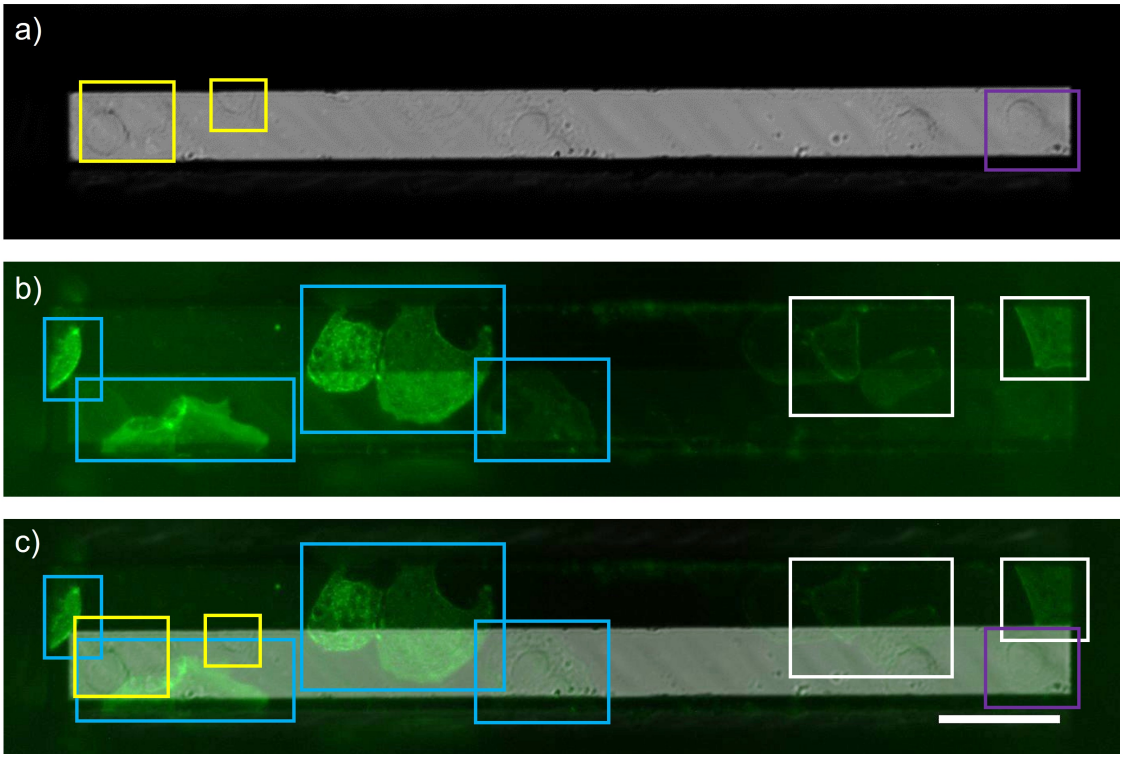

Figure 5.1: Overview of fixed SKBR3 cells labeled with green fluorescent protein (GFP) in a silicon nitrite (SiN) liquid cell. a) Differential interference contrast (DIC) shows non-expressing SKBR3 cells exposed to the electron beam marked in yellow. Unexposed and non-expressing cells are marked in purple. b) Fluorescence channel (L5). Exposed and expressing SKBR3 cells are marked in blue. Unexposed and expressing SKBR3 cells are marked in white. c) Combined overlay of DIC and L5. Different categories of SKBR3 cells are shown. Scale bars are 50 µm.

may autofluoresce.[179,180] Autofluorescence was investigated in unlabeled SKBR3 cells. Image series were acquired with one image per minute over 30 min. An exposure time of 500 ms was chosen so that GFP fluorescence was detected, but did not over-saturate. For autofluorescence, the same exposure time was chosen. For both, photobleaching and autofluorescence, stable RFI around 100 % is desired. Decreasing RFI would indicate photobleaching during exposure to light and increasing RFI of unlabeled cells would indicate autofluorescence upon light exposure. Note that SKBR3 cells were washed before fixation, so the CellLight™ Actin-GFP construct did not contribute to the fluorescence.

Figure 5.2a shows the RFI of expressing and unlabeled SKBR3 cells. Express-

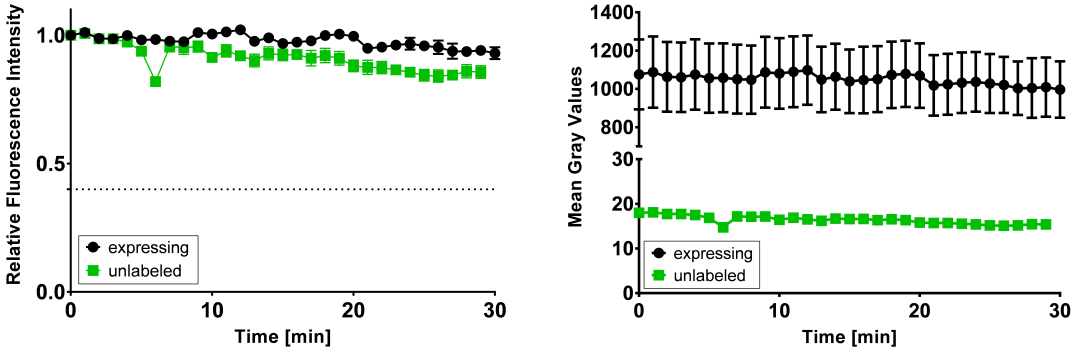

(a) (b)

Figure 5.2: Photobleaching and autofluorescence of green fluorescent protein (GFP) expressing and unlabeled SKBR3 cells. a) Relative fluorescence intensity (RFI) and b) mean grey value over time. GFP expressing (black dots) and unlabeled (green squares) SKBR3 cells on silicon nitrite (SiN) microchips were exposed in phosphate buffered saline (PBS) under fluorescence microscopy for 30 min with 1 image/min and an exposure time of 500 ms per image. RFI = 0 indicates background level and the dotted line indicates 1/e. Data points are connected for better visualization.

ing cells show photobleaching of GFP and unlabeled cells show autofluorescence of cellular components or PFA. RFI remained stable around 100 % over time and no photobleaching and autofluorescence increase was observed. **Figure 5.2b** shows mean grey values of GFP expressing and unlabeled SKBR3 cells. Mean grey values of the silicon microchip were subtracted as background. Mean grey values for expressing cells were 60x higher than for unlabeled cells. This indicates that PFA and cellular components did not contribute to the fluorescence of GFP when exposed to light.

The effect of drying was investigated in GFP expressing and unlabeled SKBR3 cells. 1 µL H_2O was added on top of the microchip and imaged during drying. Image series were acquired with one image per minute over 30 min. An exposure time of 900 ms for expressing and 500 ms for unlabeled cells was chosen so that GFP fluorescence was detected, but did not over-saturate. The autofluorescence upon drying was investigated using unlabeled SKBR3 cells. **Figure 5.3a** shows the RFI and **Figure 5.3b** shows mean grey values for expressing and unlabeled SKBR3 cells over time. The points of drying are marked in blue (4 min) and

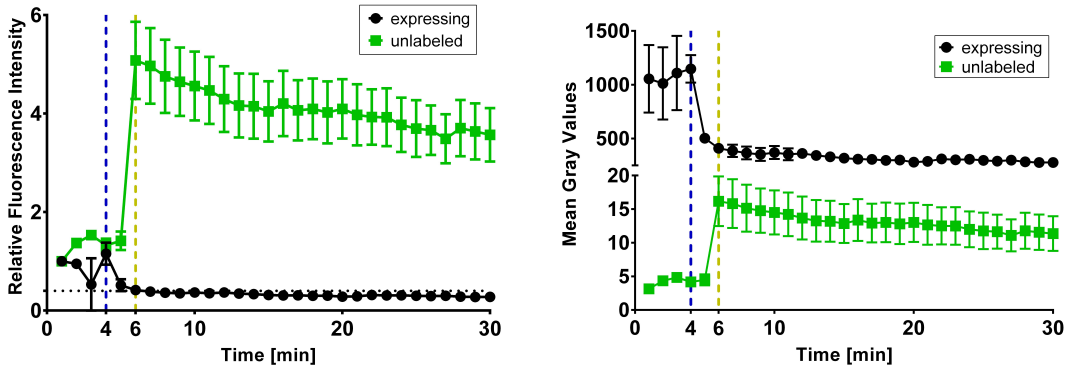

(a) (b)

Figure 5.3: Drying of green fluorescent protein (GFP) expressing and unlabeled SKBR3 cells. a) Relative fluorescence intensity (RFI) and b) Mean grey values of GFP in SKBR3 cells upon drying. GFP expressing (black dots) and unlabeled (green squares) SKBR3 cells are shown. RFI = 0 and mean grey values = 0 indicate background level. The dotted line indicates 1/e. The blue dashed line indicates the point of drying after 4 min for expressing SKBR3 cells and the yellow line indicates drying after 6 min for unlabeled SKBR3 cells. Data points are connected for better visualization.

yellow (6 min) for expressing and unlabeled cells, respectively. GFP expressing cells showed decreasing RFI over time, with a decrease of 50 % after drying. After 7 min, RFI of GFP expressing cells decreased below 1/e. Unlabeled cells showed a 5-fold increase in RFI upon drying (after 6 min) and decreased to 400 % over time. **Figure 5.3b** depicts the mean grey values of GFP in SKBR3 cells. Expressing cells showed mean grey values around 1000 before drying and decreased to around 500 after drying. Unlabeled cells showed mean grey values close to background level (mean grey value = 0) and increased upon drying to about 15 mean grey values.
The resistance of GFP in SKBR3 cells to the imaging conditions of ESEM and TEM was investigated. Samples were introduced to ESEM at 4°C and 750 Pa for 5 min and a total of 4 times, resulting in 20 min of ESEM exposure. SKBR3 cells prepared in a SiN liquid cell were introduced to TEM conditions at 1.5×10^{-5} Pa for 5 min for a total of 5 times resulting in 25 min of TEM exposure. **Figure 5.4a** shows the RFI and **Figure 5.4b** shows the relative area for GFP expressing SKBR3 cells in ESEM and TEM over time. RFI decreased to 50 % of its initial fluorescence intensity after 20 min in ESEM. Cells contracted to 80 % of their initial area after

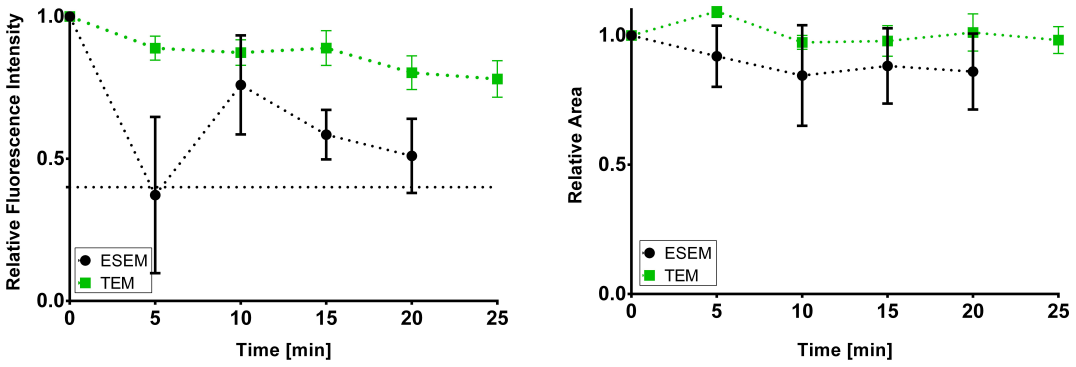

(a) (b)

Figure 5.4: Exposure of green fluorescent protein (GFP) expressing SKBR3 cells to electron microscopy conditions. a) Relative fluorescence intensity (RFI) and b) Relative area in environmental scanning electron microscopy (ESEM) conditions at 750 Pa and 4°C (black dots) and transmission electron microscopy (TEM) conditions at 1.5×10^{-5} Pa (green squares) over time. RFI = 0 and the dotted line indicates 1/e. Data points are connected for better visualization.

20 min in ESEM. In TEM, RFI decreased to about 80 % of the initial fluorescence intensity and the area of the cells remained stable around 100 %. The changes in cell area were analyzed as described in **Section 3.3.9**. Decreasing area might indicate cell contraction due to drying and will be discussed in **Section 5.2**.

Autofluorescence can also be induced by irradiation with an electron beam.[181] For this reason, unlabeled SKBR3 cells were exposed in TEM and ESEM. **Figure 5.5** shows unlabeled SKBR3 cells exposed in TEM at 200 kV and ESEM at 30 kV. Samples were exposed at a constant electron flux of $1\,e^-/Å^2s$ and increasing electron doses ranging from 0.1 to $100\,e^-/Å^2$. **Figure 5.5a** shows the RFI over the electron dose. For both, TEM and ESEM, RFI increased over electron dose. For cells exposed in TEM, RFI increased 50-fold at an accumulated electron dose of $100\,e^-/Å^2$. In ESEM, RFI showed 10-fold increase at an accumulated electron dose of $100\,e^-/Å^2$. This implies that electron beam exposure causes increasing autofluorescence in unlabeled SKBR3 cells with increasing electron dose. **Figure 5.5b** shows the relative area of the cells. For both, TEM and ESEM, the area of the cells remained stable up to an accumulative electron dose of $100\,e^-/Å^2$.

In conclusion, no photobleaching was observed for GFP expressing SKBR3 cells

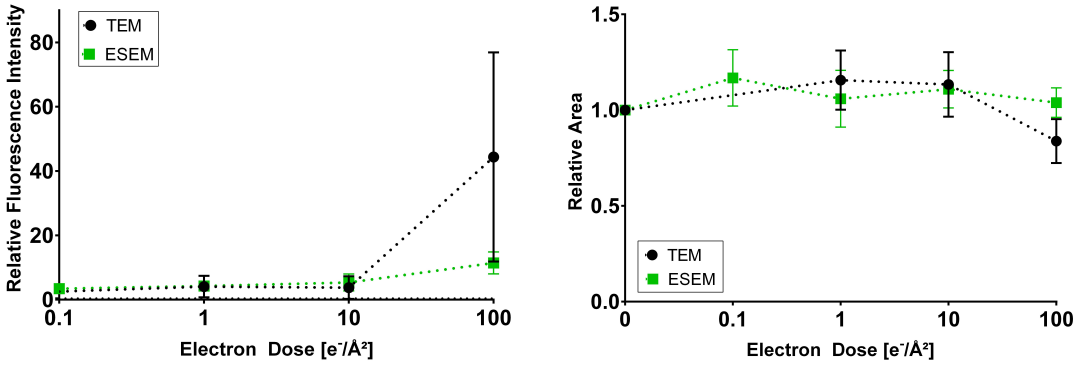

(a) (b)

Figure 5.5: Unlabeled SKBR3 cells exposed in transmission electron microscopy (TEM) and environmental scanning electron microscopy (ESEM) a) Relative fluorescence intensity (RFI) and b) Relative area of unlabeled SKBR3 cells over the electron dose exposed in TEM at 200 kV and ESEM at 30 kV. Black dots depict cells exposed in TEM and green squares depict cells exposed in ESEM. Cells were exposed with a constant electron flux of $1\,e^-/Å^2s$ and logarithmically increasing electron doses from $0.001 - 100\,e^-/Å^2$. RFI = 0 indicates background level and an electron dose of $0\,e^-/Å^2$ indicates the reference values after vacuum (9.3 Pa for 30 s). Data points are connected for better visualization.

in fluorescence microscopy. With the exposure to light, RFI of unlabeled SKBR3 cells remained stable and no increasing autofluorescence was observed. Mean grey values for unlabeled cells were close to background level, which indicates, that PFA and cellular components did not contribute to the fluorescence of SKBR3 cells. Upon drying, RFI of GFP expressing cells decreased, while RFI of unlabeled cells increased. This indicates, that autofluorescence contribution was more pronounced if cells were dry. However, GFP fluorescence of expressing SKBR3 cells degraded when the cells were dry. After exposure to ESEM conditions, RFI of GFP expressing SKBR3 cells decreased. This means, that the exposure to ESEM conditions affects the fluorescence and needs to be considered in the radiation experiments. Under TEM conditions, RFI decreased about 20 % over time, indicating that TEM conditions contributed to the decrease in RFI, however, less than ESEM conditions. In addition, it was observed that unlabeled SKBR3 cells showed increasing RFI when exposed to the electron beam in TEM and ESEM. This implies, that electron beam exposure induced autofluorescence and will be discussed in **Sec-**

tion 5.2.

5.1.2 Labeled SKBR3 Cells in Liquid-Phase Transmission Electron Microscopy

The dose tolerance of GFP bound to actin-filaments of SKBR3 cells was investigated in liquid-phase TEM with varying electron dose and electron flux. The changes in RFI were measured by comparing the fluorescence intensities after each electron beam exposure to the reference in vacuum. **Figure 5.6** depicts DIC, fluorescence (L5) and combined overlay images of SKBR3 cells labeled with GFP and prepared in a SiN liquid cell for TEM. **Figure 5.6a - c** depicts the reference images after introduction to vacuum (9.3 Pa for 30 s). **Figure 5.6d - l** show images after each electron beam exposure and the last row shows images after disassembly of the liquid cell and placing the sample in PBS. GFP expressing SKBR3 cells are marked in blue and cells that did not express GFP before electron beam exposure are marked in yellow. The left part of the microchip was exposed to the electron beam in TEM at 200 kV with a constant electron flux of $0.01\,e^-/Å^2s$ and logarithmically increasing electron dose ranging from $0.01\,e^-/Å^2$ for the first exposure to $1\,e^-/Å^2$ for the last exposure. GFP expressing cells showed decreasing fluorescence upon electron beam irradiation up to an accumulated electron dose of $0.1\,e^-/Å^2$ (**Figure 5.6** blue rectangles). Cells that did not express GFP before electron beam exposure started to fluoresce after the first electron beam exposure at $0.01\,e^-/Å^2$ (**Figure 5.6** yellow rectangles). With increasing electron dose the fluorescence of those cells increased. At an accumulative electron dose of $1\,e^-/Å^2$, the fluorescence intensity of all exposed SKBR3 cells increased (**Figure 5.6k, l**). After disassembly of the SiN liquid cell, liquid repellency of the sample is visible in the DIC channel (**Figure 5.6m**).

Figure 5.7a shows the RFI over the electron dose for GFP expressing SKBR3 cells exposed in TEM at 200 kV with electron fluxes ranging from 0.001 to $10\,e^-/Å^2s$ (cells marked in blue in **Figure 5.1**). Electron doses increased logarithmically from $0.001\,e^-/Å^2$ for the first exposure to $10\,e^-/Å^2$ for the last exposure. RFI decreased for electron fluxes of 0.001 and $0.01\,e^-/Å^2s$ up to an accumulated electron dose of $0.1\,e^-/Å^2$. RFI decreased for an electron flux of $1\,e^-/Å^2s$ up to an accumulated

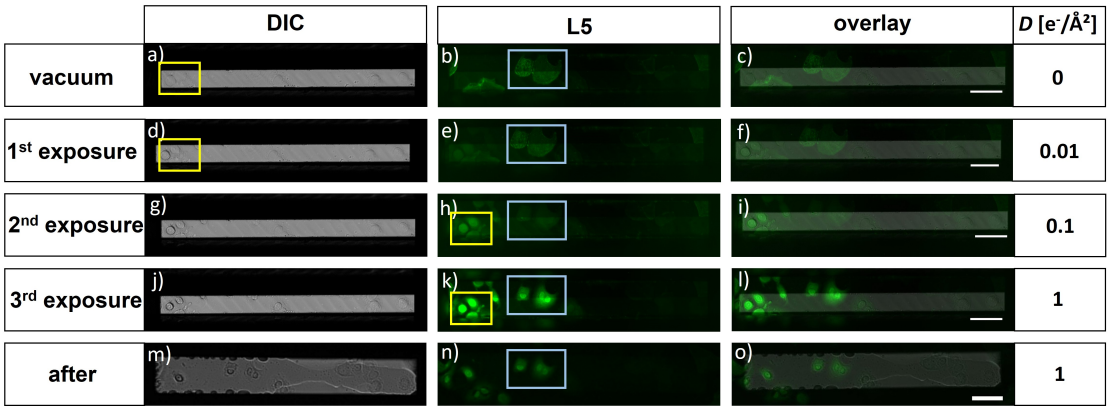

Figure 5.6: Fluorescence images of SKBR3 cells labeled with green fluorescent protein (GFP) in transmission electron microscopy (TEM) at 200 kV. Images of differential interference contrast (DIC), fluorescence (L5) and the combined overlay during electron beam exposure are shown. The first row depicts the reference images after exposure to vacuum (9.3 Pa for 30 s). Rows 2 - 4 show the images after electron beam exposure with a constant electron flux of 0.01 $e^-/Å^2s$ and electron doses of 0.01 $e^-/Å^2$ for 1st, 0.1 $e^-/Å^2$ for 2nd and 1 $e^-/Å^2$ for 3rd exposure. The last row shows images after disassembly of the liquid cell and placing the sample back in phosphate buffered saline (PBS). Blue rectangles show exposed and GFP expressing SKBR3 cells. Yellow rectangles show exposed cells that did not express GFP before electron beam exposure. Scale bars are 50 µm.

electron dose of 10 $e^-/Å^2$. For electron fluxes of 0.01 and 0.1 $e^-/Å^2s$, RFI increased at electron doses of 1 and 10 $e^-/Å^2$, respectively. For 10 $e^-/Å^2s$, RFI increased 12-fold at an electron dose of 10 $e^-/Å^2$. $D_c < 0.1\,e^-/Å^2$ for electron fluxes of 0.001 and 0.1 $e^-/Å^2s$. However, RFI increased after D_c for an electron flux of 0.1 $e^-/Å^2s$. **Figure 5.7b** shows the area of the SKBR3 cells over the electron dose. The area of the cells decreased over the electron dose for all electron fluxes. The largest decrease occurred for an electron flux of 1 $e^-/Å^2s$, where the area reduced to 50 % of the initial area.

Figure 5.8 shows the RFI (**Figure 5.8a**) and relative area (**Figure 5.8b**) over the electron dose of non-expressing SKBR3 cells exposed to the electron beam (cells marked in yellow in **Figure 5.1**). For all electron fluxes, RFI increased with increasing electron dose and did not decrease below 1/e. The area of the cells decreased to a maximum of 60 % of their initial area.

Figure 5.9a shows the RFI over the electron dose for expressing and unexposed

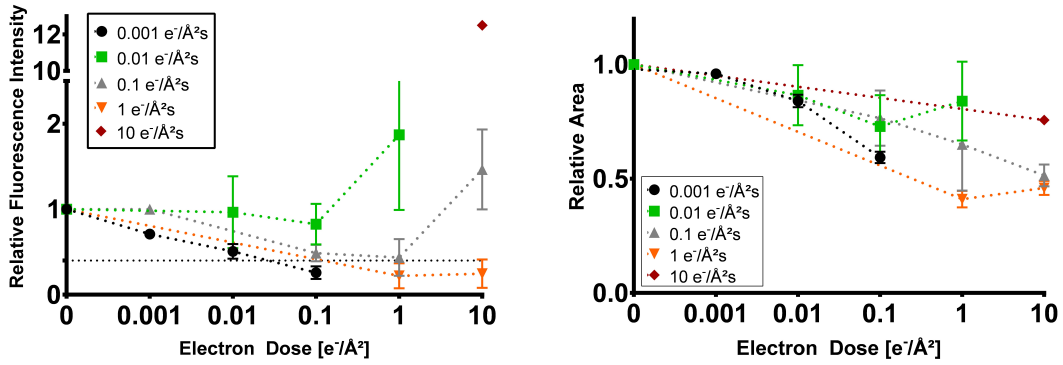

(a) (b)

Figure 5.7: Green fluorescent protein (GFP) expressing SKBR3 cells exposed in transmission electron microscopy (TEM) at 200 kV. a) Relative fluorescence intensity (RFI) and b) Relative area of GFP expressing SKBR3 cells over the electron dose. RFI = 0 indicates background level and the dotted line indicates 1/e. An electron dose of 0 $e^-/Å^2$ depicts the reference values after introduction to vacuum (9.3 Pa for 30 s). Data points are connected for better visualization.

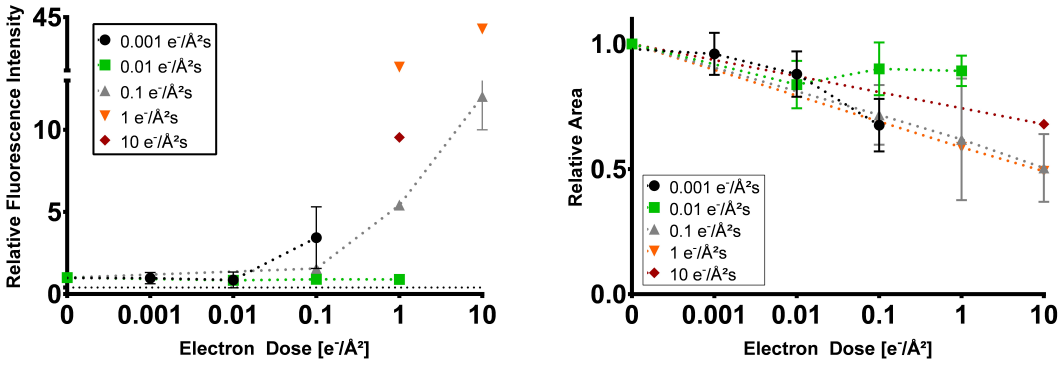

(a) (b)

Figure 5.8: Non-expressing SKBR3 cells exposed in transmission electron microscopy (TEM) at 200 kV. a) Relative fluorescence intensity (RFI) and b) Relative area of non-expressing SKBR3 cells over the electron dose. RFI = 0 indicates background level and the dotted line indicates 1/e. An electron dose of 0 $e^-/Å^2$ depicts the reference values after introduction to vacuum (9.3 Pa for 30 s). Data points are connected for better visualization.

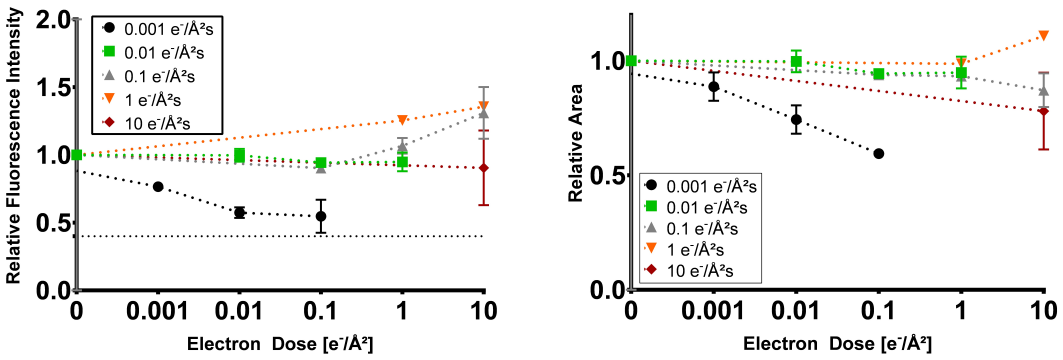

(a) (b)

Figure 5.9: Green fluorescent protein (GFP) expressing and unexposed SKBR3 cells in transmission electron microscopy (TEM). a) Relative fluorescence intensity (RFI) and b) Relative area of GFP expressing and unexposed SKBR3 cells over the electron dose. RFI = 0 indicates background level and the dotted line indicates 1/e. An electron dose of $0\,e^-/Å^2$ depicts the reference values after introduction to vacuum (9.3 Pa for 30 s). Data points are connected for better visualization.

SKBR3 cells (cells marked in white in **Figure 5.1**). RFI decreased for an electron flux of $0.001\,e^-/Å^2s$ over the electron dose. RFI remained stable for electron fluxes of 0.01 and $0.1\,e^-/Å^2s$ up to an accumulative electron dose of $1\,e^-/Å^2$. RFI increased for an electron flux of $0.1\,e^-/Å^2s$ at an electron dose of $1\,e^-/Å^2$. For an electron flux of $1\,e^-/Å^2s$, RFI increased over the electron dose. For an electron flux of $10\,e^-/Å^2s$, RFI remained stable. RFI remained above 1/e for all electron fluxes. **Figure 5.9b** shows the area for expressing and unexposed SKBR3 cells. The area remained stable around 100 % for electron fluxes of 0.01 - $10\,e^-/Å^2s$. For an electron flux of $0.001\,e^-/Å^2s$, the area decreased to 60 %.

Figure 5.10 shows the RFI (**Figure 5.10a**) and relative area (**Figure 5.10b**) over the electron dose for unexposed and non-expressing SKBR3 cells (cells marked in purple in **Figure 5.1**). RFI increased over the electron dose for all electron fluxes. The area of the cells decreased over the electron dose for an electron flux of $0.001\,e^-/Å^2s$ to 65 % of the initial area. For electron fluxes of 0.01 and $1\,e^-/Å^2s$, the area decreased to 80 % of the initial area with increasing electron dose. For an electron flux of $10\,e^-/Å^2s$, the area remained stable.

In conclusion, RFI increased for all SKBR3 cells in TEM. Only for exposed and

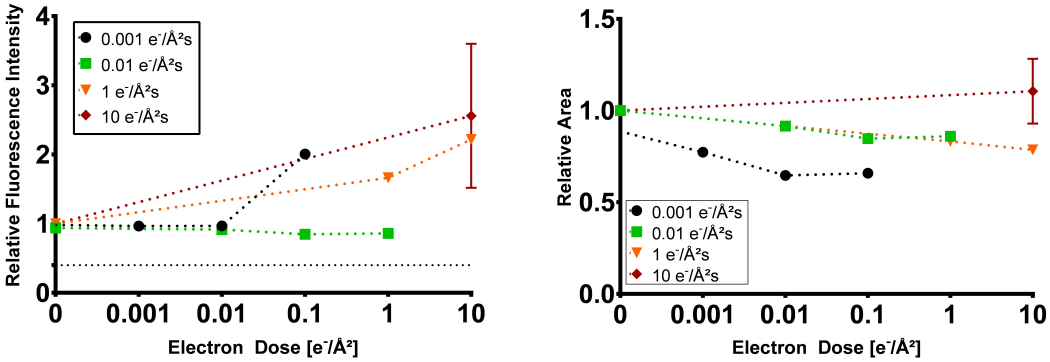

(a) (b)

Figure 5.10: Non-expressing and unexposed SKBR3 cells in transmission electron microscopy (TEM). a) Relative fluorescence intensity (RFI) and b) Relative area of non-expressing and unexposed SKBR3 cells over the electron dose. RFI = 0 indicates background level and the dotted line indicates 1/e. An electron dose of $0\,e^-/Å^2$ depicts the reference values after introduction to vacuum (9.3 Pa for 30 s). Data points are connected for better visualization.

expressing cells, RFI decreased before it increased. However, $D_c < 0.1\,e^-/Å^2$ was observed from the RFI for these cells. The control experiments showed that RFI increased for dry SKBR3 cells. The fluorescence images showed that liquid repellency was observed after radiation experiments. The liquid repellency and the increasing RFI for dry cells indicated that drying can be a reason for increasing RFI of exposed SKBR3 cells. Additionally, increasing autofluorescence caused either by the electron beam or by drying can result in increasing RFI. All exposed cells showed decreasing area with increasing electron dose while the area of unexposed cells remained stable.

5.1.3 Labeled SKBR3 Cells in Environmental Scanning Electron Microscopy

GFP bound to actin-filaments in SKBR3 cells was also investigated in ESEM at 30 kV and varying electron fluxes and electron doses to study the effect of an open, charge compensating system. **Figure 5.11** depicts DIC, fluorescence (L5) and combined overlay images of GFP labeled SKBR3 cells on a SiN microchip exposed in ESEM at 30 kV. The first row shows reference images before electron beam expo-

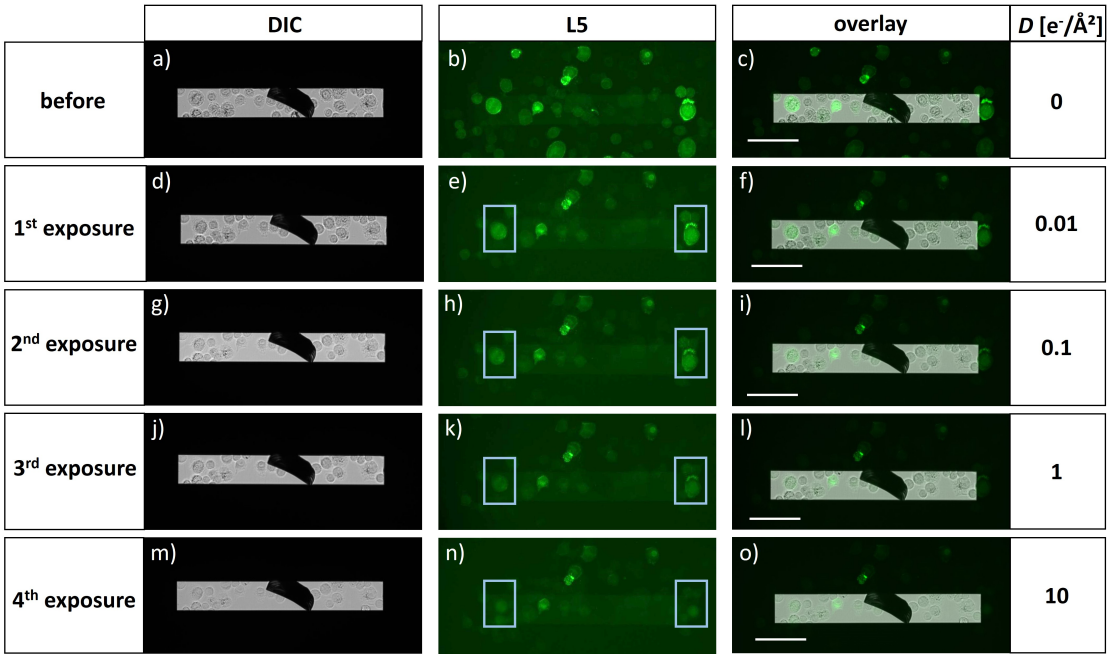

Figure 5.11: Fluorescence images of green fluorescent protein (GFP) labeled SKBR3 cells in environmental scanning electron microscopy (ESEM) at 30 kV. Images of differential interference contrast (DIC), fluorescence (L5) and the combined overlay during electron beam exposure in ESEM are shown. The first row depicts the reference images prior to electron beam exposure. Rows 2 - 5 show the images after electron beam exposure with a constant electron flux of $0.1\,e^-/Å^2s$ and electron doses of $0.01\,e^-/Å^2$ for 1st, $0.1\,e^-/Å^2$ for 2nd, $1\,e^-/Å^2$ for 3rd and $10\,e^-/Å^2$ for 4th exposure. Blue rectangles show exposed and GFP expressing SKBR3 cells. Scale bars are 100 µm.

sure. Rows 2 - 5 show images after each electron beam exposure. Exposed cells are marked in blue. Cells were irradiated with a constant electron flux of $0.1\,e^-/Å^2s$ and logarithmically increasing electron dose ranging from $0.01\,e^-/Å^2$ for the first exposure to $10\,e^-/Å^2$ for the last exposure. Exposed cells showed decreased fluorescence intensity with increasing electron dose.

RFI and relative area of GFP expressing SKBR3 cells exposed in ESEM at 30 kV over the electron dose are shown in **Figure 5.12a** and **b**, respectively (cells marked in blue in **Figure 5.1**). SKBR3 cells were exposed with electron fluxes of 0.001, 0.01, 0.1 and $10\,e^-/Å^2s$ and electron doses ranging from 0.001 to $100\,e^-/Å^2$. RFI decreased for all electron fluxes up to an accumulated electron dose of $1\,e^-/Å^2$. For an electron flux of $10\,e^-/Å^2s$, RFI increased at an electron dose of $1\,e^-/Å^2$

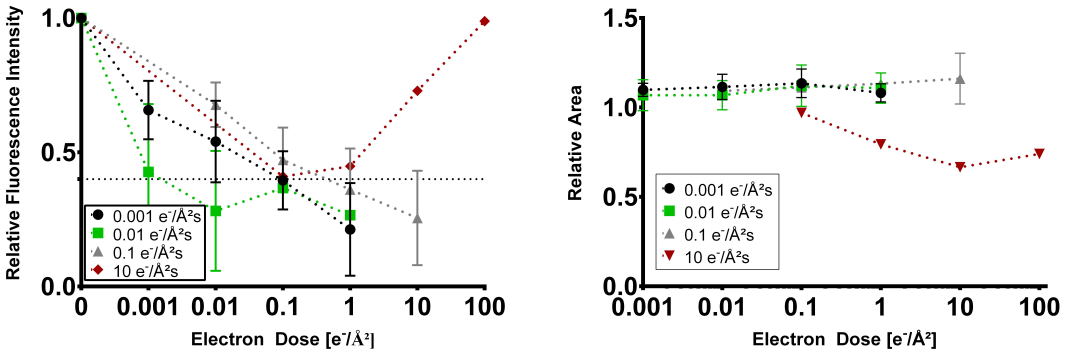

(a) (b)

Figure 5.12: Green fluorescent protein (GFP) expressing SKBR3 cells exposed in environmental scanning electron microscopy (ESEM) at 30 kV. a) Relative fluorescence intensity (RFI) and b) Relative area of GFP expressing SKBR3 cells over the electron dose. RFI = 0 indicates background level and the dotted line indicates 1/e. An electron dose of $0\,e^-/Å^2$ depicts the reference values prior to electron beam exposure. Data points are connected for better visualization.

and remained above 1/e up to an accumulated electron dose of $100\,e^-/Å^2$. $D_c < 0.1\,e^-/Å^2$ for an electron fluxes of $0.001\,e^-/Å^2s$. $D_c < 1\,e^-/Å^2$ for an electron flux of $0.1\,e^-/Å^2s$ and $D_c < 0.01\,e^-/Å^2$ for an electron flux of $0.01\,e^-/Å^2s$. The area remained stable at 100% for electron fluxes of 0.001, 0.01 and $0.1\,e^-/Å^2s$. For an electron flux of $10\,e^-/Å^2s$, the area decreased to 65 % of the initial area at an electron dose of $10\,e^-/Å^2$.

Figure 5.13a shows the RFI of expressing and unexposed SKBR3 cells (cells marked in white in **Figure 5.1**). RFI decreased with increasing electron dose for all electron fluxes. $D_c < 0.1\,e^-/Å^2$ for an electron flux of $0.1\,e^-/Å^2s$, $D_c < 1\,e^-/Å^2$ for an electron flux of $0.001\,e^-/Å^2s$ and $D_c < 100\,e^-/Å^2$ for an electron flux of $10\,e^-/Å^2s$. For an electron flux of $0.01\,e^-/Å^2s$, RFI remained above 1/e up to an accumulated electron dose of $1\,e^-/Å^2$. **Figure 5.13a** shows the area of expressing and unexposed SKBR3 cells. The area remained stable around 100 % over the electron dose for electron fluxes of 0.001, 0.01 and $10\,e^-/Å^2s$. For an electron flux of $0.1\,e^-/Å^2s$, the area showed an increase of 20 % up to an accumulated electron dose of $1\,e^-/Å^2$ and decreased to 100 % at an electron dose of $10\,e^-/Å^2$.

In conclusion, exposed cells showed decreasing RFI for all electron fluxes and an

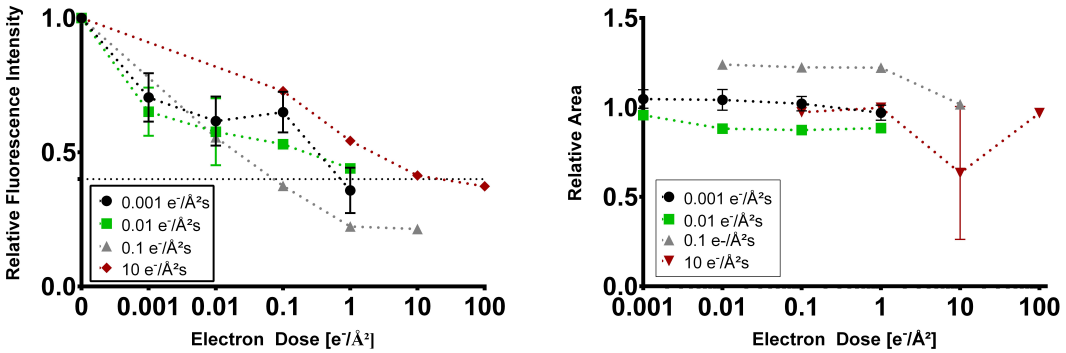

Figure 5.13: Green fluorescent protein (GFP) expressing and unexposed SKBR3 cells in environmental scanning electron microscopy (ESEM). a) Relative fluorescence intensity (RFI) and b) Relative area of GFP expressing SKBR3 cells over the electron dose without electron beam exposure. RFI = 0 indicates background level and the dotted line indicates 1/e. An electron dose of $0\,e^-/Å^2$ depicts the reference values before electron beam exposure. Data points are connected for better visualization.

increase in RFI was observed for high electron flux only ($10\,e^-/Å^2s$). Unexposed cells still showed a decrease in RFI, however less than exposed cells. Compared to TEM, SKBR3 cells did not show liquid repellency after electron beam exposure. No changes in area were observed for exposed and unexposed cells for most electron fluxes when exposed in ESEM at 30 kV.

5.2 Discussion

Radiation damage of GFP labeled SKBR3 cells was investigated in LP-EM. GFP was bound to actin filaments of SKBR3 cells for labeling. Electron beam damage was investigated by measuring the fluorescence intensities of GFP and the changes in cell area upon electron irradiation.

Control experiments were performed to distinguish various effects from electron beam exposure. Autofluorescence is an intrinsic fluorescence property of cells.[180] Among others, cellular compounds such as NAD(P)H, aromatic amino acids, lipopigments and flavins are capable of autofluorescence in a wide range of wavelengths.[180] Of the many autofluorescent compounds, the fluorescence of falvins is close to the fluorescence of GFP (ex.: 360 nm and 450 nm; em.: 520 nm).[180,182,183] Furthermore,

aldehyde fixatives such as PFA and GA can exhibit autofluorescence.[179] However, PFA, which was used as a fixative here, previously showed low autofluorescence similar to buffer solutions.[184] The control experiments confirmed that autofluorescence, from PFA or from cellular components, did not contribute to the fluorescence of the cells if exposed under fluorescence microscopy (**Figure 5.2**). Mean grey values were close to background level for unlabeled cells while mean grey values for GFP expressing SKBR3 cells were 60x higher. RFI of unlabeled SKBR3 cells did not increase over time, demonstrating that autofluorescence did not increase upon light exposure. However, unlabeled cells showed increased RFI upon drying and upon electron beam exposure (**Figure 5.3** and **Figure 5.5**). This may be due to increasing autofluorescence of the PFA fixative or cellular components. It has already been reported that the luminescence of aldehyde fixatives increases with increasing electron dose.[181] Control experiments with dried cells were performed to confirm the liquid state of the cells during the radiation experiments. It was observed that RFI of unlabeled cells increased upon drying (**Figure 5.3**). Consequently, if RFI in SKBR3 increased cells during electron beam irradiation, there were two possible explanations: Autofluorescence increased due to electron beam exposure or due to drying.

Labeled SKBR3 cells were exposed to ESEM and TEM conditions without electron beam irradiation. RFI decreased when exposed to ESEM conditions, but remained stable around 80 % when exposed to TEM (**Figure 5.4a**). As mentioned in **Chapter 4**, chamber pressure variations in ESEM can cause varying RFI. In TEM, however, the SiN liquid cell provides a sealed, atmospheric pressure environment resulting in natural pressure conditions for SKBR3 cells and stable RFI.[38,39]

5.2.1 Liquid-Phase Transmission Electron Microscopy

As for surface-bound GFP, RFI for GFP expressing and exposed cells in liquid-phase TEM decreased and $D_c < 0.1\,e^-/Å^2$ for most electron fluxes (**Figure 5.7**). Explanations for the degradation of fluorescence are similar to those mentioned in **Chapter 4** for surface-bound GFP: structural damage of the protein, protein detachment and changing liquid environment caused by electron beam exposure. However, actin-bound GFP in SKBR3 cells showed one order of magnitude higher

dose tolerance compared to surface-bound GFP. This may be due to the location of GFP inside cells, where it is protected by cellular components such as the plasma membrane. These components might be damaged at lower electron doses, presumably comparable to surface-bound GFP. The dose tolerance for SKBR3 cells in LP-EM were around three orders of magnitude lower than previous studies of whole cells in cryo-EM ($50 - 200\,e^-/Å^2$).[178,185]
After RFI decreased, it increased again for exposed cells as shown in **Figures 5.7** and **5.8**. This could be caused by the following factors:

- **Dry cells**. In the DIC images after opening the SiN liquid cell and placing the sample back in PBS (**Figure 5.6m**), SKBR3 cells, or the SiN membrane, appear to repel liquid after electron beam exposure. The control experiment of dry SKBR3 cells reveals that autofluorescence increased if samples were dry (**Figure 5.3**). The repellency might indicate, that cells were dry after a certain electron dose and hence, autofluorescence of all SKBR3 cells in TEM increased. Unexposed cells still showed increased RFI but less compared to exposed cells.

  Fabricated microchip surfaces are generally hydrophobic and more hydrophilic surfaces can be achieved by plasma treatment which removes hydrophobic hydrocarbon contaminations.[38,41,186] Hydrocarbons were shown to cause hydrophobicity e.g. in rare earth oxide ceramics.[187] To keep SiN membranes hydrophilic for a longer period of time, and to improved cell attachment, microchips were coated with PLL.[38,39] However, hydrocarbons can redeposit on the surface during electron beam irradiation.[70] In the past, hydrocarbon contaminations were more problematic because electron microscopes were operated at lower vacuum. Nowadays, the higher vacuum in the microscopes reduces hydrocarbons in the microscope originating from e.g. pump oils or vacuum grease.[70] However, specimens themselves can be a source of hydrocarbons so that complete elimination of hydrocarbon contaminations has not yet been achieved.[70]

  Most probably, hydrocarbons originated from the cells and resulted in hydrocarbon deposition on the surface in the experiments presented here. This increased hydrophobicity of the surface and caused dewetting. As a result,

cells dried after a certain electron dose and the autofluorescence signal increased. Other causes of dewetting behavior after electron beam irradiation were previously demonstrated on metallic nanoparticles on non- and semiconducting surfaces, hydrogen titanate nanowires, and ZnO powder under low energy irradiation.[188–190] Dewetting of metallic nanoparticles was mainly associated with mobile charges in the nanoparticles that are trapped at the interface between the nonconducting surface and the nanoparticles.[188] In hydrogen titanate nanowires, hydrophobicity was associated with the removal of hydroxyl groups upon electron beam irradiation.[189] Investigation of hydrophobicity of hydroxyapatite films showed disruption of the polarity of OH ions resulting in dewetting behavior with increasing electron dose.[191]

- **Cathodoluminescence**. During electron beam irradiation, some substances may exhibit cathodoluminescence, which has previously been shown for air-dried GFP.[175,176] Photoluminescence was shown to decrease upon irradiation while cathodoluminescence increased in these studies. However, simultaneous illumination of light and electron beam is required for the detection of cathodoluminescence.[37] Therefore, special cathodoluminescence microscopes, or electron microscopes equipped with spectrometers or in-built fluorescence microscopes are necessary.[32] Additionally, increasing RFI was not observed for surface-bound GFP (see **Chapter 4**), suggesting that increasing fluorescence is due to cellular or PFA autofluorescence rather than GFP itself.

In **Chapter 4** it was shown, that the use of GLCs increased the dose tolerance of GFP compared to SiN liquid cells. SKBR3 cells could also be seeded on graphene grids and enclosed in GLCs to mitigate beam damage. However, TEM grids used in this study are fragile and bend easily during handling which potentially causes leaking of the GLCs. An experimental setup is required which prevents bending and folding of the grids. In addition, graphene could potentially increase hydrophobicity. Incomplete wetting of graphene-coated SiN microchips due to hydrophobicity has been shown previously.[44]

The area changed for all exposed cells in TEM. For unexposed cells, the area remained stable over the electron dose. Changes in area can be caused by shrinkage of the cells. The fact that only exposed cells show decreasing area indicates, that

these cells shrink more. Together with the liquid repellency of exposed cells this strengthens the argument that cells were dry.
Unexposed SKBR3 cells with actin-bound GFP showed less decrease in RFI compared to unexposed surface-bound GFP. SE created in the liquid cell still propagate through the liquid and cause damage. However, GFP was bound to actin filaments inside the cells. The plasma membrane presumably protected GFP from damage caused by SE.

5.2.2 Environmental Scanning Electron Microscopy

In ESEM, GFP expressing SKBR3 cells exposed with a flux of $10\,e^-/Å^2s$ showed increasing RFI but other fluxes showed decreasing RFI over the electron dose (**Figure 5.12**). In addition, SiN membranes were still wetting after electron beam exposure (**Figure 5.11m-o**). As mentioned in **Chapter 4**, the liquid thickness in ESEM could not be determined quantitatively and varied between samples. Therefore, the electron beam may not fully encounter the sample, which would keep the SiN membrane more hydrophilic. Cells would be wet and less autofluorescence would occur. In addition, positive ions in the gas environment of ESEM neutralize charge and mitigate charging effects (see **Section 2.1.2**).[29,47]
RFI of unexposed cells decreased below 1/e for all electron fluxes in ESEM (**Figure 5.13**). This decrease can as well be caused by the exposure to ESEM conditions as shown in the control experiments (**Figure 5.4**). RFI did not increase in unexposed cells, supporting the argument that SiN microchips were still wetting after electron beam exposure (**Figure 5.13**). The area for all cells in ESEM remained stable. This indicates, that cells were still hydrated and liquid did not evaporate in vacuum. For an electron flux of $10\,e^-/Å^2s$, the area decreased over increasing electron dose. Together with the fact that RFI increased in this sample, there might have been more drying in this sample although samples still appeared hydrated in ESEM as well as under fluorescence microscopy. Another option is that the electron dose tolerance was dependent on the electron flux.

It has been reported that cells are stable up to an electron dose of $0.01\,e^-/Å^2$.[20] In the experiments shown here, the electron dose threshold was one order of magnitude

higher ($0.1\,e^-/Å^2$). However, GFP bound to actin filaments inside the cells and protected from the electron beam by surrounding proteins, i.e. the plasma membrane, was investigated here. Proteins in the plasma membrane could be damaged before GFP. It has been reported previously that 50 % of bacteria showed damage in the cytoplasm at an electron dose of $0.1\,e^-/Å^2$ while the plasma membranes remained intact.[192] Moreover, the absence of other functions such as reproducibility and enzyme function was observed at this electron dose.[192] Enzyme inactivation was observed at electron doses around $0.01\,e^-/Å^2$.[193]
Another aspect that must be considered for cells in SiN liquid cells is the compression between the two microchips. Bacterial damage from compression has been reported previously.[192] In the study presented in this thesis, spacers of 5 µm were used per microchip, resulting in 10 µm spacer thickness. However, SKBR3 cells can be thicker than 10 µm and this would cause compression to be a damaging factor.[194] In addition, 10 µm thickness will result in low electron transmission. Therefore, the use of this setup for further investigations of cells in LP-EM should be addressed in future studies.

5.3 Conclusion

In this chapter, electron beam damage of GFP labeled SKBR3 cells was investigated in LP-EM. The following conclusions can be drawn:

1. $D_c < 0.1\,e^-/Å^2$ for some electron fluxes in TEM before RFI increased. This dose tolerance was one order of magnitude higher compared to surface-bound GFP (see **Chapter 4**).

2. $D_c < 0.1\,e^-/Å^2$ in ESEM which was consistent with experiments in **Chapter 4**.

3. The dose tolerance for GFP in SKBR3 cells in LP-EM was three orders of magnitude lower than previously described for whole cells in cryo-EM.[178,185]

4. After the decrease, RFI increased again. This was associated with dried cells resulting from increased hydrophobicity and dewetting upon electron beam irradiation.

5. The area of SKBR3 cells remained stable in ESEM. In TEM, all exposed cells showed decreasing area and unexposed cells showed stable area, possibly due to dewetting and drying in TEM.

6 Graphene Enclosure of Chemically Fixed Mammalian Cells for Liquid-Phase Electron Microscopy

Parts of this chapter were published in Blach, P.; Keskin, S. & de Jonge, N. Graphene Enclosure of Chemically Fixed Mammalian Cells for Liquid-Phase Electron Microscopy Journal of Visualized Experiments, MyJove Corporation, 2020 DOI: 10.3791/61458[154]

Analysis of membrane protein function is essential for cell biological research, and for drug development. A class of important experiments involves the examination of membrane protein positions in cells. This information can be used to deduce conclusions about the assembly of proteins in protein complexes and their specific locations in the plasma membrane, which, via dynamic assembly and disassembly, drives a wide variety of cellular functions. Among other techniques, light microscopy (LM) and EM are used to study protein functions in cells. LM allows the analysis of whole cells in liquid; however, the resolution is restricted to 200 - 300 nm for conventional and up to 20 nm for super resolution fluorescence microscopy under practical conditions.[195,196] EM provides around 1 Å resolutions,[8] but conventional sample preparation requires dehydration, metal staining to enhance image contrast, and embedding in a mounting substance, such as resin, for TEM.[2] To preserve biological samples in a more native-like environment, cryo-EM techniques can be used.[197,198] The samples are rapidly frozen into amorphous ice, and, if needed, sectioned. Another option is freeze-fracturing EM.[199] EM techniques for studying membrane proteins within intact cells in their native, liquid state have emerged in the past decade.[200–203] A spatial resolution of 2 nm was achieved on QDs labeled membrane proteins in whole cells grown on a SiN membrane and enclosed by a layer of graphene.[201]

Here, details of a protocol for protein labeling and graphene coating are described.[45,201] The goal of this protocol is to analyze the spatial distribution of HER2 in the membrane of whole, fixed cells, while preserving the cells in a hydrated state. Coating with graphene prevents drying of the cells in vacuum, and

also reduces radiation damage.[44] This method provides information about labeled membrane proteins within the intact plasma membrane, but the method is not useful for studying cellular ultrastructure as is usually done with EM.
Graphene is the thinnest nanomaterial known, and consists of a single carbon atom thick crystalline sheet arranged in a honeycomb lattice.[85] It has unique properties including high flexibility and mechanical strength. Recent research has shown that defect-free graphene is impermeable to gases and liquids, but defects allow hydrogen permeation.[101] This leakage can be reduced by using multilayer graphene as used a support for cryo-EM samples, improving the homogeneity of the thin ice layer compared to graphene oxide, where only nonuniform layers can be formed.[204] Graphene was also shown to reduce beam damage of biological samples during liquid-phase transmission electron microscopy.[26,44] As an exemplary experiment, HER2 expressed in the mammalian breast cancer cell line SKBR3 was labeled with QDs[205] and its spatial distribution recorded using STEM. Cells were seeded on a Si microchip with an electron transparent SiN membrane.[38] The microchips were chosen as a support as they are robust, compatible with LM and EM, and the entire labeling procedure can be performed directly on the microchip.[38] After cell attachment, HER2 was labeled with a two-step protocol.[206] First, a biotinylated anti-HER2 antibody mimetic compound[207] was attached to HER2. The cells were then chemically fixed to prevent label-induced receptor clustering. Streptavidin-coated QDs were subsequently linked to the HER2-antibody mimetic complex. The bright fluorescence signal and the electron-dense core of the QDs allowed correlative fluorescence- and electron microscopy (CLEM).[206] CLEM is especially useful because cellular regions of interest for STEM analysis can be selected from the overview fluorescence microscopy images highlighting the localization of HER2 on the cells. Cells were analyzed by fluorescence microscopy to identify cellular regions with high HER2 levels. Thereafter, a 3-5 layer thick sheet of graphene was transferred onto the cells for coating.[201,208] Subsequently, the sample was mounted in an EM specimen holder. STEM data was acquired using the ADF detector, providing information about the spatial distribution of HER2 on the cell surface location, but giving no information about the ultrastructure of the cell. To determine the stability of the sample under electron beam irradiation, the samples were examined at increasing dose (D) in an image series. The difference between graphene-coated

and non-coated samples was investigated. Several kinds of radiation damage were evaluated.

6.1 Results

Representative STEM data is shown in **Figure 6.1**. Graphene-coated (left column) and non-coated (right column) SKBR3 cells were investigated. **Figure 6.1A** and **Figure 6.1B** show $M = 800$x overview images of the cells on the window. The areas shown as insets were imaged at $M = 80{,}000$x during the dose series, see **Figure 6.1C** and **Figure 6.1D**. The QDs are visible as bright spots here. **Figure 6.1E** and **Figure 6.1F** show $M = 50{,}000$x magnified images acquired at the locations of the rectangles in **Figure 6.1C** and **Figure 6.1D**. Both images were recorded after the acquisition of a dose series with $D = (7.8 \pm 0.4) \cdot 10^3\,\mathrm{e}^-/\mathrm{Å}^2$. The dose series was recorded at $M = 80{,}000$x. The exposed areas can be recognized as rectangles, whereby the rectangle is clearest visible for the non-coated sample (**Figure 6.1F**). To verify the presence of graphene, diffraction patterns of areas without cells, but with or without graphene on the SiN window were acquired. The hexagonal structure of the graphene was observed in the diffraction pattern of the graphene-coated sample (**Figure 6.1G**), while it was absent for the non-coated sample (**Figure 6.1H**). The diffraction pattern of single crystal graphene will have six-fold symmetry due to highly ordered hexagonal structure of graphene. So, the hexagonal structure indicates the presence of graphene on the samples.

To investigate the effect of electron beam illumination on the sample, STEM images were acquired in an image series with an accumulating electron dose. Representative results for non-coated and graphene-coated samples are shown in **Figure 6.2A - D** and **Figure 6.2E - G**, respectively. All data was acquired at the edge of the cell, where the cell is the flattest, and the observed structure is thus the closest to the SiN membrane. The exposure of a non-coated samples led to bright structures appearing on the cell surfaces at $D = (1.9 \pm 0.1) \cdot 10^3\,\mathrm{e}^-/\mathrm{Å}^2$ (**Figure 6.2B**). These structures became larger with higher doses, so they were clearly visible in the last image of the series at $D = (7.8 \pm 0.4) \cdot 10^3\,\mathrm{e}^-/\mathrm{Å}^2$ (**Figure 6.2C** and **D**). These spots did not appear on any of the graphene-coated samples (**Figure 6.2E - G**).

Six coated and seven non-coated samples were investigated in total. Two out

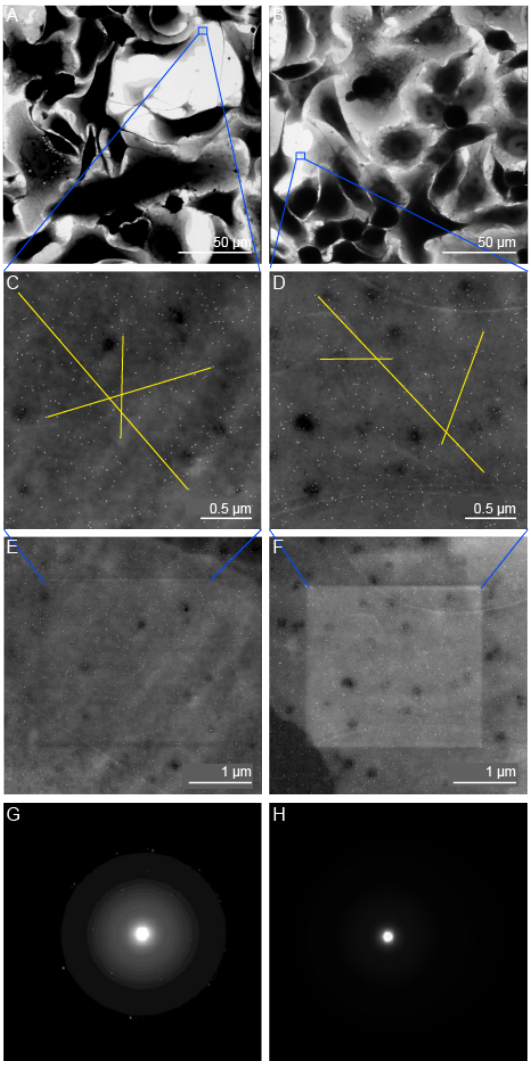

Figure 6.1: Scanning transmission electron microscopy (STEM) of graphene coated and non-coated SKBR3 cells on silicon nitrite (SiN) window. (**A**) STEM of a graphene coated sample acquired at $M = 800$x. (**B**) STEM image of a non-coated sample acquired at $M = 800$x. (**C**) $M = 80{,}000$x image recorded at the position of the blue rectangle in A. Yellow lines represents examples distances measured within particle. (**D**) $M = 80{,}000$x image recorded at the position of the blue rectangle in B. Yellow line represents examples distances measured within particles. (**E**) $M = 50{,}000$x image of the same region as C exposed to $D = (7.8 \pm 0.4) \cdot 10^3\,\mathrm{e}^-/\mathrm{Å}^2$. (**F**) $M = 50{,}000$x image of the same region as D and exposed to $D = (7.8 \pm 0.4) \cdot 10^3\,\mathrm{e}^-/\mathrm{Å}^2$. The exposed areas were clearly seen. (**G**) Diffraction pattern of a graphene-coated sample from an area without cells. The six-fold symmetry of the graphene is visible as bright spots. (**H**) Diffraction pattern of a sample without graphene showing no 6-fold bright spots. This is adapted from .[154]

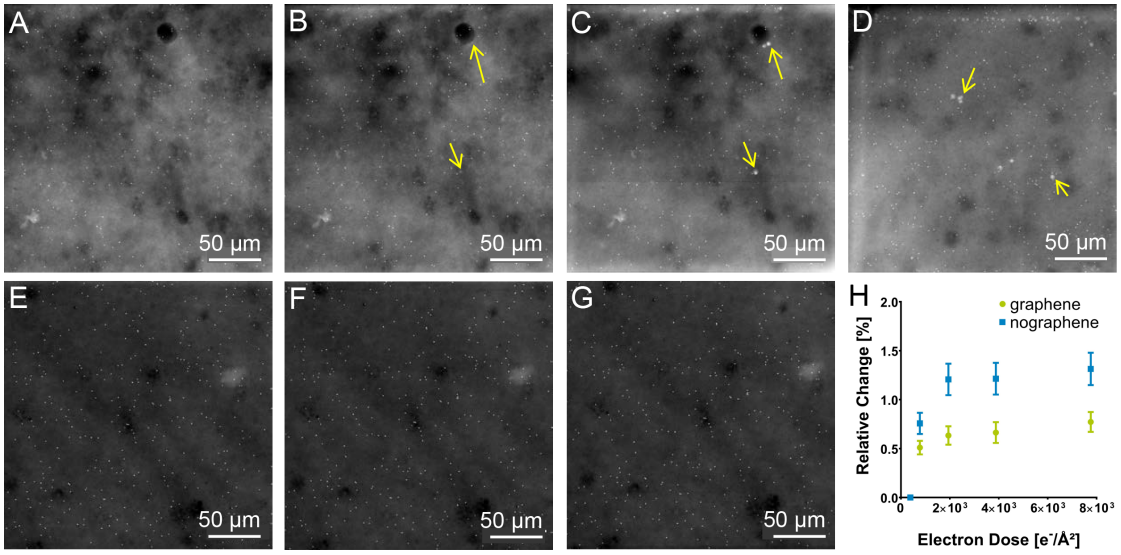

Figure 6.2: Artifacts arising on samples without graphene coating. (**A**) First images of regions on samples without graphene coating acquired at $M = 80{,}000$x, and exposed to $D = (0.39 \pm 0.02) \cdot 10^2\,\mathrm{e}^-/\mathrm{Å}^2$. (**B**) Images with the first artifacts arising at $D = (1.94 \pm 0.1) \cdot 10^3\,\mathrm{e}^-/\mathrm{Å}^2$ (yellow arrows). (**C,D**) Last image of the series acquired with $\mathrm{D} = (7.8 \pm 0.4) \cdot 10^3\,\mathrm{e}^-/\mathrm{Å}^2$. Artifacts are visible as bright spots. (**E-G**) Graphene coated samples without arising artifacts. (**E**) $D = (0.39 \pm 0.02) \cdot 10^2\,\mathrm{e}^-/\mathrm{Å}^2$ (**F**) $D = (1.94 \pm 0.1) \cdot 10^3\,\mathrm{e}^-/\mathrm{Å}^2$ (**G**) $D = (7.8 \pm 0.4) \cdot 10^3\,\mathrm{e}^-/\mathrm{Å}^2$. (**H**) Relative change in particle distances for graphene coated and non-coated samples. Two of the non-coated samples showing artifacts, one of which shown in (A-C), and the last image of the second sample in D, as well as three coated samples were analyzed (one is shown in E-G). In total, ten quantum dot (QD) pairs were examined per sample with distances ranging between 250 nm and 3 µm. The relative change reflects the average of all measurements in one group. This is adapted from .[154]

of seven non-coated samples showed these artifacts. None of the coated samples showed any additional bright spots. As another measure of radiation damage, the distance between QDs was examined. If structural damage were to occur, one would expect distances between QDs to change. Changes in distances were measured for different pairs of QDs with accumulating D for a range of pair distances. **Figure 6.2H** shows that the relative change of the particles for non-coated samples stayed below 1.3 % on average, while the average relative distance remained below 0.8 % for the coated samples. One can, therefore, conclude that the graphene coating stabilized the sample but the dried-in samples without graphene coating were also remarkably stable.

6.2 Discussion

To better understand protein function, it is important to obtain information about protein locations in the plasma membrane of intact cells. Methods for obtaining this information include super-resolution fluorescence microscopy.[195,196] Although super-resolution microscopy has further developed over the past years, its resolution is still limited to about 20 nm for practical conditions of cell experiments, while typical receptor proteins have sizes in the range of 1-10 nm. The imaging of proteins on single cell and single molecule level with sufficient resolution to visualize proteins is possible with EM. But due to sectioning, conventional EM methods typically do not leave the cell intact,[27] which leads to the loss of important information about the context and the spatial distribution of proteins in the plasma membrane. Methods for whole cells with cryo-TEM have been developed,[198] it is feasible to combine protein labeling with cryo-EM,[209] also cryo-STEM has been demonstrated.[210] However, cryo-EM workflows are optimized for studying the cellular ultrastructure and protein structure, and not so much for analyzing membrane protein spatial distributions. Critical point drying is another whole cell preparation method but the samples are subjected to several drying steps, and the technique is highly time-consuming.[211] Membrane proteins have also been examined via freeze fracture.[199] In this method, cells are fixed, frozen, and fractured. The fractured parts are replicated by carbon and platinum layers, and the biological sample is removed. The replicas can then be analyzed with EM.[212] Whole cell analysis is impossible with freeze fraction, because information about the distribution of proteins in the membrane within context of the whole cell is lost.

The method presented here allows the cell membrane to be studied without needing to thin-slice the specimen.[201,213] The cells are kept intact so that the localization of the membrane proteins is visible from the fluorescence images, which are correlated with the EM images. Studying proteins at the single cell and single molecule level within intact cells in hydrated state has shown to be possible with a resolution of 2 nm using STEM of QD labeled proteins using this graphene enclosure method.[201] Keeping cells in their native state is crucial, as it preserves the spatial distribution of membrane proteins such that analyses are possible at the single cell and single molecule level, which is important for understanding protein functions, and devel-

oping new drugs for therapy approaches.
Another critical aspect of imaging biological samples with EM is the radiation damage of the samples caused by the electron beam. Solutions often include the reduction of the electron dose as much as possible or various coating methods, such as encapsulating the specimen between thin layers of carbon.[74] Our method shows that graphene coating reduces beam-induced artifacts that emerge on the cell surface for non-coated samples. Examination of the chemically fixed, and graphene coated biological samples is possible under electron beam irradiation at 200 kV beam energy up to $D = (7.8 \pm 0.4) \cdot 10^3\,\mathrm{e}^-/\mathrm{Å}^2$ without radiation damage, such as bright spots, appearing on the sample.
Graphene coating prevented artifacts from appearing on the sample. But for $D < 4 \cdot 10^2\,\mathrm{e}^-/\mathrm{Å}^2$ also no artifacts emerged for the non-coated sample, and artifacts appeared for 2 non-coated samples only. Thus, examinations of non-coated cells also seem possible, although it would be better to use graphene and avoid the risk of artifact formation. The composition of those artifacts can be analyzed in the future to give hints about how to prevent their formation. Regarding the structural stability of the cells only a minor improvement of the graphene coating was observed. The fixed cells were apparently stabilized in the examined thin areas, where their structure was in close proximity of the SiN membrane. What we did not examine here, however, were drying artifacts that are known to occur for cellular samples when exposed to vacuum.[2] Drying of the cells would lead to shrinkage of the cells so that also the QD distances would change as a consequence. For the electron dose used here, the distance of QDs of graphene-coated and non-coated samples remained stable. Further studies are needed to examine the effect of graphene coating on the cells for EM.
One limitation of this method is that the chemical fixation of the cells is necessary; therefore, no life cell experiments can be performed. But in case the labeling is not needed and cells with a higher structural stability are used, for example bacteria, then unfixed cells can be enclosed in graphene for EM[214] albeit with a different electron dose tolerance. Also, the proteins are not directly detectable, so QDs are needed to visualize the proteins. The method would benefit from smaller labels. A point of discussion is whether it is good or bad that the ultrastructure is not clearly visible. Our method is similar to that of fluorescence microscopy where only se-

lected proteins are visible.[215] Increasing the visibility of the ultrastructure would also add much more information to the image, and then at some point prevent detection of the individual label positions. Furthermore, the method described here is for one protein species, and additions of the protocol are needed to be able to label multiple proteins. Last, the method works when a small high affinity specifically binding molecule such as antibody mimetic[207] or nanobody[216] is available. Commonly used antibodies are much larger and would prevent the detection of the functional state of the protein subunits into oligomers.

Our method is useful for studying protein function on whole cells using EM while keeping the cells in hydrated state. It is readily possible to examine series of cells. Other type of cells and proteins can be studied as well. If protein labeling is not needed, a subset of the protocol can be used for graphene coating of wide variety of biological specimens. The ability to study whole cells is relevant in cellular research for understanding correlations of membrane protein function at the molecular level.

7 Conclusion and Outlook

Observation of native biological materials in conventional EM is usually hindered by sample preparation procedures such as dehydration, freezing, staining, and sectioning. In addition, the electron beam can cause damage, such as bond rupture, which in particular complicates the examination of radiation-sensitive materials such as biological samples. LP-EM allows the observation of biological materials in liquid environments without conventional sample preparation procedures. However, electron beam damage also occurs in LP-EM, and can result in loss of information about the samples. Electron dose thresholds for biological samples in LP-EM are not yet fully explored.

In this thesis, the electron dose tolerance of biological samples in LP-EM was investigated. GFP was used as a model protein and studied in SiN liquid cells and in GLCs. In addition, GFP was bound to actin filaments in fixed SKBR3 cells to determine the dose tolerance in more complex systems. In fixed SKBR3 cells, radiation damage was also analyzed by the displacement of QD-labeled membrane receptor HER2. Here, the difference between graphene coated and non-coated samples was analyzed.

The first approach was to study the electron dose tolerance of GFP in LP-EM. GFP was either bound to SiN surfaces and studied in SiN liquid cells or encapsulated in GLCs. Samples were exposed in TEM and ESEM with electron doses ranging from 0.001 - 100 $e^-/Å^2$ and electron fluxes ranging from 0.001 - 10 $e^-/Å^2s$. For GFP in SiN liquid cells $D_c < 0.01\,e^-/Å^2$ in TEM. To investigate whether electron beam damage can be mitigated, graphene was used as a sample support instead of SiN. GFP was encapsulated in GLCs and exposed with the same electron doses and fluxes in TEM. The dose tolerance could be increased to $D_c < 10\,e^-/Å^2$. This was mainly associated with the radical scavenging property of graphene. However, the setup of GLC experiments could also contribute to the large increase in dose tolerance compared to SiN. The liquid thickness in GLCs with GFP was 380 ± 110 nm which possibly caused beam spreading when the electron beam encountered the specimen, so that the specimen was not fully exposed. Additionally, electron beam exposure and bulging can cause protein detachment in SiN liquid cells which may artificially decrease the fluorescence intensity. Therefore, the actual electron dose

tolerance of GFP in GLCs might be lower, and the dose tolerance of surface-bound GFP in SiN liquid cells might be higher. GFP encapsulated in GLCs was studied at a beam energy of 30 kV in TEM to find an indication for the damage mechanism. From theory it is well known that damage caused by elastic scattering increases with lower beam energy. No significant difference in the electron dose tolerance of GFP at beam energies of 30 kV and 200 kV could be observed. This indicated that damage caused by elastic scattering did not have a major impact on these samples. Surface-bound GFP exposed in ESEM showed one order of magnitude higher dose tolerance compared to TEM ($D_c < 0.1\,\mathrm{e}^-/\mathrm{Å}^2$). The higher dose tolerance was mainly associated with the experimental setup in ESEM. Beam spreading can be caused by irregular liquid thickness and scattering of the primary electron beam at gas molecules. This possibly decreased the electron dose that encountered the specimen. A controlled liquid system could be beneficial in ESEM to ensure that the specimen was fully exposed.

GFP bound to actin filaments in SKBR3 cells showed one order of magnitude higher electron dose tolerance compared to surface-bound GFP in SiN liquid cells when exposed in TEM ($D_c < 0.1\,\mathrm{e}^-/\mathrm{Å}^2$). In ESEM, $D_c < 0.1\,\mathrm{e}^-/\mathrm{Å}^2$ which was consistent with the electron dose thresholds of surface-bound GFP. However, RFI of samples exposed in TEM increased when the electron dose increased above D_c. Fluorescence increase was associated with dewetting behavior which was also observed under fluorescence microscopy. One explanation for dewetting was increased hydrophobicity upon electron beam irradiation due to hydrocarbon contaminations. Another indication of dry cells upon electron beam irradiation was decreasing area of all exposed SKBR3 cells in TEM, whereas the area of unexposed cells remained stable. In ESEM, RFI did not increase for most electron fluxes. This indicated that the samples remained hydrated in ESEM. In addition, large spacers (10 µm) were used for liquid cell preparation in TEM to minimize compression of SKBR3 cells. However, the high thickness resulted in lower electron transmission and uncertainties in the effective electron dose. Due to dewetting and the high liquid thickness, the liquid cell system in TEM requires improvement or other systems must be used to study whole cells in LP-EM. For example, since cells appear to remain hydrated in ESEM, this method would be well suited to image whole cells if a controlled liquid system could be established.

GFP bound to actin filaments showed higher dose tolerance compared to surface-bound GFP in TEM. However, the protein was protected inside the cells by other cellular components such as the plasma membrane. Although the fluorescence of GFP was preserved, the proteins in the plasma membrane could be damaged at lower electron dose. The electron deposition per unit area per unit time, i.e., electron flux, did not affect the electron dose tolerance of GFP, either for surface-bound or actin-bound GFP.
Radiation damage was also investigated by analyzing the displacement of the membrane receptor HER2. HER2 was labeled with QDs on fixed SKBR3 cells. Graphene coated and non-coated samples were studied. At $D = (7.8 \pm 0.4) \cdot 10^3\,\mathrm{e^-/Å^2}$ the displacement of coated samples was below 0.8 %. Non-coated samples remained stable with a relative change of 1.3 %. However, samples formed artifacts in the form of bright spots on some uncoated samples. The electron doses used in this study were quite high compared to the dose tolerances for surface-bound and actin-bound GFP. Imaging of QD labels was possible, and SKBR3 cells appeared to be stable in this environment; however, proteins were likely damaged at such high electron doses.

This thesis provides information about the electron dose thresholds of biological specimens in LP-EM. However, further investigations on the nature of electron beam damage can be performed in the future. For example, photoconversion of GFP has been reported previously.[122,175,217] This would result in a decrease in intensity at the natural emission wavelength, but an increase in intensity at other wavelengths. To investigate whether photoconversion also occurs after electron beam exposure, structural changes in the chromophore of GFP could be assessed using NMR spectroscopy.[218] However, an experimental setup is required to detach the exposed proteins from the SiN surface after electron beam irradiation without changing their structure.
A pressure control system as reported previously is required to reduce bulging and the possible accompanying protein detachment.[40] A pressure control system is also required in ESEM to ensure comparable liquid thickness for all samples. In addition, results can be compared more reliably to TEM if a controlled liquid system is

present.
Further damage mitigation can be achieved by reducing the electron dose in EM. Methods such as sparse imaging and electron beam image shift can be used.[83] Another option for mitigating radiation damage is reduction of the beam energy. No significant difference was found between 30 kV and 200 kV for GLCs in the experiments presented in this thesis. However, it has previously been reported that radiation damage in graphene increased above 80 kV.[219] Below 80 kV, knock-on damage in graphene can be reduced.[20,112,219] Furthermore, ^{13}C graphene showed less damage than ^{12}C graphene which is usually used for graphene preparation. Substitution with ^{13}C graphene can further mitigate beam damage.[219]
To mitigate radiation damage in cells, they can be investigated in GLCs. If cells remain hydrated in GLCs, this could be a viable system for studying radiation damage in whole cells. The high flexibility of graphene could also decrease compression of cells. In SiN liquid cells, a constant flow in the liquid holder could increase the wettability of cells. In addition, constantly changing the liquid can contribute to a stable chemical environment and reduce radicals.

In summary, this thesis provides information about electron dose thresholds for biological materials such as proteins and fixed cells in liquid environment using LP-EM. The findings of this work provide a guideline for electron dose measurements in LP-EM. Damage mitigation was achieved by encapsulating proteins in GLCs. The reported electron dose tolerances for GFP and fixed cells can be applied to further studies of proteins and cells in LP-EM.

References

[1] Ernst Ruska. The development of the electron microscope and of electron microscopy (nobel lecture). *Angewandte Chemie International Edition in English*, 26(7):595–605, 1987.

[2] John Bozzola. *Electron microscopy : principles and techniques for biologists*. Jones and Bartlett, Sudbury, Mass, 1999.

[3] Max Knoll and Ernst Ruska. Das Elektronenmikroskop. *Zeitschrift für Physik*, 78(5-6):318–339, 1932.

[4] B. Borries, E. Ruska, and H. Ruska. Bakterien und Virus in übermikroskopischer Aufnahme. *Klinische Wochenschrift*, 17(27):921–925, 1938.

[5] Helmut Ruska, Bodo v Borries, and Ernst Ruska. Die Bedeutung der Übermikroskopie für die Virusforschung. *Archiv für die gesamte Virusforschung*, 1(1):155–169, 1939.

[6] F. Krause. Das magnetische Elektronenmikroskop und seine Anwendung in der Biologie. *Die Naturwissenschaften*, 25(51):817–825, 1937.

[7] R. D. Heidenreich. Electron microscope and diffraction study of metal crystal textures by means of thin sections. *Journal of Applied Physics*, 20(10):993–1010, 1949.

[8] David B. Williams and C. Barry Carter. *Transmission electron microscopy: a textbook for materials science*. New York ; London : Springer, 2nd edition, 2009. This ed. originally published: 2008.

[9] John W. Smith and Qian Chen. Liquid-phase electron microscopy imaging of cellular and biomolecular systems. *Journal of Materials Chemistry B*, 8(37):8490–8506, 2020.

[10] Y. Zhu and H. D. Espinosa. An electromechanical material testing system for in situ electron microscopy and applications. *Proceedings of the National Academy of Sciences*, 102(41):14503–14508, 2005.

[11] Niels de Jonge and Frances M. Ross. Electron microscopy of specimens in liquid. *Nature Nanotechnology*, 6(11):695–704, 2011.

[12] O. Scherzer. Über einige Fehler von Elektronenlinsen. *Zeitschrift für Physik*, 101(9-10):593–603, 1936.

[13] Albert Prebus and James Hillier. The construction of a magnetic electron microscope of high resolving power. *Canadian Journal of Research*, 17a(4):49–65, 1939.

[14] M. Haider et al. Current and future aberration correctors for the improvement of resolution in electron microscopy. *Philosophical Transactions of the Royal Society A: Mathematical, Physical and Engineering Sciences*, 367(1903):3665–3682, 2009.

[15] F. Hosokawa. A spherical aberration-corrected 200 kV TEM. *Journal of Electron Microscopy*, 52(1):3–10, 2003.

[16] M. Haider et al. Towards 0.1 nm resolution with the first spherically corrected transmission electron microscope. *Journal of Electron Microscopy*, 47(5):395–405, 1998.

[17] Rafal E. Dunin-Borkowski and Lothar Houben. Spherical and chromatic aberration correction for atomic-resolution liquid cell electron microscopy. In *Liquid Cell Electron Microscopy*, pages 434–455. Cambridge University Press, 2016.

[18] C. Kisielowski et al. Detection of single atoms and buried defects in three dimensions by aberration-corrected electron microscope with 0.5-Å information limit. *Microscopy and Microanalysis*, 14(5):469–477, 2008.

[19] E. Knapek and J. Dubochet. Beam damage to organic material is considerably reduced in cryo-electron microscopy. *Journal of Molecular Biology*, 141(2):147–161, 1980.

[20] Jungjae Park et al. Graphene liquid cell electron microscopy: Progress, applications, and perspectives. *ACS nano*, 15(1):288–308, 2021.

[21] Ludwig Reimer. *Scanning Electron Microscopy*. Springer Berlin Heidelberg, 2010.

[22] Xiao-chen Bai, Greg McMullan, and Sjors H.W Scheres. How cryo-EM is revolutionizing structural biology. *Trends in Biochemical Sciences*, 40(1):49–57, 2015.

[23] Audrey M. Glauert and Peter R. Lewis. *Biological Specimen Preparation for Transmission Electron Microscopy*. Princeton University Press, dec 1998.

[24] Hanglong Wu et al. Liquid-phase electron microscopy for soft matter science and biology. *Advanced Materials*, 32(25):2001582, 2020.

[25] Werner Villiger and Andreas Bremer. Ultramicrotomy of biological objects: From the beginning to the present. *Journal of Structural Biology*, 104(1-3):178–188, 1990.

[26] Sercan Keskin and Niels de Jonge. Reduced radiation damage in transmission electron microscopy of proteins in graphene liquid cells. *Nano Letters*, 18(12):7435–7440, 2018.

[27] Helmut Reimer, Ludwig; Kohl. *Transmission Electron Microscopy: Physics of Image Formation*. Springer New York, fifth edition, 2008.

[28] David Bell and Natasha Erdman. *Low Voltage Electron Microscopy: Principles and Applications*. Wiley, 2013.

[29] Ludwig Reimer. *Scanning electron microscopy : physics of image formation and microanalysis*. Springer-Verlag, Berlin New York, 1985.

[30] SJ Pennycook et al. Scanning transmission electron microscopy for nanostructure characterization. In *Scanning microscopy for nanotechnology*, pages 152–191. Springer, 2006.

[31] David A. Muller. Structure and bonding at the atomic scale by scanning transmission electron microscopy. *Nature Materials*, 8(4):263–270, 2009.

[32] Toon Coenen and otheres. Cathodoluminescence microscopy: Optical imaging and spectroscopy with deep-subwavelength resolution. *MRS Bulletin*, 40(4):359–365, 2015.

[33] R. F. Egerton. *Physical Principles of Electron Microscopy: An Introduction to TEM, SEM, and AEM*. Springer Nature, 2011.

[34] K. Murata. Depth resolution of the low- and high-deflection backscattered electron images in the scanning electron microscope. *Physica Status Solidi (a)*, 36(2):527–532, 1976.

[35] Diana B. Peckys, Elena Macías-Sánchez, and Niels de Jonge. Liquid phase electron microscopy of biological specimens. *MRS Bulletin*, 45(9):754–760, 2020.

[36] Frances M Ross. Opportunities and challenges in liquid cell electron microscopy. *Science*, 350(6267), 2015.

[37] Frances M. Ross, editor. *Liquid Cell Electron Microscopy*. Cambridge University Press, nov 2016.

[38] E. A. Ring et al. Silicon nitride windows for electron microscopy of whole cells. *Journal of Microscopy*, 243(3):273–283, 2011.

[39] Elisabeth A. Ring and Niels de Jonge. Microfluidic system for transmission electron microscopy. *Microscopy and Microanalysis*, 16(5):622–629, 2010.

[40] Sercan Keskin, Peter Kunnas, and Niels de Jonge. Liquid-phase electron microscopy with controllable liquid thickness. *Nano Letters*, 19(7):4608–4613, 2019.

[41] Taylor J. Woehl et al. Experimental procedures to mitigate electron beam induced artifacts during in situ fluid imaging of nanomaterials. *Ultramicroscopy*, 127:53–63, 2013.

[42] Christopher J Russo and Lori A Passmore. Progress towards an optimal specimen support for electron cryomicroscopy. *Current Opinion in Structural Biology*, 37:81–89, 2016.

[43] Christopher J Russo and Lori A Passmore. Controlling protein adsorption on graphene for cryo-EM using low-energy hydrogen plasmas. *Nature Methods*, 11(6):649–652, 2014.

[44] Hoduk Cho et al. The use of graphene and its derivatives for liquid-phase transmission electron microscopy of radiation-sensitive specimens. *Nano Letters*, 17(1):414–420, 2016.

[45] Matthew R. Hauwiller, Justin C. Ondry, and A. Paul Alivisatos. Using graphene liquid cell transmission electron microscopy to study in situ nanocrystal etching. *Journal of Visualized Experiments*, (135), 2018.

[46] Pauline M. G. van Deursen et al. Graphene liquid cells assembled through loop-assisted transfer method and located with correlated light-electron microscopy. *Advanced Functional Materials*, 30(11):1904468, 2020.

[47] S.E. Kirk, J.N. Skeeper, and A.M. Donald. Application of environmental scanning electron microscopy to determine biological surface structure. *Journal of Microscopy*, 233(2):205–224, 2009.

[48] D.J. Stokes. Environmental scanning electron microscopy (ESEM): principles and applications to food microstructures. In *Food Microstructures*, pages 3–26. Elsevier, 2013.

[49] Athene M Donald. Environmental scanning electron microscopy for the study of 'wet' systems. *Current Opinion in Colloid & Interface Science*, 3(2):143–147, 1998.

[50] G.D. Danilatos. Foundations of environmental scanning electron microscopy. In *Advances in Electronics and Electron Physics Volume 71*, pages 109–250. Elsevier, 1988.

[51] Debbie J. Stokes. Recent advances in electron imaging, image interpretation and applications: environmental scanning electron microscopy. *Philosophical Transactions of the Royal Society of London. Series A: Mathematical, Physical and Engineering Sciences*, 361(1813):2771–2787, 2003.

[52] Scott P. Collins et al. Advantages of environmental scanning electron microscopy in studies of microorganisms. *Microscopy Research and Technique*, 25(5-6):398–405, 1993.

[53] Stefan W. Hell and Jan Wichmann. Breaking the diffraction resolution limit by stimulated emission: stimulated-emission-depletion fluorescence microscopy. *Optics Letters*, 19(11):780, 1994.

[54] Michael Weber et al. MINSTED fluorescence localization and nanoscopy. *Nature Photonics*, 15(5):361–366, 2021.

[55] Michael J Rust, Mark Bates, and Xiaowei Zhuang. Sub-diffraction-limit imaging by stochastic optical reconstruction microscopy (STORM). *Nature Methods*, 3(10):793–796, 2006.

[56] Bonnie O. Leung and Keng C. Chou. Review of super-resolution fluorescence microscopy for biology. *Applied Spectroscopy*, 65(9):967–980, 2011.

[57] Megan J. Dobro et al. Plunge freezing for electron cryomicroscopy. In *Methods in Enzymology*, pages 63–82. Elsevier, 2010.

[58] Kazuyoshi Murata and Matthias Wolf. Cryo-electron microscopy for structural analysis of dynamic biological macromolecules. *Biochimica et Biophysica Acta (BBA) - General Subjects*, 1862(2):324–334, 2018.

[59] Lesley A Earl et al. Cryo-EM: Beyond the microscope. *Current Opinion in Structural Biology*, 46:71–78, 2017.

[60] Mark A. Herzik Jr. Cryo-electron microscopy reaches atomic resolution. *Nature*, 587(7832):39–40, 2020.

[61] Takanori Nakane et al. Single-particle cryo-EM at atomic resolution. *Nature*, 587(7832):152–156, 2020.

[62] Ka Man Yip et al. Atomic-resolution protein structure determination by cryo-EM. *Nature*, 587(7832):157–161, 2020.

[63] Zonghuan Lu et al. Monolithic microfluidic mixing–spraying devices for time-resolved cryo-electron microscopy. *Journal of Structural Biology*, 168(3):388–395, 2009.

[64] Joachim Frank. Time-resolved cryo-electron microscopy: Recent progress. *Journal of Structural Biology*, 200(3):303–306, 2017.

[65] Heiner Friedrich et al. Imaging of self-assembled structures: Interpretation of TEM and cryo-TEM images. *Angewandte Chemie Intertional Edition*, 49(43):7850–7858, 2010.

[66] Mathew J. Peet, Richard Henderson, and Christopher J. Russo. The energy dependence of contrast and damage in electron cryomicroscopy of biological molecules. *Ultramicroscopy*, 203:125–131, 2019.

[67] Vanessa Cabra and Montserrat Samsó. Do's and don'ts of cryo-electron microscopy: A primer on sample preparation and high quality data collection for macromolecular 3D reconstruction. *Journal of Visualized Experiments*, (95), 2015.

[68] Petr Cizmar and Yuana Yuana. Detection and characterization of extracellular vesicles by transmission and cryo-transmission electron microscopy. In *Methods in Molecular Biology*, pages 221–232. Springer New York, 2017.

[69] Eva Nogales. The development of cryo-EM into a mainstream structural biology technique. *Nature Methods*, 13(1):24–27, 2015.

[70] RF Egerton, P Li, and M Malac. Radiation damage in the TEM and SEM. *Micron*, 35(6):399–409, 2004.

[71] V. E. Cosslett. Radiation damage in the high resolution electron microscopy of biological materials: A review. *Journal of Microscopy*, 113(2):113–129, 1978.

[72] Florian Banhart. Irradiation effects in carbon nanostructures. *Reports on Progress in Physics*, 62(8):1181–1221, 1999.

[73] S. Das et al. Inelastic guiding of electrons in polymer nanocapillaries. *Physical Review A*, 76(4):042716, 2007.

[74] RF Egerton. Control of radiation damage in the TEM. *Ultramicroscopy*, 127:100–108, 2013.

[75] Nan Jiang. Electron beam damage in oxides: a review. *Reports on Progress in Physics*, 79(1):016501, 2015.

[76] RF Egerton. Radiation damage to organic and inorganic specimens in the TEM. *Micron*, 119:72–87, 2019.

[77] T. Lehnert et al. Electron radiation damage mechanisms in 2d MoSe2. *Applied Physics Letters*, 110(3):033106, 2017.

[78] H Seiler. Secondary electron emission in the scanning electron microscope. *Journal of Applied Physics*, 54(11):R1–R18, 1983.

[79] Tanya Gupta et al. Spatially dependent dose rate in liquid cell transmission electron microscopy. *Nanoscale*, 10(16):7702–7710, 2018.

[80] RF Egerton. Mechanisms of radiation damage in beam-sensitive specimens, for TEM accelerating voltages between 10 and 300 kV. *Microscopy research and technique*, 75(11):1550–1556, 2012.

[81] RF Egerton et al. Basic questions related to electron-induced sputtering in the TEM. *Ultramicroscopy*, 110(8):991–997, 2010.

[82] Elisah J. van den Bussche and David J. Flannigan. Reducing radiation damage in soft matter with femtosecond-timed single-electron packets. *Nano Letters*, 19(9):6687–6694, 2019.

[83] Eduardo Ortega et al. High temporal-resolution scanning transmission electron microscopy using sparse-serpentine scan pathways. *Scientific Reports*, 11(1), 2021.

[84] K. S. Novoselov. Electric field effect in atomically thin carbon films. *Science*, 306(5696):666–669, 2004.

[85] Fancheng Meng et al. Graphene-based fibers: A review. *Advanced Materials*, 27(35):5113–5131, 2015.

[86] Radosav S. Pantelic et al. Graphene: Substrate preparation and introduction. *Journal of structural biology*, 174(1):234–238, 2011.

[87] Daniel R Cooper et al. Experimental review of graphene. *International Scholarly Research Notices*, 2012, 2012.

[88] D.S.L. Abergel et al. Properties of graphene: a theoretical perspective. *Advances in Physics*, 59(4):261–482, 2010.

[89] C. N. R. Rao. *Graphene*. Wiley-VCH Verlag GmbH, Weinheim, 2013.

[90] Valeri N. Kotov et al. Electron-electron interactions in graphene: Current status and perspectives. *Reviews of Modern Physics*, 84(3):1067–1125, 2012.

[91] Taisuke Ohta et al. Controlling the electronic structure of bilayer graphene. *Science*, 313(5789):951–954, 2006.

[92] Liangzhu Feng and Zhuang Liu. Graphene in biomedicine: opportunities and challenges. *Nanomedicine*, 6(2):317–324, 2011.

[93] Pooja Rani and V. K. Jindal. Designing band gap of graphene by b and n dopant atoms. *Royal Society of Chemistry Advances*, 3(3):802–812, 2013.

[94] Yuanbo Zhang et al. Direct observation of a widely tunable bandgap in bilayer graphene. *Nature*, 459(7248):820–823, 2009.

[95] F. Chen and N. J. Tao. Electron transport in single molecules: From benzene to graphene. *Accounts of chemical research*, 42(3):429–438, 2009.

[96] Amedea B. Seabra et al. Nanotoxicity of graphene and graphene oxide. *Chemical Research in Toxicology*, 27(2):159–168, 2014.

[97] Sungjin Park et al. Biocompatible, robust free-standing paper composed of a TWEEN/graphene composite. *Advanced Materials*, 22(15):1736–1740, 2010.

[98] Xiaoming Sun et al. Nano-graphene oxide for cellular imaging and drug delivery. *Carbon*, 1(3):203–212, 2008.

[99] R. R. Nair et al. Graphene as a transparent conductive support for studying biological molecules by transmission electron microscopy. *Applied Physics Letters*, 97(15):153102, 2010.

[100] K. S. Novoselov et al. A roadmap for graphene. *Nature*, 490(7419):192–200, 2012.

[101] P. Z. Sun et al. Limits on gas impermeability of graphene. *Nature*, 579(7798):229–232, 2020.

[102] Sumit Goenka, Vinayak Sant, and Shilpa Sant. Graphene-based nanomaterials for drug delivery and tissue engineering. *Journal of Controlled Release*, 173:75–88, 2014.

[103] Zhuang Liu and. PEGylated nanographene oxide for delivery of water-insoluble cancer drugs. *ChemPhysChem*, 130(33):10876–10877, 2008.

[104] Lingyan Feng et al. A graphene functionalized electrochemical aptasensor for selective label-free detection of cancer cells. *Biomaterials*, 32(11):2930–2937, 2011.

[105] Ryan Muszynski, Brian Seger, and Prashant V. Kamat. Decorating graphene sheets with gold nanoparticles. *The Journal of Physical Chemistry C*, 112(14):5263–5266, 2008.

[106] Ming Zhou, Yueming Zhai, and Shaojun Dong. Electrochemical sensing and biosensing platform based on chemically reduced graphene oxide. *Analytical chemistry*, 81(14):5603–5613, 2009.

[107] Su Ryon Shin et al. Graphene-based materials for tissue engineering. *Advanced Drug Delivery Reviews*, 105:255–274, 2016.

[108] Radosav S. Pantelic et al. The application of graphene as a sample support in transmission electron microscopy. *Solid State Communications*, 152(15):1375–1382, 2012.

[109] Jamie H. Warner et al. Examining Co-based nanocrystals on graphene using low-voltage aberration-corrected transmission electron microscopy. *ACS nano*, 4(1):470–476, 2009.

[110] Jannik C. Meyer et al. Imaging and dynamics of light atoms and molecules on graphene. *Nano letters*, 454(7202):319–322, 2008.

[111] Yang Qiu et al. Antioxidant chemistry of graphene-based materials and its role in oxidation protection technology. *Nanoscale*, 6(20):11744–11755, 2014.

[112] Recep Zan et al. Control of radiation damage in MoS2 by graphene encapsulation. *ACS nano*, 7(11):10167–10174, 2013.

[113] Michal Wojcik et al. Graphene-enabled electron microscopy and correlated super-resolution microscopy of wet cells. *Nature Communications*, 6(1), 2015.

[114] Osamu Shimomura, Frank H. Johnson, and Yo Saiga. Extraction, purification and properties of aequorin, a bioluminescent protein from the luminous hydromedusan, *Aequorea*. *Journal of Cellular and Comparative Physiology*, 59(3):223–239, 1962.

[115] James G. Morin and J. W. Hastings. Energy transfer in a bioluminescent system. *Journal of Cellular Physiology*, 77(3):313–318, 1971.

[116] Frank H. Johnson et al. Quantum efficiency of *Cypridina* luminescence, with a note on that of *Aequorea*. *Journal of Cellular and Comparative Physiology*, 60(1):85–103, 1962.

[117] M Chalfie et al. Green fluorescent protein as a marker for gene expression. *Science*, 263(5148):802–805, 1994.

[118] M. Ormö et al. Crystal structure of the aequorea victoria green fluorescent protein. *Science*, 273(5280):1392–1395, 1996.

[119] Fan Yang, Larry G. Moss, and George N. Phillips. The molecular structure of green fluorescent protein. *Nature Biotechnology*, 14(10):1246–1251, 1996.

[120] Chris W. Cody et al. Chemical structure of the hexapeptide chromophore of the aequorea green-fluorescent protein. *Biochemistry*, 32(5):1212–1218, 1993.

[121] Douglas C. Prasher et al. Primary structure of the aequorea victoria green-fluorescent protein. *Gene*, 111(2):229–233, 1992.

[122] Alexey M. Bogdanov et al. Turning on and off photoinduced electron transfer in fluorescent proteins by π-stacking, halide binding, and tyr145 mutations. *Journal of the American Chemical Society*, 138(14):4807–4817, 2016.

[123] Alexander V. Yakhnin et al. Green fluorescent protein purification by organic extraction. *Protein Expression and Purification*, 14(3):382–386, 1998.

[124] Roger Y. Tsien. The Green Fluorescent Protein. *Annual Review of Biochemistry*, 67(1):509–544, 1998.

[125] Andrew B. Cubitt et al. Understanding, improving and using green fluorescent proteins. *Trends in Biochemical Sciences*, 20(11):448–455, 1995.

[126] Hiroshi Morise et al. Intermolecular energy transfer in the bioluminescent system of aequorea. *Biochemistry*, 13(12):2656–2662, 1974.

[127] Martin Chalfie and Steven R Kain. *Green fluorescent protein: properties, applications and protocols*. John Wiley & Sons, 2005.

[128] Marc Zimmer. Green fluorescent protein (GFP): applications, structure, and related photophysical behavior. *Chemical Reviews*, 102(3):759–782, 2002.

[129] Martin Chalfie. Green fluorescent protein. *Photochemistry and Photobiology*, 62(4):651–656, 1995.

[130] David Ehrhardt. GFP technology for live cell imaging. *Current Opinion in Plant Biology*, 6(6):622–628, 2003.

[131] Antsje Nolles et al. Colorful packages: Encapsulation of fluorescent proteins in complex coacervate core micelles. *International Journal of Molecular Sciences*, 18(7):1557, 2017.

[132] George Patterson, Rich N. Day, and David Piston. Fluorescent protein spectra. *Journal of Cell Science*, 114(5):837–838, 2001.

[133] Stephen H. Bokman and William W. Ward. Renaturation of aequorea green-fluorescent protein. *Biochemical and Biophysical Research Communications*, 101(4):1372–1380, 1981.

[134] Brendan P. Cormack, Raphael H. Valdivia, and Stanley Falkow. FACS-optimized mutants of the green fluorescent protein (GFP). *Gene*, 173(1):33–38, 1996.

[135] Tom Misteli and David L. Spector. Applications of the green fluorescent protein in cell biology and biotechnology. *Nature Biotechnology*, 15(10):961–964, 1997.

[136] Alexander S. Mishin et al. The first mutant of the aequorea victoria green fluorescent protein that forms a red chromophore. *Biochemistry*, 47(16):4666–4673, 2008.

[137] J. C. March, G. Rao, and W. E. Bentley. Biotechnological applications of green fluorescent protein. *Applied Microbiology and Biotechnology*, 62(4):303–315, 2003.

[138] Junichi Nakai, Masamichi Ohkura, and Keiji Imoto. A high signal-to-noise Ca^{2+} probe composed of a single green fluorescent protein. *Nature Biotechnology*, 19(2):137–141, 2001.

[139] Hod Dana et al. High-performance calcium sensors for imaging activity in neuronal populations and microcompartments. *Nature Methods*, 16(7):649–657, 2019.

[140] Akira Muto and Koichi Kawakami. Prey capture in zebrafish larvae serves as a model to study cognitive functions. *Frontiers in Neural Circuits*, 7:110, 2013.

[141] J. Akerboom et al. Optimization of a GCaMP calcium indicator for neural activity imaging. *Journal of Neuroscience*, 32(40):13819–13840, 2012.

[142] D. E. Bonder and K. D. McCarthy. Astrocytic Gq-GPCR-linked IP3R-dependent Ca^{2+} signaling does not mediate neurovascular coupling in mouse visual cortex in vivo. *Journal of Neuroscience*, 34(39):13139–13150, 2014.

[143] Christina L. Takanishi et al. GFP-based FRET analysis in live cells. *Brain Research*, 1091(1):132–139, 2006.

[144] R. Heim, D. C. Prasher, and R. Y. Tsien. Wavelength mutations and post-translational autoxidation of green fluorescent protein. *Proceedings of the National Academy of Sciences*, 91(26):12501–12504, 1994.

[145] Roger Heim, Andrew B. Cubitt, and Roger Y. Tsien. Improved green fluorescence. *Nature*, 373(6516):663–664, 1995.

[146] Joanna Krasowska et al. Chromophore of an enhanced green fluorescent protein can play a photoprotective role due to photobleaching. *International Journal of Molecular Sciences*, 22(16):8565, 2021.

[147] Tirthendu Sen et al. Influence of the first chromophore-forming residue on photobleaching and oxidative photoconversion of EGFP and EYFP. *International Journal of Molecular Sciences*, 20(20):5229, 2019.

[148] S James Remington. Fluorescent proteins: maturation, photochemistry and photophysics. *Current Opinion in Structural Biology*, 16(6):714–721, 2006.

[149] Bella L. Grigorenko et al. Modeling of the glycine tripeptide cyclization in the ser65gly/tyr66gly mutant of green fluorescent protein. *Mendeleev Communications*, 29(2):187–189, 2019.

[150] Jason L Fu et al. GFP loss-of-function mutations in arabidopsis thaliana. *G3: Genes, Genomes, Genetics*, 5(9):1849–1855, 2015.

[151] Małgorzata Bartkiewicz et al. Non–fluorescent mutant of green fluorescent protein sheds light on the mechanism of chromophore formation. *FEBS Letters*, 592(9):1516–1523, 2018.

[152] Justus Hermannsdörfer et al. The effect of electron beam irradiation in environmental scanning transmission electron microscopy of whole cells in liquid. *Microscopy and Microanalysis*, 22(3):656–665, 2016.

[153] T. Malis, S. C. Cheng, and R. F. Egerton. EELS log-ratio technique for specimen-thickness measurement in the TEM. *Journal of Electron Microscopy Technique*, 8(2):193–200, 1988.

[154] Patricia Blach, Sercan Keskin, and Niels de Jonge. Graphene enclosure of chemically fixed mammalian cells for liquid-phase electron microscopy. *Journal of Visualized Experiments*, (163), 2020.

[155] Kim L. Kusser and Troy D. Randall. Simultaneous detection of EGFP and cell surface markers by fluorescence microscopy in lymphoid tissues. *Journal of Histochemistry & Cytochemistry*, 51(1):5–14, 2003.

[156] Tessa N Campbell and Francis YM Choy. The effect of pH on green fluorescent protein: a brief review. *Molecular Biology Today*, 2(1):1–4, 2001.

[157] Won-Gyu Choi, Sarah J. Swanson, and Simon Gilroy. High-resolution imaging of Ca^{2+}, redox status, ROS and pH using GFP biosensors. *The Plant Journal*, 70(1):118–128, 2012.

[158] Chong Zhang, Min-Sheng Liu, and Xin-Hui Xing. Temperature influence on fluorescence intensity and enzyme activity of the fusion protein of GFP and hyperthermophilic xylanase. *Applied Microbiology and Biotechnology*, 84(3):511–517, 2009.

[159] William W. Ward et al. Spectral perturbations of the aequorea green-fluorescent protein. *Photochemistry and Photobiology*, 35(6):803–808, 1982.

[160] Hao Chen et al. Effects of pH and ionic strength on sulfamethoxazole and ciprofloxacin transport in saturated porous media. *Journal of Contaminant Hydrology*, 126(1-2):29–36, 2011.

[161] François Courchesne. Electrolyte concentration and composition effects on sulfate sorption by two spodosols. *Soil Science Society of America Journal*, 55(6):1576–1581, 1991.

[162] Ouyang Zhanmu et al. Maintenance of fluorescence during paraffin embedding of fluorescent protein-labeled specimens. *Frontiers in Neuroscience*, 13, 2019.

[163] Willem F. Wolkers, Maria G. van Kilsdonk, and Folkert A. Hoekstra. Dehydration-induced conformational changes of poly-l-lysine as influenced by drying rate and carbohydrates. *Biochimica et Biophysica Acta (BBA) - General Subjects*, 1425(1):127–136, 1998.

[164] J. C. Bischof. Thermal stability of proteins. *Annals of the New York Academy of Sciences*, 1066(1):12–33, 2005.

[165] Sawako Enoki et al. Acid denaturation and refolding of green fluorescent protein†. *Biochemistry*, 43(44):14238–14248, 2004.

[166] William W. Ward and Stephen H. Bokman. Reversible denaturation of aequorea green-fluorescent protein: physical separation and characterization of the renatured protein. *Biochemistry*, 21(19):4535–4540, 1982.

[167] Nicholas M. Schneider et al. Electron–water interactions and implications for liquid cell electron microscopy. *The Journal of Physical Chemistry C*, 118(38):22373–22382, 2014.

[168] Joanna Korpanty, Lucas R. Parent, and Nathan C. Gianneschi. Enhancing and mitigating radiolytic damage to soft matter in aqueous phase liquid-cell transmission electron microscopy in the presence of gold nanoparticle sensitizers or isopropanol scavengers. *Nano Letters*, 21(2):1141–1149, 2021.

[169] Sercan Keskin, Carly Pawell, and Niels de Jonge. Verification of water presence in graphene liquid cells. *Micron*, 149:103109, 2021.

[170] Seyed Mohammadreza Ghodsi et al. In situ study of molecular structure of water and ice entrapped in graphene nanovessels. *ACS Nano*, 13(4):4677–4685, 2019.

[171] Melissa Holstein et al. Strategies for high-concentration drug substance manufacturing to facilitate subcutaneous administration: A review. *Biotechnology and Bioengineering*, 117(11):3591–3606, 2020.

[172] Joseph M. Grogan et al. Bubble and pattern formation in liquid induced by an electron beam. *Nano Letters*, 14(1):359–364, 2013.

[173] Juhan Lee et al. Controlling radiolysis chemistry on the nanoscale in liquid cell scanning transmission electron microscopy. *Physical Chemistry Chemical Physics*, 23(33):17766–17773, 2021.

[174] Shengda Pu, Chen Gong, and Alex W. Robertson. Liquid cell transmission electron microscopy and its applications. *Royal Society Open Science*, 7(1):191204, 2020.

[175] Keiichirou Akiba et al. Cathodoluminescence of green fluorescent protein exhibits the redshifted spectrum and the robustness. *Scientific Reports*, 10(1), 2020.

[176] H. Ikegami, K. Akiba, and H. Minoda. Evaluation of electron radiation damage to green fluorescent protein. *Ultramicroscopy*, 225:113272, 2021.

[177] Johan Hattne et al. Analysis of global and site-specific radiation damage in cryo-EM. *Structure*, 26(5):759–766.e4, 2018.

[178] Trevor H. Moser et al. The role of electron irradiation history in liquid cell transmission electron microscopy. *Science Advances*, 4(4), 2018.

[179] Sarah E. Smith et al. Fluorescence imaging preparation methods for tissue scaffolds implanted into a green fluorescent protein porcine model. *Transgenic Research*, 24(5):911–919, 2015.

[180] Monica Monici. Cell and tissue autofluorescence research and diagnostic applications. In *Biotechnology Annual Review*, pages 227–256. Elsevier, 2005.

[181] Aditi Srinivasa Raja et al. Electron-beam induced luminescence and bleaching in polymer resins and embedded biomaterial. *Macromolecular Bioscience*, 21(11):2100192, 2021.

[182] Georges A. Wagnieres, Willem M. Star, and Brian C. Wilson. In vivo fluorescence spectroscopy and imaging for oncological applications. *Photochemistry and Photobiology*, 68(5):603–632, 1998.

[183] Victoria V. Roshchina. Vital autofluorescence: Application to the study of plant living cells. *International Journal of Spectroscopy*, 2012:1–14, 2012.

[184] T. J. Staughton, C. J. Mcgillicuddy, and P. D. Weinberg. Techniques for reducing the interfering effects of autofluorescence in fluorescence microscopy: improved detection of sulphorhodamine b-labelled albumin in arterial tissue. *Journal of Microscopy*, 201(1):70–76, 2001.

[185] Gregory P. Henderson, Lu Gan, and Grant J. Jensen. 3-D ultrastructure of *O. tauri*: Electron cryotomography of an entire eukaryotic cell. *PLoS ONE*, 2(8):e749, 2007.

[186] Thomas C. Isabell et al. Plasma cleaning and its applications for electron microscopy. *Microscopy and Microanalysis*, 5(2):126–135, 1999.

[187] Daniel J. Preston et al. Effect of hydrocarbon adsorption on the wettability of rare earth oxide ceramics. *Applied Physics Letters*, 105(1):011601, 2014.

[188] P.M Ajayan and Sumio Iijima. Wetting and de-wetting transitions of small metal particles on substrates under electron irradiation. *Journal of Colloid and Interface Science*, 147(1):281–285, 1991.

[189] Pritam Das, N. Usha Kiran, and Shyamal Chatterjee. Electron beam modulated wettability and electrical conductivity of hydrogen titanate nanowires. *The Journal of Physical Chemistry C*, 125(29):16191–16199, 2021.

[190] I. Torchinsky and G. Rosenman. Wettability modification of nanomaterials by low-energy electron flux. *Nanoscale Research Letters*, 4(10), 2009.

[191] M.Gregor et al. Hydrophobicity of electron beam modified surface of hydroxyapatite films. *Applied Surface Science*, 337:249–253, 2015.

[192] Taylor J. Woehl et al. Correlative electron and fluorescence microscopy of magnetotactic bacteria in liquid: Toward in vivo imaging. *Scientific Reports*, 4(1), 2014.

[193] M Hahn, J Seredynski, and W Baumeister. Inactivation of catalase monolayers by irradiation with 100 keV electrons. *Proceedings of the National Academy of Sciences*, 73(3):823–827, 1976.

[194] Joseph A. Sebastian et al. An image-based flow cytometric approach to the assessment of the nucleus-to-cytoplasm ratio. *PLOS ONE*, 16(6):e0253439, 2021.

[195] S. W. Hell. Far-field optical nanoscopy. *Science*, 316(5828):1153–1158, 2007.

[196] Yaron M. Sigal, Ruobo Zhou, and Xiaowei Zhuang. Visualizing and discovering cellular structures with super-resolution microscopy. *Science*, 361(6405):880–887, 2018.

[197] Rebecca F. Thompson et al. An introduction to sample preparation and imaging by cryo-electron microscopy for structural biology. *Methods*, 100:3–15, 2016.

[198] Vladan Lučić, Andrew Leis, and Wolfgang Baumeister. Cryo-electron tomography of cells: connecting structure and function. *Histochemistry and Cell Biology*, 130(2):185–196, 2008.

[199] Johnny L. Carson. Fundamental technical elements of freeze-fracture/freeze-etch in biological electron microscopy. *Journal of Visualized Experiments*, (91), 2014.

[200] Hidetoshi Nishiyama et al. Reprint of: Atmospheric scanning electron microscope observes cells and tissues in open medium through silicon nitride film. *Journal of Structural Biology*, 172(2):191–202, 2010.

[201] Indra N. Dahmke et al. Graphene liquid enclosure for single-molecule analysis of membrane proteins in whole cells using electron microscopy. *ACS Nano*, 11(11):11108–11117, 2017.

[202] Yuusuke Maruyama et al. Immuno EM–OM correlative microscopy in solution by atmospheric scanning electron microscopy (ASEM). *Journal of Structural Biology*, 180(2):259–270, 2012.

[203] Takaaki Kinoshita et al. Immuno-electron microscopy of primary cell cultures from genetically modified animals in liquid by atmospheric scanning electron microscopy. *Microscopy and Microanalysis*, 20(2):469–483, 2014.

[204] Ryuichi Kato et al. High-precision thickness control of ice layer on CVD grown bilayer graphene for cryo-TEM. *Carbon*, 160:107–112, 2020.

[205] Ben N G Giepmans et al. Correlated light and electron microscopic imaging of multiple endogenous proteins using quantum dots. *Nature Methods*, 2(10):743–749, 2005.

[206] Diana B Peckys, Ulrike Korf, and Niels de Jonge. Local variations of HER2 dimerization in breast cancer cells discovered by correlative fluorescence and liquid electron microscopy. *Science advances*, 1(6):e1500165, 2015.

[207] Charles Eigenbrot et al. Structural basis for high-affinity HER2 receptor binding by an engineered protein. *Proceedings of the National Academy of Sciences*, 107(34):15039–15044, 2010.

[208] Martin Textor and Niels de Jonge. Strategies for preparing graphene liquid cells for transmission electron microscopy. *Nano Letters*, 18(6):3313–3321, 2018.

[209] Hong Yi et al. Native immunogold labeling of cell surface proteins and viral glycoproteins for cryo-electron microscopy and cryo-electron tomography applications. *Journal of Histochemistry and Cytochemistry*, 63(10):780–792, 2015.

[210] Sharon Grayer Wolf, Lothar Houben, and Michael Elbaum. Cryo-scanning transmission electron tomography of vitrified cells. *Nature Methods*, 11(4):423–428, 2014.

[211] Madeline J. Dukes et al. Three-dimensional locations of gold-labeled proteins in a whole mount eukaryotic cell obtained with 3nm precision using aberration-corrected scanning transmission electron microscopy. *Journal of Structural Biology*, 174(3):552–562, 2011.

[212] Carola Meier and Anja Beckmann. Freeze fracture: new avenues for the ultrastructural analysis of cells in vitro. *Histochemistry and Cell Biology*, 149(1):3–13, 2017.

[213] Diana B. Peckys and Niels de Jonge. Liquid scanning transmission electron microscopy: Imaging protein complexes in their native environment in whole eukaryotic cells. *Microscopy and Microanalysis*, 20(2):346–365, 2014.

[214] Kunmo Koo et al. Live cell electron microscopy using graphene veils. *Nano Letters*, 20(6):4708–4713, 2020.

[215] James B. Pawley, editor. *Handbook Of Biological Confocal Microscopy*. Springer US, 2006.

[216] Inhee Chung et al. Spatial control of EGF receptor activation by reversible dimerization on living cells. *Nature*, 464(7289):783–787, 2010.

[217] Dmitry A. Gorbachev et al. A general mechanism of green-to-red photoconversions of GFP. *Frontiers in Molecular Biosciences*, 7, 2020.

[218] Andrew T Ulijasz and Richard D Vierstra. Phytochrome structure and photochemistry: recent advances toward a complete molecular picture. *Current Opinion in Plant Biology*, 14(5):498–506, 2011.

[219] Jannik C. Meyer et al. Accurate measurement of electron beam induced displacement cross sections for single-layer graphene. *Physical Review Letters*, 108(19), 2012.

A Appendices

A.1 List of Figures

1.1 Electron microscopic images of biological specimens. 1
2.1 Schematic setup of electron microscopes. 6
2.2 Dependence of the interaction volume in SEM in bulk specimens. . 8
2.3 SiN liquid Cell in TEM. 9
2.4 Preparation methods for GLCs. 10
2.5 Signal generation in ESEM. 11
2.6 Scattering of incident beam electrons in an atom of a specimen. . . 14
2.7 Ratio for inelastic and elastic scattering cross section. 18
2.8 Molecular structure, excitation and emission spectra of GFP. 23
2.9 Chromophores and emission wavelengths of various fluorescent proteins. 25
3.1 Schematics of GFP binding methods. 34
3.2 Assembly of a SiN liquid cell 36
3.3 Assembly of a graphene liquid cell 37
3.4 EELS of GLCs with PBS in STEM. 40
3.5 Analysis of the area of SKBR3 cells. 42
3.6 Cell seeding on a SiN window of a silicon microchip and HER2 labeled. 44
3.7 Graphene coating of cells seeded on a Si microchip. 46
4.1 Photobleaching of GFP on SiN during fluorescence microscopy. . . . 50
4.2 Photobleaching of GFP in GLCs. 51
4.3 RFI of dry GFP. 52
4.4 RFI of GFP in EM conditions over time. 53
4.5 Fluorescence images of GFP in SiN liquid cells after each electron beam exposure in liquid-phase TEM at 200 kV. 54
4.6 RFI of GFP in liquid-phase TEM at 200 kV. 56
4.7 Liquid thickness of different regions in GLCs with PBS, GFP and H_2O. 57

4.8 Overview of a graphene liquid cell (GLC) with encapsulated green fluorescent protein (GFP) under fluorescence microscopy. 58
4.9 Fluorescence images of GFP encapsulated in a GLC after each electron beam exposure in liquid-phase TEM at 200 kV. 58
4.10 RFI of GFP in GLCs exposed in liquid-phase TEM at 200 kV. . . . 59
4.11 RFI of GFP in GLCs exposed in liquid-phase TEM at 30 kV. 61
4.12 RFI of GFP in GLCs exposed in liquid-phase TEM at 30 kV and 200 kV. 61
4.13 Comparison of RFI of GFP in GLCs and SiN liquid cells exposed in liquid-phase TEM at 200 kV. 62
4.14 Fluorescence images of GFP after each electron beam exposure in ESEM at 30 kV. 64
4.15 RFI of GFP during electron beam exposure in ESEM at 30 kV. . . 65
4.16 Comparison of electron beam exposure with a defocused and a focused electron beam in ESEM at 30 kV. 65
5.1 Overview of fixed SKBR3 cells labeled with GFP in a SiN liquid cell. 77
5.2 Photobleaching and autofluorescence of GFP expressing and unlabeled SKBR3 cells. 78
5.3 Drying of GFP expressing and unlabeled SKBR3 cells. 79
5.4 Exposure of GFP expressing SKBR3 cells to electron microscopy conditions. 80
5.5 Unlabeled SKBR3 cells exposed in TEM at 200 kV and ESEM at 30 kV. 81
5.6 Fluorescence images of SKBR3 cells labeled with GFP in TEM at 200 kV. 83
5.7 GFP expressing SKBR3 cells exposed in TEM at 200 kV. 84
5.8 Non-expressing SKBR3 cells exposed in TEM at 200 kV. 84
5.9 GFP expressing and unexposed SKBR3 cells in TEM. 85
5.10 Non-expressing and unexposed SKBR3 cells in TEM. 86
5.11 Fluorescence images of GFP labeled SKBR3 cells in ESEM at 30 kV. 87
5.12 GFP expressing SKBR3 cells exposed in ESEM at 30 kV. 88
5.13 GFP expressing and unexposed SKBR3 cells in ESEM. 89
6.1 STEM of graphene coated and non-coated SKBR3 cells on SiN window. 99

6.2 Artifacts arising on samples without graphene coating. 100
A.1 pH measurements for PBS and HPLC-grade H_2O 132
A.2 Stage shift after multiple removals of the sample holder. 133

A.2 List of Tables

1 Table of Chemicals 27
2 Table of Expendable Materials 29
3 Table of Hardware 30
4 Preparation of Working Solutions 31
5 Critical electron doses of green fluorescent protein in silicon nitrite liquid cells in liquid-phase transmission electron microscopy. 55
6 Critical electron doses of green fluorescent protein in graphene liquid cells in liquid-phase transmission electron microscopy. 59
7 Critical electron doses of green fluorescent protein in silicon nitrite and graphene liquid cells in liquid-phase transmission electron microscopy. 62
8 Critical electron doses of green fluorescent protein on silicon nitrite in environmental scanning electron microscopy. 66
9 Results for the dose tolerance in liquid-phase electron microscopy. . 66

A.3 pH Measurements for PBS and HPLC-grade H_2O

The pH of PBS and HPLC-grade H_2O was measued. **Figure A.1** shows pH measurements using pH test stripes. Both, PBS (**a**) and HPLC-grade H_2O (**b**) show a pH around 7.5.

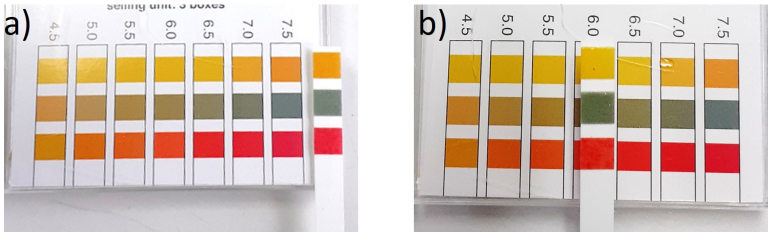

Figure A.1: PH measurements for PBS and HPLC-grade H_2O a) PBS b) HPLC-grade H_2O. Both solutions show a pH around 7.5.

A.4 Calculation of the Ionic Strength

The ionic strength is calculated by

$$\text{ionic strength} = \frac{1}{2}\sum_{i=1}^{n} c_i z_i^2 \tag{19}$$

PBS used in this work contains the following components:

- 154 mM $NaCl \longrightarrow Na^+ + Cl^-$
- 5.6 mM $Na_2HPO_4 \longrightarrow 2Na^+ + HPO_4^{2-}$
- 1 mM $KH_2PO_4 \longrightarrow K^+ + H_2PO_4^-$

with these components, the calculated ionic strength is 169 mol/L.

A.5 Stage Shift

The position of the stage was marked in the TEM center software to be able to expose the same region for all exposures. However, the stage can shift between multiple removals of the holder. This shift was evaluated as shown in **Figure A.2**. The shift was found around 3 µm after 5 removals of the holder and 3.5 µm after 10 removals.

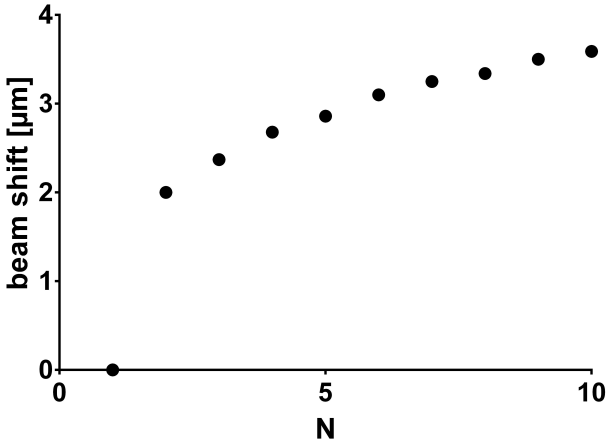

Figure A.2: Stage shift after multiple removals of the sample holder.

A.6 Publications

Peer-Reviewed Publications

- Blach, P., Keskin, S., de Jonge, N. Graphene Enclosure of Chemically Fixed Mammalian Cells for Liquid-Phase Electron Microscopy. Journal of Visualized Experiments, 2020, doi:10.3791/61458.

- Klarner, M.; Blach, P.; Wittkämper, H.; Jonge, N.; Papp, C. & Kempe, R. Key Parameters for the Synthesis of Active and Selective Nanostructured 3d Metal Catalysts Starting from Coordination Compounds – Case Study: Nickel Mediated Reductive Amination. ChemCatChem, Wiley, 2021, doi: 10.1002/cctc.202100562.

- Klausfelder, B.; Blach, P.; Jonge, N. & Kempe, R. Synthesis of 3,4-Dihydro-2H-pyrroles from Ketones, Aldehydes, and Nitro Alkanes via Hydrogenative Cyclization. Chemistry - A European Journal, Wiley, 2022, doi: 10.1002/chem.202201307.

Conferences Contributions

- Blach, Patricia, de Jonge, Niels. Investigation of the Electron Beam Dose Tolerance of GFP in Liquid. Cell Physics, Saarland University, 2021.

- Blach, Patricia, de Jonge, Niels. Studying Electron Beam Induced Radiation Damage on Graphene Coated SKBR3 Cells. Gordon Research Conference on Liquid Phase Electron Microscopy, Tuscany, 2020.

- Blach, Patricia, de Jonge, Niels. Reducing electron beam induced radiation damage on SKBR3 cells by graphene coating. In: Cell Physics 2019, October 9-11, 2019, Saarland University . Saarland University ; 2019: 113 P.7.

- Blach, Patricia, Weinberg, Florian, Peckys, Diana, Dahmke, Indra N., de Jonge, Niels. Analysis of breast cancer cell subpopulations for the expression and distribution of HER2 and their response to anti-cancer drugs using electron microscopy. Microscopy and Microanalysis 2019, 25 (1S), 51-52.

- Blach, Patricia, Weinberg, Florian, Dahmke, Indra N., Peckys, Diana, de Jonge, Niels. Single cell analysis of HER2 receptors with nanometer resolution of breast cancer cells by electron microscopy. AEK: 20th International AEK Cancer Congress, European Molecular Biology Laboratory EMBL, Heidelberg, 2019.

- Blach, Patricia, Weinberg, Florian, Peckys, Diana, Dahmke, Indra N., de Jonge, Niels. Analysis of breast cancer cell subpopulations for the expression and distribution of HER2 and their response to anti-cancer drugs using electron microscopy. CISCEM 2018 - 4th International Conference on In Situ and Correlative Electron Microscopy, Saarland University, 2018.